Title

Development of a Hessian-Free Algorithm for Transition State Searches, Application to Reactions of Light Alkanes in Zeolite Catalysts, and Extension to Wavefunction Stability Analysis in the Absence of Analytical Hessians

Author

Mallikarjun Sharada, Shaama M

Publication Date

2015

Peer reviewed|Thesis/dissertation

Development of a Hessian-Free Algorithm for Transition State Searches, Application to Reactions of Light Alkanes in Zeolite Catalysts, and Extension to Wavefunction Stability Analysis in the Absence of Analytical Hessians

by

Shaama Mallikarjun Sharada

A dissertation submitted in partial satisfaction of the
requirements for the degree of
Doctor of Philosophy

in

Chemical Engineering

in the

Graduate Division

of the

University of California, Berkeley

Committee in charge:

Professor Alexis T. Bell, Co-chair
Professor Martin Head-Gordon, Co-chair
Professor David B. Graves
Professor William H. Miller

Summer 2015

Development of a Hessian-Free Algorithm for Transition State Searches, Application to Reactions of Light Alkanes in Zeolite Catalysts, and Extension to Wavefunction Stability Analysis in the Absence of Analytical Hessians

Abstract

Development of a Hessian-Free Algorithm for Transition State Searches, Application to Reactions of Light Alkanes in Zeolite Catalysts, and Extension to Wavefunction Stability Analysis in the Absence of Analytical Hessians

by

Shaama Mallikarjun Sharada

Doctor of Philosophy in Chemical Engineering

University of California, Berkeley

Professor Alexis T. Bell, Co-chair

Professor Martin Head-Gordon, Co-chair

The cost of calculating second derivatives of the energy, or nuclear hessians, in the course of quantum chemical analyses can be prohibitive for systems containing hundreds of atoms. In particular, when searching for reaction transition states (TSs), only a few eigenvalues and eigenvectors, and not the full hessian, are required. Here, a method is described that can eliminate the need for hessian calculations for both TS searches as well as characterization of stationary points. A finite differences implementation of the Davidson method that uses only first derivatives of the energy to calculate the lowest eigenvalues and eigenvectors of the hessian is discussed. When implemented in conjunction with a double-ended interpolation method for generating TS guesses, such as the freezing string method (FSM), an approximate hessian can be constructed in lieu of the full hessian as input to any quasi-Newton TS optimization routine. With equal ease, the finite differences Davidson approach can be implemented at the end of geometry optimization for verifying stationary points on a potential energy surface. The approach scales one power of system size lower than exact hessian calculation since the rate of convergence is approximately independent of the size of the system. Therefore, it achieves significant cost savings relative to exact hessian calculation when applied to both stationary point characterization as well as TS search, particularly when analytical hessians are not available or require substantial computational effort.

The TS search approach is a useful tool for reaction kinetics and catalysis studies. Zeolite catalysts are employed extensively in industry owing to their high Brønsted acidity and shape selective properties, which are probed typically using monomolecular cracking and dehydrogenation reactions of alkanes. The TS search method is combined with hybrid quantum mechanics/molecular mechanics (QM/MM), and a modified harmonic oscillator approximation in order to calculate intrinsic activation parameters for monomolecular reactions of n-butane. The first study calculates TSs for all cracking and dehydrogenation

pathways in MFI. Based on an examination of adsorption enthalpies and intrinsic activation energies for these reactions at active sites located at the channel intersection as well as the sinusoidal channel in MFI, the analysis concludes that reaction energetics are highly sensitive to the active site location due to varying acidities and non-bonding framework-substrate interactions.

The second investigation extends the QM/MM approach to examine the sensitivity of intrinsic reaction kinetics to zeolite pore topology. Monomolecular cracking and dehydrogenation reactions of n-butane are examined in six zeolite frameworks - TON, SVR, MFI, MEL, STF and MWW, with active sites located within channels, channel intersections and cage geometries. By analyzing calculated intrinsic enthalpies and entropies of activation together with experimental values, the sensitivity of cracking and dehydrogenation pathways to active site location is examined for all site types. Dehydrogenation exhibits a surprising preference for the methyl pathway in cages in spite of the higher barrier relative to methylene, which points towards significant entropy compensation occurring at these active sites. However, although computed enthalpies of activation are in good agreement with experiment, thermochemical approximations that better account for anharmonic contributions are required to accurately determine entropy differences between these pathways.

The hessian-free finite differences Davidson approach can also be extended to the space of molecular orbital coefficients. Wavefunction stability analysis is commonly applied to converged self-consistent field (SCF) solutions to verify whether the electronic energy is a local minimum with respect to second-order variation in the orbitals, by calculating the lowest eigenvalue of the electronic hessian. Analytical expressions for the electronic hessian are unavailable for some advanced post-Hartree–Fock (HF) wave function methods and even certain Kohn–Sham (KS) density functionals. Calculating full finite difference hessians for even small molecules can prove intractable in such cases. To address this issue, the hessian-vector product within the Davidson scheme is formulated as a finite difference of the electronic gradient with respect to orbital perturbations. As a model application, following the lowest eigenvalue of the orbital-optimized second-order Møller–Plesset perturbation theory (OOMP2) hessian during H_2 dissociation reveals the surprising stability of the spin-restricted solution at all separations, with a second independent unrestricted solution. A single stable solution can be recovered by using the regularized OOMP2 method (δ-OOMP2), which contains a level shift. Internal and external stability analyses are also performed for SCF solutions of a recently developed range-separated hybrid density functional, ωB97X-V, for which the analytical hessian is not yet available due to the complexity of its long-range non-local VV10 correlation functional.

To Prashant Pawan Pisipati
...who beat all odds and moved halfway across the globe to be by my side.

Contents

List of Figures

List of Tables

Acknowledgments

Unlike what popular culture would have us believe, scientific research is not a single player sport. This thesis is the result of the combined effort of many dedicated scientists, and I am deeply indebted to all of them. First and foremost, I wish to thank both my advisors, Prof. Alexis T Bell and Prof. Martin Head-Gordon, for their invaluable guidance and support these past five years. Both of them are extremely humble, care deeply about their students, and make time every week for meetings in spite of their busy schedules and large groups. There is a lot to learn from Alex and Martin, and not just on the science side of things. They taught me to ask the right questions, to think critically, and to persevere. They are the most amazing advising team anyone can ask for, and I will dearly miss working with them.

I also want to thank both the Bell Choir and the Head-Gordon group for all the support and collaborations over the years. I am very grateful to Joseph Gomes, who showed me the ropes of computational research when I started out in the lab, and also engaged in several enriching discussions. I also want to thank Dr. Paul Zimmerman, who spent a lot of time during his postdoctoral stint at Berkeley guiding me through the early days of my project. Amber Janda, my brilliant experimental collaborator, taught me nearly everything I know about zeolite chemistry. I am grateful to David Stück, an enthusiastic collaborator in developing methods to aid electronic structure calculations. I also want to thank other collaborators – Yi-Pei Li, Jason Wu, Dr. Andreas Hauser, Karthish Manthiram, and Dr. Eric Sundstrom. A special thank you to Dr. Shannon Klaus for spreading cheer and breaking the monotony of computing life, and Rachel Licht for single-handedly organizing all social events and keeping the Bell group alive!

Life in Berkeley would have been incomplete without the friendships forged here. Sarika Goel and I went from strangers to roommates to fast friends in no time. I was very fortunate to find someone as sweet and caring as Sarika to share graduate life with. I am also grateful to the wonderful group of friends I have – the entire ChemE batch of 2010, Sudeep Kamath, Kaushik Jayaram, Onkar Dalal, Rutooj Deshpande, Mangesh Bangar, Kartik Ganapati, Pavan Hosur, Gireeja Ranade, Shraddha Vacchani, Siddhartha Pathak, and many more. Together, we have traveled, hiked, played tennis, watched (and made!) movies, and celebrated festivals, adding fun and color to an otherwise difficult and tedious journey.

The decision to move to a different continent for graduate studies was not an easy one, but I was backed by a completely supportive and loving family. My father very nearly built a library at home to encourage me to read widely. If not for him, I probably would have struggled to communicate in English to this day. My mother is my goddess and my pillar of strength through thick and thin. She has always, always been there for me. I am very lucky to have a little sister and role model like Appu, who is not only my best friend but also the kindest and most selfless person on earth. Leaving Pawan behind to move here was a very

tough decision, but he supported me nevertheless, and strove hard to move here too so we could begin a life together. I am thankful for the love and support of all these people, and for the vibrant atmosphere at UC Berkeley that promotes collaboration and camaraderie over everything else.

Chapter 1

Introduction

1.1 Computational tools for catalysis and quantum chemistry

One of the key components of computational reaction kinetics studies is the calculation of transition states (TSs). A TS is a first order saddle point, and a maximum along the minimum energy path connecting a reactant and a product on a potential energy surface. These characteristic points on the potential surface not only shed light on reaction mechanisms but also provide a quantitative estimate of the barriers to chemical reactions and the impact of catalysts on reaction rates. However, the calculation of TSs, particularly in the course of quantum chemical analyses, can be tedious owing to the high dimensionality of most potential energy surfaces and associated computational costs.

Early efforts to develop TS search algorithms were based purely on gradient minimization[1]. On a complex potential energy surface, though, one runs the risk of converging to a stationary point that is not a TS since gradients at all stationary points are identically zero. However, the eigenvalue spectrum of the matrix of second derivatives of the energy (hessian) can be employed to distinguish between various stationary points. An important milestone in the development of TS search methods was the first hessian-based algorithm proposed by Cerjan and Miller[2], in which the search follows the reaction coordinate uphill from the minimum to the TS.

These early developments, along with enhanced computing speeds, spurred progress in the field of TS search algorithms that aimed at reducing guesswork and computational effort[3]. TS search was recognized as a two-step problem: first involved the generation of a reliable guess structure, and the second step was to optimize or refine this guess. Guesses can be generated by hand, or by employing a scheme that interpolates between reactant and product to generate an approximate reaction path. One of the first, and probably most widely used double-ended interpolation techniques is the nudged elastic band (NEB)[4] method. TS

refinement methods include gradient-based methods that calculate the lowest eigenmode on the fly[5], as well as eigenvector-following methods that require explicit calculation of the hessian matrix as input[6, 7]. Although hessian-based methods are robust, they scale poorly with size owing to approximately cubic scaling of hessian calculation and storage costs. Since this poses a severe bottleneck to kinetics studies on large, complex catalytic systems, there is a need for TS search methods that are not only efficient but also avoid full hessian calculations, and can therefore be applied to larger systems at reasonable computational cost.

A crystalline zeolite framework consisting of Brønsted acid sites is a classic example of a large, complex catalytic system. Zeolites are important cracking catalysts in the petrochemical industry due to their high acidity, shape-selective behavior and thermal stability[8, 9]. Since zeolite pores are typically of molecular dimensions, the extended framework surrounding active sites also has an important role to play in reaction kinetics. The framework can not only stabilize adsorbates and reaction intermediates via non-bonding dispersion and electrostatic interactions, but can also restrict the mobility of the adsorbate depending on both pore size and shape, and substrate geometry. As a result, the pre-exponential factor comprising the entropy of activation cannot be neglected for reactions occurring at high temperatures within these zeolites. The design and selection of zeolite catalysts for specific reactions, therefore, requires knowledge of the distribution and strength of active sites, as well as confinement effects induced by the zeolite pore topology. The exact locations of active sites in most zeolites cannot be directly determined, although it has been demonstrated that the distribution of active sites is non-random and strongly dependent on conditions of synthesis[10]. In addition, the results of examining probe reactions such as monomolecular alkane cracking in various zeolite frameworks has led to conflicting conclusions about the role of the extended framework. While some studies conclude that confinement effects affect only adsorption enthalpies and entropies[11], others claim that the framework can also influence intrinsic rates[12].

Quantum chemistry plays a significant role in developing a better understanding of these structure-function relationships since it allows the study of reaction kinetics at specific active sites. By combining density functionals that can accurately estimate non-bonding interactions such as dispersion[13], and sufficiently large representations of the catalyst via periodic[14] or hybrid quantum mechanics/molecular mechanics (QM/MM) approaches[15], it is now possible for theoretical models to achieve the accuracy of experimentally determined energy changes. However, quantum chemical approaches generally fail to accurately calculate entropies of adsorption and activation since the standard rigid rotor/harmonic oscillator (RRHO) approximation for thermodynamic quantities cannot capture restricted translational and rotational degrees of freedom of an adsorbed molecule within the pores[16]. More recently, both static[17, 18] and more expensive dynamic approaches[19, 20] have been developed in order to better understand entropy, and consequently free energy effects in zeolite catalysts.

The computational bottleneck posed by hessian calculations is not limited to stationary points on potential energy surfaces. While the nuclear hessian can be expensive, the dimensionality of the hessian is still small enough for calculation and storage to be feasible. On the other hand, the space of molecular orbital coefficients is significantly higher-dimensional. Wavefunction stability analysis involves the calculation of the lowest eigenvalue of the hessian with respect to orbital rotations in order to verify whether the variationally determined electronic energy corresponds to a local minimum. In traditional Hartree-Fock (HF) theory and density functional theory (DFT) where analytical second derivatives of the exchange-correlation function are available, the analysis of wavefunction stability is inexpensive[21]. However, suitable hessian-free approaches are required for examining the stability of post-HF methods or DFT when analytical hessians are not readily available.

1.2 Outline

The goal of this project is to develop a hessian-free strategy that renders TS search viable for large systems. Eliminating the need for full hessian calculations, which scale approximately cubically with system size, is an essential component of this strategy. Chapter 2 describes one such procedure for TS search. The first step involves calculation of a reliable guess to the TS using a modified implementation of the double-ended Freezing String Method (FSM). The existing conjugate gradient optimization step in FSM is replaced with quasi-Newton line search, which reduces the computational effort of finding the TS guess by about half. FSM not only generates a TS guess starting from reactant and product geometries, but also provides a guess for the reaction coordinate at the TS guess. The coordinate is employed, along with a single-step estimate of the curvature at the TS guess, to construct an approximate hessian matrix input to a quasi-Newton-based TS optimization method in lieu of the exact hessian. In most cases, the optimizer with this approximate hessian input performs at least as well as with an exact hessian input, thereby demonstrating that FSM with approximate hessian-based TS search is a viable TS search procedure for large systems where exact hessians are expensive to compute.

Chapter 3 describes a more reliable eigenvalue finding technique to replace the one-step interpolated curvature estimate described in chapter 2. Implementation of a finite differences Davidson method for calculating the lowest eigenvalue(s) and eigenvector(s) of a hessian matrix without actually computing the hessian is discussed. By replacing the hessian-vector product in the standard Davidson procedure for iterative matrix diagonalization with finite differences of perturbed gradients, the exact eigenvalue and eigenvector corresponding to the reaction coordinate can be calculated. Therefore, compared to the interpolation in Chapter 2, this technique generates a more reliable approximation to the hessian as input to TS optimization. In addition, it also serves as a post-optimization characterization method for minima and TSs, thereby avoiding full hessian calculations that are usually required to verify the nature of stationary points. By using the lowest eigenvectors of the quasi-Newton

updated hessian matrix from the optimizer as guess vectors to the Davidson method, significant cost savings can be achieved relative to full hessian calculations for both large systems as well as in cases where analytical hessians are unavailable. In addition, the end-to-end process of locating and characterizing TSs beginning from reactants and products becomes automated with this approach with minimal user intervention.

A key application of the TS search approach is the examination of complex catalytic systems such as zeolites. Chapter 4 discusses the application of FSM, in conjunction with hybrid quantum mechanics/molecular mechanics (QM/MM) and dispersion-corrected DFT to examine the mechanisms and calculate activation energies for monomolecular cracking and dehydrogenation of n-butane at Brønsted acid sites in the MFI framework. The computational approach is significantly more accurate in estimating activation energies relative to earlier methods proposed in the literature. In addition, it is demonstrated that different active sites within the same framework are not kinetically equivalent. Adsorption enthalpies and intrinsic activation energies for cracking and dehydrogenation vary markedly with active site location, due to differences in acidity of the proton as well as non-bonding interactions between the extended framework and the substrate.

Chapter 5 extends the approach described in Chapter 4, along with an improved thermochemical approximation, to examine trends in both intrinsic activation enthalpies as well as entropies for active sites situated in various pore geometries ranging from narrow one-dimensional channels to large supercages. In general, enthalpies can be calculated within experimental accuracy. Unfortunately, the thermochemical approximation can only capture entropies correctly only when deviations from harmonic behavior are small. Enthalpies of activation for both central and terminal cracking are relatively insensitive to the location of the active site. On the other hand, comparison between experiments and computations reveals a distinct pathway preference for dehydrogenation. The methylene pathway is preferred for active sites in both channels as well as channel intersections owing to lower enthalpic barrier compared to the methyl pathway. Within active sites in cages, however, methyl dehydrogenation seems to occur almost exclusively, which can be attributed to entropy compensation occurring in larger, less confined pore geometries.

The hessian-free finite difference Davidson method described in Chapter 3 can be also be applied to the space of molecular orbital rotations. Chapter 6 outlines the extension of this approach to wavefunction stability analysis, a procedure that verifies whether variationally determined electronic energy is a local minimum with respect to second order variation of molecular orbitals. The finite difference Davidson method is implemented for post-Hartree Fock methods and density functionals that lack analytical expressions for the electronic hessian. This novel approach to stability analysis is a useful diagnostic tool to examine stability and dissociation behavior of spin-restricted and unrestricted solutions for post-Hartree Fock methods such as orbital-optimized Møller–Plesset perturbation theory (OOMP2). It is also demonstrated to be a low-cost, practical means of examining the stability of metal-containing

systems such as organometallics using DFT, where multiple spin states of varying energies are likely to emerge from electronic energy calculations.

Chapter 2

Automated Transition State Searches without Evaluating the Hessian

2.1 Abstract

Accurate and speedy determination of transition structures (TSs) is essential for computational studies on reaction pathways, particularly when the process involves expensive electronic structure calculations. Many search algorithms require a good initial guess of the TS geometry, as well as a Hessian input that possesses a structure consistent with the desired saddle point. Among the double-ended interpolation methods for generation of the guess for the TS, the freezing string method (FSM) is proven to be far less expensive compared to its predecessor, the growing string method (GSM). In this chapter, it is demonstrated that the efficiency of this technique can be improved further by replacing the conjugate gradient optimization step (FSM-CG) with a quasi-Newton line search coupled with a BFGS Hessian update (FSM-BFGS). A second crucial factor that affects the speed with which convergence to the TS is achieved is the quality and cost of the Hessian of the energy for the guessed TS. For electronic structure calculations, the cost of calculating an exact Hessian increases more rapidly with system size than the energy and gradient. Therefore, to sidestep calculation of the exact Hessian, an approximate Hessian is constructed, using the tangent direction and local curvature at the TS guess. It is demonstrated that the partitioned-rational function optimization algorithm for locating TSs with this approximate Hessian input performs at least as well as with an exact Hessian input in most test cases. The two techniques, FSM and approximate Hessian construction, therefore can significantly reduce costs associated with finding TSs.

2.2 Introduction

The determination of transition structures (TSs), which are first order saddle points between reactants and products on potential energy surfaces, is a critical step in the analysis

of reaction pathways and rates. TS searches typically involve two steps. The first step is determination of a guess for the TS based on the reactant and product configurations, while the second step is the refinement of the guess to precisely locate the saddle point. Owing to substantial computational costs associated with electronic structure calculations, traditionally, the TS guess is determined by hand.[3, 22, 23] The process involves using chemical intuition such as knowledge of the form of the TS in a system related to the one under study. If the guess is sufficiently good that it lies in the quadratic basin of the TS, or in other words has one negative hessian eigenvalue, then it is likely that the TS can be successfully located. The principal advantage of this homolog-based approach is that it is computationally free and can be successful in systems that are either simple or very closely related to ones with known TSs. The disadvantage is that a rather large amount of human trial and error is required in many applications, particularly those where intuition fails and homology is not available. Unfortunately this encompasses many complex systems, particularly those involved in catalytic processes, where multiple TSs, as well as intermediates that may not be observed, exist on intricate pathways between reactants and products[24, 25].

To overcome the limitations of either human or machine-based guessing, there has accordingly been growing effort to automatically identify a high-quality trial structure for the TS by characterizing the path(s) connecting a pair of known local minima, typically reactant and product structures. The result is a discretized path, which may approximate the intrinsic reaction coordinate (IRC) corresponding to the zero velocity trajectory linking the TS to reactants and products. There are a great variety of path searching methods in common use, most of which employ double-ended techniques such as the nudged elastic band (NEB)[4, 26–29], the string method (SM)[30–34] the searching string method[35], spline methods[36], the growing string method (GSM)[37–41] or the freezing string method (FSM)[42]. Given the discretized path, the geometry corresponding to the highest energy intermediate can be harvested as a high-quality TS guess. The second step involves refining the TS guess using algorithms such as the Berny optimization algorithm[7], the dimer method[5, 43], partitioned-rational function optimization (P-RFO)[2, 6, 44] eigenvector following methods[2, 44–47], or global reaction route mapping (GRRM) combined with microiteration methods for large molecules[48]. Algorithms have been developed that combine double-ended interpolation methods with TS refinement[49, 50]. Single-ended methods have also been developed, which require knowledge of only one local minimum[51]. Extensive reviews are available on TS finding techniques[3, 22].

Chain-of-states methods, such as the NEB and SM, involve the creation of a string of images between the reactant and product states, which are then relaxed to the reaction pathway. In the NEB, the forces on each image are projected along and perpendicular to the tangent direction and energy is minimized perpendicular to this direction. Spring forces are artificially introduced between the images to maintain even spacing. String methods, on the other hand, use splines to calculate tangents and maintain node spacing via re-parameterization. The main drawback of these methods is that multiple gradient calculations must be per-

formed on images located far away from the TS. To reduce the computational burden of such calculations for applications involving electronic structure theory, the GSM was developed. In this method, the search begins with only the reactant and product configurations, and the two string segments are grown independently until they join together. Once a new node is optimized with respect to the gradient in the direction perpendicular to the approximate reaction path, the string is re-parameterized. In order to obtain a reasonable guess of the TS, the re-parameterization and optimization steps are repeated for the completed string, or for a substring that contains the guess to the TS.

Very recently, we have introduced the Freezing String method (FSM) as an algorithm that attempts to avoid the costs associated with both the re-parameterization as well as the iterative steps of the GSM. In the FSM, the newly created nodes are optimized in a direction perpendicular to the reaction coordinate with a few conjugate gradient (CG) steps, and are then irreversibly frozen in place from the path ends going inwards until the ends meet. The FSM therefore is able to generate a guess for the transition state with significantly lower cost, quantified by the number of gradient calculations, compared to the GSM, as it removes the iterative refinement of the fully grown string. As a consequence, the FSM does not reproduce the IRC, and does not provide any guarantee that the TS guess will have the appropriate hessian structure. However, in practical applications, the FSM has proved computationally highly efficient and satisfactorily robust. It is an open question, however, whether or not further improvements in the efficiency of the FSM are possible by modifying the perpendicular search protocol. The first purpose of this paper is to explore this question.

Turning to the second stage of a TS search, of the local TS refinement methods, partitioned-rational functional optimization (P-RFO) is an efficient technique based on separation of the hessian eigenvalues into modes with negative curvatures along which energy maximization is carried out, and all other modes along which the energy is minimized. Therefore P-RFO requires an initial hessian with a single negative eigenvalue along the reaction coordinate in order to ensure convergence to the near-by TS. The P-RFO search may not lead to the desired TS if all the hessian eigenvalues are positive, because the smallest positive eigenvalue is chosen as the mode for energy maximization, which may not correspond to the reaction coordinate. The same issue arises if the hessian possesses multiple negative eigenvalues of similar magnitude, where the most negative eigenvalue is followed uphill even if it may not correspond to the reaction coordinate. Moreover, a P-RFO calculation may fail if the hessian is not evaluated with high fidelity even if the TS guess is good, because errors in the sign of eigenvalues lead to the same ambiguity in identifying which mode to follow uphill. In routine calculations, therefore, the exact second derivative matrix is typically calculated for the TS guess as an input to the P-RFO algorithm to ensure that the input is reliable.

Just how severe is the requirement of obtaining the exact hessian, or a finite difference approximation to it? The answer, of course depends on the type of PES that one is exploring: the answer can be very different for an empirical force field potential versus one based on

quantum mechanics (QM) such as density functional theory (DFT)[24]. Restricting ourselves to QM methods, it is well-known that the computational expense associated with evaluation of the hessian typically scales one power of system size higher than the energy itself or the gradient[52, 53]. Fundamentally, the scaling differences arise from the fact that responses of the unknowns are required with respect to each geometric distortion, whose number scales with the system size. Therefore in practice, analytical hessian or even finite difference hessian evaluations become exceedingly expensive for systems containing a large number of atoms. It is highly desirable to remove the need for explicit evaluation of the hessian, and that is the second purpose of this paper.

We describe here a modified version of the FSM that uses a quasi-Newton line search method for optimization in place of the existing conjugate gradient method. The enhancement in efficiency is measured in terms of the reduction in number of force calculations required to generate the string using the two methods. Information generated by the FSM is then directly incorporated into the construction of an approximate, but entirely appropriate, hessian, which is utilized as input to the P-RFO method in lieu of an exact hessian. The performance of the algorithm with the approximate hessian is compared to that with the exact hessian, in terms of computational time as well as number of optimization cycles. The overall objective is that, by amalgamating the FSM method with the approximate hessian-based transition state search, we can obtain a low-cost, automated transition-state search technique that is particularly useful for studying reactions of large molecules, where exact hessian calculations are prohibitively expensive.

2.3 Methods

2.3.1 Modified Freezing String Method (FSM-BFGS)

The algorithm for the freezing string method (FSM-CG) has been described in detail by Behn et al.[42] The string progresses by alternately adding nodes to two growing substrings that originate respectively from the reactant and product basins on the PES. The FSM terminates when the reactant and product string segments join together. Each node is created via an interpolation step followed by an optimization step.

The interpolation can either be done by a straight line cartesian or a linear synchronous transit (LST) method[54]. The latter is much preferred since LST preserves inter-nuclear distances on interpolation, whereas cartesian interpolation may result in unrealistic bond stretches or bends, and hence, very high energies[55]. Tangent directions are determined at the innermost reactant and product nodes by fitting a spline through the images created by the LST.

In the optimization step, the energy is minimized along the negative perpendicular gra-

dient to the interpolated geometry using the method of conjugate gradients (CG). When the convergence criterion is satisfied, or if maximum number of steps, N_{steps}, is reached, the optimization terminates, and the newly created node is frozen into place. The interpolation and optimization steps are repeated until the reactant and product side strings join.

A modified approach to the FSM is developed here. The original framework of the method, shown in Figure 2.1, remains unchanged. However, the conjugate gradient optimization step is replaced with a quasi-Newton line search method[56], which, in addition to gradient information, builds and utilizes approximate hessian information for optimization of the node in the direction perpendicular to the reaction coordinate. Since the line search is coupled with the Broyden-Fletcher-Goldfarb-Shanno (BFGS) method of updating the hessian, this approach is termed FSM-BFGS.

The quasi-Newton line search procedure incorporated in the FSM is described in Figure 2.2 In this technique, the energy is minimized based on the quadratic approximation

$$E_{k+1} = E_k + \Delta x_k^T g_k^\perp + \frac{1}{2}\Delta x_k^T H_k \Delta x_k \tag{2.1}$$

Here, Δx_k is the stepsize, $g_k^\perp$ is the perpendicular gradient, and H_k is the approximate hessian in the space perpendicular to the reaction coordinate. $g_k^\perp$ is given by

$$g_k^\perp = (I - tt^T)g_k \tag{2.2}$$

where t is the tangent direction determined in the interpolation step. This direction is not updated in the course of an optimization cycle. The quasi-Newton optimization algorithm consists of the following steps:

1. Determine the search direction, s_k , and normalize the direction

$$s_k = -\frac{H_k^{-1} g_k^\perp}{|H_k^{-1} g_k^\perp|} = -\frac{G_k g_k^\perp}{|G_k g_k^\perp|} \tag{2.3}$$

   where G_k is the inverse of the approximate hessian

2. Determine the scaling factor for the step, α_k

3. Take the minimization step by displacing atoms along the search direction in cartesian coordinates

$$x_{k+1} = x_k + \alpha_k s_k \tag{2.4}$$

4. Update the inverse hessian in the perpendicular direction, using the Broyden-Fletcher-Goldfarb-Shanno (BFGS) algorithm[56], which preserves the positive definiteness of the

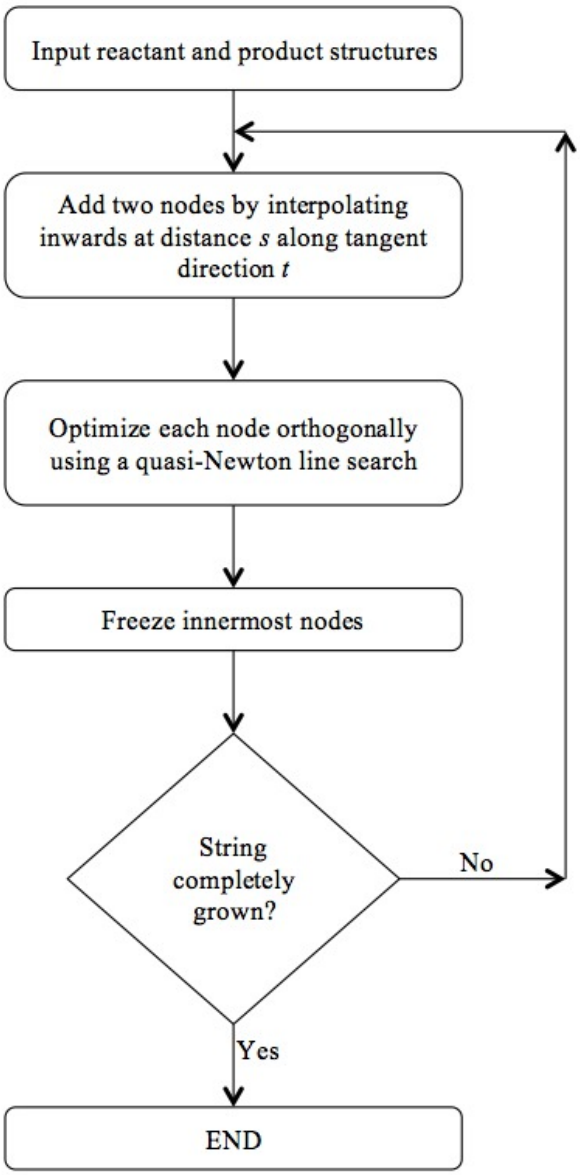

Figure 2.1: Algorithm for the freezing string method, where the conjugate gradient optimization (FSM-CG) step is replaced with the quasi-Newton line search technique (FSM-BFGS).

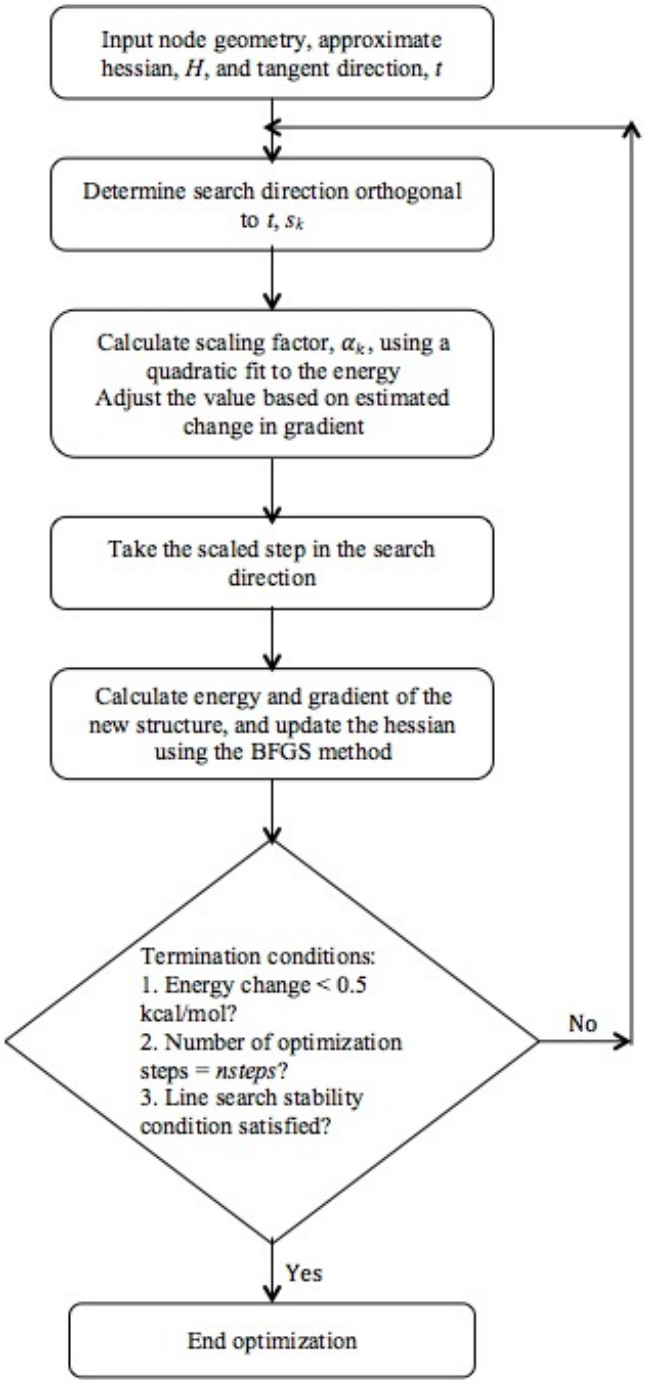

Figure 2.2: Algorithm for quasi-Newton line search optimization in the FSM-BFGS method.

matrix. At the start of the FSM algorithm, both reactant and product side hessians are initialized to identity matrices.

$$\gamma_k = g_{k+1}^{\perp} - g_k^{\perp} \tag{2.5a}$$

$$\delta_k = x_{k+1} - x_k \tag{2.5b}$$

$$G_{k+1} = G_k + \left(1 + \frac{\gamma_k^T G_k \gamma_k}{\delta_k^T \gamma_k}\right) \frac{\delta_k \delta_k^T}{\delta_k^T \gamma_k} - \left(\frac{\delta_k \gamma_k^T G_k + G_k \gamma_k \delta_k^T}{\delta_k^T \gamma_k}\right) \tag{2.5c}$$

In addition to the termination criteria specified by the FSM-CG algorithm, a condition associated with the stability of the line search is implemented. A line search factor $\sigma \in (0, 1)$ is introduced[56]. The stability condition, shown below, ensures that in the limit of an exact line search the gradient is perpendicular to the search direction.

$$|(g_{k+1}^{\perp})^T s_k| \leq -\sigma (g_k^{\perp})^T s_k \tag{2.6}$$

The line search terminates if this condition is satisfied. If σ is large, the condition is representative of a weak line search. In the current line search implementation, the value of σ is fixed at 0.7 for all test cases.

The scaling factor α_k can in principle be determined by minimizing the objective function for the energy iteratively. This approach, however, is not feasible if expensive electronic structure calculations are involved. Therefore a simple scaling factor evaluation is implemented. The ceiling value α_{max} is determined by imposing a constraint of 0.05 Å on the maximum possible step taken along any coordinate direction[57].

$$\alpha_{max} |s_k^{max}| \leq 0.05 \tag{2.7}$$

where $|s_k^{max}|$ is the magnitude of the maximum component of the search direction vector. The FSM-CG algorithm also imposes a maximum step-size constraint of 0.05 Å. The scaling factor is then evaluated using the following expression[56]

$$\alpha_k = -\frac{2\Delta E}{(g_k^{\perp})^T s_k}, \quad \text{where} \quad \Delta E = max(E_{k-1} - E_k, \epsilon) \tag{2.8}$$

Here ϵ is an approximate lower limit on the desired change in energy, and is a fixed parameter in the algorithm. The value of ϵ is set to a fixed value of 2.5 kcal/mol for systems where the difference in energy between reactant and product structures is of higher order of magnitude. However, in cases such as particular rotation or isomerization reactions, where the reactant and product configurations are similar in energy, this value is set to the difference in energy itself. The scaling factor is further refined by an a priori verification of whether the stability condition is satisfied. The Taylor series expansion for the gradient iterate is given by

$$g_{k+1}^{est} = g_k^{\perp} + \alpha_k G_k^{-1} s_k \tag{2.9}$$

By substituting the expression for s_k and taking the inner product with s_k on both sides,

$$s_k^T g_{k+1}^{est} = s_k^T g_k^{\perp} \left(1 - \frac{\alpha_k}{|G_k g_k^{\perp}|} \right) \tag{2.10}$$

The expression on the right hand side in parenthesis must be less than σ. The value of α_k is adjusted accordingly. However, if the adjusted value exceeds α_{max}, the ceiling value itself is used to determine the step size. This step ensures that the scaling factor is neither too small nor too large in magnitude. If the search becomes unstable, it is immediately indicated by a negative value of the scaling factor, and rectified by re-initializing the hessian to an identity matrix.

2.3.2 Construction of an approximate hessian

The basis for construction of an approximate hessian is that the tangent direction at the TS guess generated by any interpolation algorithm should be a reasonable approximation to the reaction coordinate at the TS. The second derivative of the energy with respect to the tangent direction is a good approximation to the single negative eigenvalue of the hessian. This is already enough to separate the single maximization direction from the other degrees of freedom in which minimization is performed. Standard methods for guessing hessians for minimization[58, 59] can then be employed to yield a better guess for the remainder of the hessian. For example, it is well-established that a unit hessian constructed in delocalized internal coordinates[60] is usually substantially superior to a unit diagonal hessian in Cartesian coordinates.

Specifically, beginning with an initial unit matrix constructed in delocalized internal coordinates[60], the transformation to Cartesian coordinates is carried out using the B matrix[61, 62] according to

$$H_{cart} = B^T H_{int} B \tag{2.11}$$

where the B matrix transforms displacement in Cartesian coordinates to internal coordinates. The product, BB^T, generates the matrix in internal coordinates, H_{int}. The B matrix itself is constructed from the coordinates of the TS guess. The transformation to cartesian coordinates is carried out since the tangent direction is available in this coordinate system, and we can later transform back to delocalized internal coordinates. The eigenvalues of the matrix in cartesian coordinates are all positive by construction. At this stage, we impose the correct structure on the approximate hessian with no additional cost, by removing the component normal to the reaction coordinate from this matrix, followed by a rank-one update with the approximate curvature.

$$H = H_{cart} - (t^T H_{cart} t) t t^T + C t t^T \tag{2.12}$$

The update is carried out such that the curvature, C, is the expectation value of the resulting hessian along the tangent direction. The value of C is obtained by a three-point finite difference interpolation between the TS guess and the two nodes closest and on either side of the guess along the FSM string, say nodes A and B, at distances a and b from the TS guess, respectively. The expression for curvature is given by[63]

$$C = \frac{2E_A}{a(a+b)} - \frac{2E_{TS}}{ab} + \frac{2E_B}{b(a+b)} \tag{2.13}$$

The approximate hessian, therefore, has only one negative eigenvalue, as required. Therefore it is now compatible with automatic TS refinement via the P-RFO algorithm.

The performance of the P-RFO with the approximate hessian input can be contrasted with that using an exact hessian in terms of number of optimization cycles as well as the total CPU time required for convergence. Since the approximate hessian is determined with no additional electronic structure calculations, the cost of calculating this hessian compared to the exact hessian is nearly zero.

2.3.3 Computational details

A test suite consisting of 9 reactions was chosen for this study, as summarized in Table 2.1. The broad categories of bond formation or dissociation, rearrangement, ring opening or formation, and isomerization reactions are encompassed in this test set. The size of the test system ranges from 4 to 56 atoms. Basis sets ranging from STO-3G to 6-31G** are used along with either wave function theory (HF) or density functional theory (B3LYP). The reactions in Table 2.1, listed in order of increasing system size, are used to test both the efficiency of FSM-BFGS as well as the performance of the transition state search using the approximate hessian relative to the exact hessian. The efficiency of FSM-BFGS relative to FSM-CG is evaluated in both the steps of TS search based on several parameters. In the TS guess generation step, the methods are contrasted based on the number of gradient calculations required to generate the guess, as well as the number of negative eigenvalues of the exact hessian at the guess, which indicates the quality of the guess structure. In the TS refinement step, the performance of the P-RFO method with the approximate and exact hessians at the TS guess are contrasted for the guess structures generated by both FSM-CG and FSM-BFGS. The two FSM methods are compared based on the number of optimization cycles required by the P-RFO to converge to the true TS structure. The efficiency of the approximate hessian is evaluated based on the computational time saved by sidestepping the exact hessian computation.

All calculations were performed with a developmental version of Q-Chem[65]. The FSM requires optimized reactant and product structures as input. In addition, the user can specify both the desired number of maximum steps per optimization, given by *ngrads*, and the node spacing, given by *nnodes*. The node spacing is determined by dividing the distance between

Reaction	**Description**	**Number of atoms**	**Basis set**	**Theory**
formaldehyde decomposition	$H_2CO \leftrightarrow H_2 + CO$	4	6-31G	B3LYP
silane formation	$SiH_2 + H_2 \leftrightarrow SiH_4$	5	6-31G	B3LYP
ethanal rearrangement	$CH_3CHO \leftrightarrow CH_2CHOH$	7	STO-3G	HF
ethane dehydrogenation	$CH_3CH_3 \leftrightarrow CH_2CH_2 + H_2$	8	6-31G**	B3LYP
bicyclobutane ring opening	bicyclobutane $\leftrightarrow$ $CH_2CHCHCH_2$	10	STO-3G	HF
hexadiene ring formation	cis,cis-2,4-hexadiene $\leftrightarrow$ $3,4-$dimethylcyclobutene	16	STO-3G	HF
Diels Alder reaction	$CH_2CHCHCH_2 +$ $CH_2CH_2 \leftrightarrow$ cyclohexene	16	6-31G	B3LYP
alanine dipeptide rearrangement	$C_5 \leftrightarrow C_{7AX}$	22	6-31G	B3LYP
Ireland Claisen rearrangement[64]	silyl ketene acetal $\leftrightarrow$ silyl ester	56	3-21G	B3LYP

Table 2.1: Test suite of reactions used for both comparison between FSM-BFGS and FSM-CG, and to contrast between TS search with an approximate hessian and that with an exact hessian.

reactant and product structures by this number. For all the reactions studied, *ngrads* is set to 3 and *nnodes* is set to 18. These values are chosen such that a sufficiently smooth string and a reasonable guess structure are generated with minimal computational expense for all the systems under investigation. The inputs to the P-RFO algorithm for TS refinement consist of the TS guess structure, the exact or approximate hessian, and a user-defined ceiling on the optimization step-size, which is set to $0.05a_0$ for all reactions.

2.4 Results and Discussion

2.4.1 Modified Freezing String Method

The efficiency of FSM-BFGS is measured based on the number of gradients required to obtain a string similar to that generated by FSM-CG. The quality of the guess generated, indicated by the number and magnitude of negative eigenvalues in the exact hessian, is also contrasted for the two methods. The results are shown in Table 2.2. Irrespective of the size

of the system, level of theory, or reaction involved, both techniques require less than 100 gradient calculations to produce a complete string. This is already a substantial improvement over iterative NEB or string methods[37]. Barring the exception of ethane dehydrogenation where the FSM-CG hessian has three negative eigenvalues and the FSM-BFGS hessian has two, both methods generate guess structures whose hessians have single negative eigenvalues. As already discussed, this is highly desirable to ensure that the subsequent P-RFO refinement of the TS is successful. The magnitudes of the eigenvalues corresponding to the reaction coordinate are similar in most cases, indicating the similarity of the TS guesses generated by the two methods. From Table 2.2, it can also be observed that the FSM-BFGS method requires far fewer gradient calculations than the FSM-CG technique to generate a similar guess structure using identical input parameters. For the reactions in the test set, the existing FSM-CG method requires 50% more gradients on average compared to the new FSM-BFGS variant.

The quasi-Newton optimization method can determine step sizes more effectively than the conjugate gradient method since approximate hessian information is also incorporated in the line search in addition to gradient information. A moderate line search stability condition, that uses a default value of 0.7 for σ, is sufficient to generate a smooth string in all cases. As a result, the termination condition for the line search is usually satisfied in fewer steps than the enforced upper limit. The FSM-BFGS technique, therefore, reduces computational effort relative to the FSM-CG method for identical input conditions.

The FSM-BFGS method is able to generate a guess for the TS at significantly reduced cost compared to the FSM-CG method. The quality of the TS guess generated by each method is also examined by testing the performance of the approximate hessian for TS refinement.

2.4.2 Transition state search with an approximate hessian

The quality of the approximate hessian is tested based on the total time required for the algorithm to converge to the correct transition state. For the TS search conducted with an exact hessian, the total time includes the time required to evaluate the hessian itself. In addition, the most negative eigenvalue, which indicates the reaction coordinate, is compared between the approximate and exact hessian. The overlap of the approximate and exact eigenvectors corresponding to the reaction coordinate, given by their scalar product, is also calculated. The efficiency of the P-RFO search algorithm with these hessians is compared in delocalized internal coordinates.

The contrast between searches carried out with the exact and approximate hessians with the TS guess generated by the FSM-BFGS algorithm is reported in Table 2.3. The best possible input for a P-RFO search should be the exact hessian. The expectations for relative efficiency of searches performed with an approximate hessian therefore should not be

Reaction	**FSM-CG**		**FSM-BFGS**		**% increase from BFGS to CG**
	Gradients	Negative eigenvalue	Gradients	Negative eigenvalue	
formaldehyde decomposition	94	-0.05	53	-0.27	77
silane formation	73	-0.24	41	-0.23	78
ethanal rearrangement	78	-0.48	61	-0.55	28
ethane dehydrogenation	74	-0.16	58	-0.05	28
bicyclobutane ring opening	70	-0.10	47	-0.07	49
hexadiene ring formation	78	-1.10	55	-1.00	42
Diels Alder reaction	72	-0.05	57	-0.04	26
alanine dipeptide rearrangement	94	-0.003	53	-0.003	77
Ireland Claisen rearrangement[64]	78	-0.25	53	-0.06	47

Table 2.2: Comparison between FSM-CG and FSM-BFGS for generating TS guesses, using identical input parameters ($ngrads = 3$, $nnodes = 18$), based on total number of gradient calculations required to obtain the string, as well as the magnitude of the eigenvalue corresponding to the reaction coordinate (Ha/Bo^2).

too high since the primary purpose of the approximate hessian is to avoid expensive exact hessian evaluations in large systems. The trends are not uniform since the quality of both hessians depends on the nature of the TS guess. In addition, the constructed hessian is based on an approximate reaction coordinate and an interpolated curvature. However, the overall results are promising.

One measure of the quality of the approximate hessian is the overlap between the eigenvector corresponding to the reaction coordinate in the exact hessian with the corresponding vector in the approximate hessian, which can be evaluated as a scalar product of these two vectors. This overlap is greater than 0.5 in most of the test reactions studied, with a fair match between the eigenvalues as well. In general, with the exception of ethane dehydrogenation, the transition-state search performs remarkably well with an approximate hessian

Reaction	**Exact hessian**			**Approximate hessian**				**CPU time reduced (%)**
	-ve eval	Cycles	CPU time (s)	d.p.	-ve eval	Cycles	CPU time (s)	
formaldehyde decomposition	-0.27	50	56	0.7	-0.29	44	44	22
silane formation	-0.23	5	14	0.6	-0.45	12	14	-4
ethanal rearrangement	-0.55	74	16	0.0	-2.63	54	11	30
ethane dehydrogenation	-0.05	63	460	0.5	-0.26	148	906	-97
bicyclobutane ring opening	-0.07	129	38	0.7	-0.30	147	41	-10
hexadiene ring formation	-1.00	61	45	0.8	-1.68	67	44	2
Diels Alder reaction	-0.04	63	1367	0.6	-0.23	63	1034	24
alanine dipeptide rearrangement	-0.003	43	2538	0.7	-0.02	51	1890	26
Ireland Claisen rearrangement[64]	-0.06	88	13567	0.3	-2.65	153	12980	4

Table 2.3: Performance of P-RFO with exact and approximate hessian, using the TS guess and hessian generated using FSM-BFGS . "-ve eval" represents the eigenvalue corresponding to the reaction coordinate. "d.p." denotes the scalar product between the eigenvectors corresponding to the reaction coordinate in the exact and approximate hessians.

input, both in terms of number of optimization cycles as well as the total CPU time required for convergence. In the case of ethane dehydrogenation, it is observed that the exact hessian has two negative eigenvalues of similar magnitude. This indicates that the TS guess is not close to the region of the true saddle point, and therefore, the approximate tangent direction may not be effective in guiding the P-RFO. However, the algorithm does converge to the true TS within 150 optimization cycles since the approximate hessian possesses the desired structure of a single negative eigenvalue. The utility of an approximate hessian in saving computational time, however, is distinctly visible for large systems. For systems containing 16 atoms or higher, the exact hessian calculation costs between 10% of the total CPU time in the case of hexadiene ring formation to 45% in the case of Ireland-Claisen rearrangement. In these cases, the reduction in cost associated with sidestepping the exact hessian clearly

outweighs the increase in cost of gradients associated with the use of an approximate hessian.

On similar lines, the performance of the approximate hessian using the TS guess generated by the FSM-CG method is also evaluated. The results are shown in Table 2.4. In most cases, the approximate hessian generated using the FSM-CG algorithm performs just as effectively as that using the FSM-BFGS algorithm, demonstrating the transferability of the approximate hessian construction procedure to any interpolation algorithm. The overlap between the exact and approximate reaction coordinates, however, is slightly poorer on average compared to the FSM-BFGS method. Particularly, in the instances of ethane dehydrogenation and Ireland-Claisen rearrangements, the TS searches with the approximate hessian converge to first order saddle points, which do not lead to the correct reactant and product structures. The TS guesses converge to the true TS with the exact hessian input for these reactions, indicating that the FSM-CG generates a good structure for the TS guess. However, for the same input parameters, the approximate reaction coordinate generated by the BFGS method is better than the CG direction for these reactions.

The approximate hessian calculated using the information generated by the FSM algorithm, therefore, effectively eliminates the need for computation of an exact hessian for TS search. The requirement of an exact hessian for accurate transition state search has been a massive obstacle to determining TSs for systems consisting of hundreds of atoms. While the largest system in this study, the Ireland-Claisen rearrangement, has only 56 atoms, the impact of exact hessian evaluation in that case is already significant. The exact hessian calculation constitutes about 45% of the entire job time when the search is carried out in internal coordinates. If one then doubles the system size, the energy and gradient calculations will scale up by approximately a factor of 4 for these DFT calculations, while the exact hessian calculation will increase by approximately a factor of 8[52, 53]. This illustrates how exact hessian evaluation progresses from being computationally insignificant in the small reactions towards being a severe bottleneck in large systems. The virtue of the approximate hessian approach is the removal of this bottleneck without unduly affecting the convergence of the TS refinement by the P-RFO algorithm.

The overall performance of the combined FSM and approximate hessian-based method, described by the total gradient calculations required for both steps of TS finding, is shown in Figure 2.3. It can be observed that the FSM-BFGS performs better both in terms of accuracy as well as efficiency of finding the TS. Most of the improvement in efficiency arises from the improvement in the string method itself, since the TS guesses generated, and the constructed approximate hessians are similar.

Reaction	**Exact hessian**			**Approximate hessian**				**CPU time reduced (%)**
	-ve eval	Cycles	CPU time (s)	d.p.	-ve eval	Cycles	CPU time (s)	
formaldehyde decomposition	-0.05	59	65	0.6	-0.15	64	64	2
silane formation	-0.24	5	14	0.7	-0.48	12	14	-4
ethanal rearrangement	-0.48	66	14	0.8	-0.22	65	13	6
ethane dehydrogenation	-0.16	193	1256	0.1	-1.20			
bicyclobutane ring opening	-0.1	114	33	0.6	-0.31	117	33	2
hexadiene ring formation	-1.1	54	40	0.5	-1.85	77	51	-25
Diels Alder reaction	-0.05	83	1695	0.4	-0.20	85	1395	18
alanine dipeptide rearrangement	-0.003	36	2279	0.4	-0.007	51	1890	17
Ireland Claisen rearrangement	-0.25	364	36983	0.1	-0.27			

Table 2.4: Comparison between performance of P-RFO with exact and approximate hessian, using the TS guess and hessian generated using FSM-CG. For ethane dehydrogenation, TS search with the exact hessian required a smaller step to converge to the correct TS (0.025Bo).

2.5 Conclusions

The aim of this study is to develop a set of computational techniques that determines transition structures rapidly and accurately, given only reactant and product structures. We have made progress in addressing two of the key bottlenecks in finding transition states: generating the guess to the transition state, and calculating the exact hessian.

The cost of automatically generating an initial guess is reduced by replacing the conjugate gradient technique used in the optimization step of the freezing string method (FSM) with a quasi-Newton line search coupled with a BFGS hessian update. This approach enhances the computational efficiency of the FSM by about 50 % on average for the test suite consisting of a diverse range of reaction types and system sizes without altering the quality

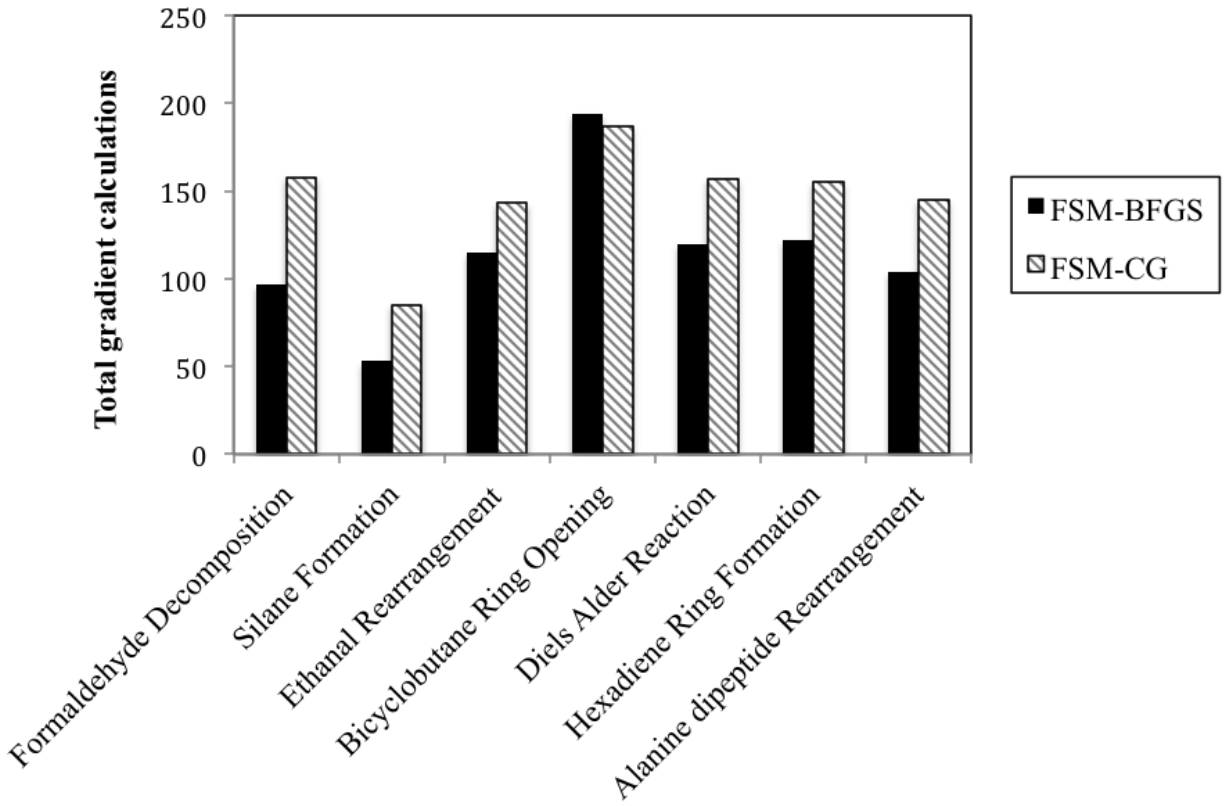

Figure 2.3: Performance of the combination of a string method (FSM-CG and FSM-BFGS) with an approximate hessian-based TS search, based on total gradients to achieve convergence beginning with reactant and product configurations.

of the guess generated. It must be noted, however, that interpolation methods do not follow the reaction path exactly. Therefore, convergence to the correct TS cannot be rigorously guaranteed. The FSM-BFGS method with the current set of parameters may fail in systems more complex than the current test set. In such cases, however, it is possible to tighten the line search using a lower value of , in order to follow the true reaction path more accurately.

The second bottleneck, the exact hessian calculation, is addressed by constructing an approximate hessian using the output of the FSM-BFGS or FSM-CG method, which is then used as an input to the P-RFO algorithm instead of the exact hessian. In addition to the computational benefit of avoiding an expensive exact hessian calculation, the approximate hessian by design possesses the desirable property of a single negative eigenvalue. This means that it can in fact be more appropriate than the exact hessian in cases where the latter does not initially have the correct structure. Despite being approximate, the numerical performance of P-RFO refinements is not degraded by its use. Furthermore, an approximate

hessian-based search in delocalized internal coordinates helps to make the study of reactions of large molecules more computationally viable using electronic structure methods.

2.6 Acknowledgements

Dr. Paul Zimmerman was a collaborator on this project. This work was supported by a grant from Chevron Energy Technology Co.

Chapter 3

A Finite Difference Davidson Procedure to Sidestep Full Ab Initio Hessian Calculation: Application to Characterization of Stationary Points and Transition State Searches

3.1 Abstract

The cost of calculating nuclear hessians, either analytically or by finite difference methods, during the course of quantum chemical analyses can be prohibitive for systems containing hundreds of atoms. In many applications, though, only a few eigenvalues and eigenvectors, and not the full hessian, are required. For instance, the lowest one or two eigenvalues of the full hessian are sufficient to characterize a stationary point as a minimum or a transition state (TS), respectively. In this chapter, we describe a method that can eliminate the need for hessian calculations for both the characterization of stationary points as well as searches for saddle points. A finite differences implementation of the Davidson method that uses only first derivatives of the energy to calculate the lowest eigenvalues and eigenvectors of the hessian is discussed. This method can be implemented in conjunction with geometry optimization methods such as partitioned-rational function optimization (P-RFO) to characterize stationary points on the potential energy surface. With equal ease, it can be combined with interpolation methods that determine TS guess structures, such as the freezing string method, to generate approximate hessian matrices in lieu of full hessians as input to P-RFO for TS optimization. This approach is shown to achieve significant cost savings relative to exact hessian calculation when applied to both stationary point characterization as well as TS optimization. The basic reason is that the present approach scales one power of system size lower since the rate of convergence is approximately independent of the size of the sys-

tem. Therefore, the finite-difference Davidson method is a viable alternative to full hessian calculation for stationary point characterization and TS search particularly when analytical hessians are not available or require substantial computational effort.

3.2 Introduction

The feasibility of applying quantum chemical tools to reaction kinetics studies is severely limited by the size of the system under examination. In particular, the cost of calculating analytical second derivatives, or the nuclear hessian, scales about one power of system size greater than the energy or gradient[52, 53]. In situations where analytical second derivatives are not available, one is forced to use finite differences to evaluate the hessian, which is even more expensive[52, 53]. Although its calculation is costly, the hessian matrix is essential for several reasons. From an analysis of the hessian one can determine whether a stationary point on a potential energy surface corresponds to a minimum or saddle point. Some eigenvector-following optimization techniques, such as the partitioned-rational function optimization (P-RFO) method[2, 6, 44] also rely on an initial hessian input for robust performance and faster convergence. Reaction path searches initiated at the transition state (TS) also require an exact hessian input[66–71].

In most applications, however, it is not the full hessian but only a few eigenvalues or eigenvectors that are necessary. When characterizing stationary points, if the exact hessian matrix has all non-negative eigenvalues, the geometry is classified as a minimum on the potential energy surface. If the hessian has exactly one negative eigenvalue, the geometry corresponds to a TS, with the negative mode representative of the reaction coordinate. In order to verify whether a given geometry corresponds to a minimum or a TS, one only needs to calculate the lowest one or two eigenvalues, respectively. The same principle can be applied to TS search methods that require an initial hessian input. The P-RFO, for example, is more reliable if the hessian input has exactly one negative eigenvalue that resembles the reaction coordinate[3]. Instead of calculating the full hessian, therefore, the lowest eigenvalue and eigenvector are sufficient to generate a matrix input with the correct eigenvalue structure.

Some efforts have been made in this direction, particularly to generate approximate hessians for initiating geometry optimization. Lindh et al.[59] have developed a method in which a model hessian, constructed as a function of force constant parameters, improved the efficiency of geometry optimization via the quasi-Newton-Raphson method. However, the efficiency was tested for only a small basis set and at the Hartree-Fock level of theory, and the model hessian was limited to systems involving atoms in the first three rows of the periodic table. A variational method implemented by Kumeda et al.[72] minimizes the finite-difference formulation of the Rayleigh-Ritz ratio using conjugate gradients. The crudely converged eigenvalue and eigenvector corresponding to the reaction coordinate are then used to initiate eigenvector following methods for TS search. More recently, an eigen-

vector following method that uses the eigensolutions of a finite-difference based Davidson approach has been proposed[73]. The approach uses all the eigensolutions generated by the Davidson method, even if they havent fully converged. As a consequence, the reliability of the saddle-point search based on this approximate hessian remains questionable. The Davidson approach has also been used in a hybrid quantum mechanics/molecular mechanics (QM/MM) approach along with RFO, since it can determine the desired eigenvalues without requiring the storage or calculation of the full hessian[74]. Olsen et al. have also reported the use of a Lanczos scheme for iteratively determining the lowest hessian mode for saddle point search[75]. Reiher and Neugebauer developed a mode-tracking algorithm using the Davidson method for calculating only the modes relevant for vibrational analysis[76]. Similarly, a block-Davidson approach via finite differentiation of the gradient was implemented for calculating hessian-vector products for normal mode analysis[77]. Deglmann and Furche developed a method for stationary point characterization with density functional theory where coupled-perturbed Kohn-Sham equations, the bottleneck in hessian calculation, could be avoided through iterative calculation of hessian-vector products to determine only the lowest eigenvalues[78].

We have previously reported a method that constructs the approximate hessian based on an interpolated curvature obtained from the freezing string method (FSM)[42, 79]. The technique shows promising results when the approximate hessian input is used with P-RFO. However, since the curvature is not optimized, the accuracy of the interpolated curvature and hence the efficiency of optimization relies heavily on the quality of the reaction path generated by FSM, which is not desirable.

The goal of our research is to develop a low-cost alternative to exact or finite difference hessians for applications where only the lowest eigenvalues are required. This paper describes an approach that employs a finite differences form of the Davidson method[80] in conjunction with the P-RFO, which can be applied to both stationary point characterizations as well as TS searches. The Davidson method calculates one or more lowest eigenvalues of a matrix without diagonalizing the full matrix. It does so by diagonalizing a matrix constructed using an orthonormal subspace of size smaller than that of the original matrix, and subsequently minimizing the error between the true and subspace eigensolutions. Any other iterative diagonalization method can also be used instead of the Davidson method for calculating the lowest eigenvalues[81–83].

The P-RFO approach uses quasi-Newton hessian update methods in order to revise the (exact or approximate) hessian input at every step. For stationary point characterization, therefore, the lowest eigenvectors of this matrix at the end of geometry optimization constitute the initial subspace for the Davidson method. Depending on whether the optimization is searching for a minimum or TS, this approach determines the lowest one or two hessian eigenvalues and eigenvectors, respectively, without calculating the exact hessian itself. The Davidson approach is also extended to TS search, for which it uses reaction coordinate in-

formation generated by the FSM to calculate the lowest eigenvalue and eigenvector of the hessian at the TS guess. This information is then incorporated into a guess matrix that is employed as input to P-RFO in lieu of the exact hessian for the TS search. The performance of this method is examined for stationary point characterization and TS search in terms of accuracy, the cost savings it achieves relative to the full hessian calculation, and its scaling with respect to system size. Extensive testing shows that this method requires significantly less computational effort when compared with calculation of the full hessian, and is also nearly independent of system size, making it a very valuable tool for studying large systems.

3.3 Method

3.3.1 Characterization of minima and transition states

The Davidson method has been employed traditionally in situations where the cost of full matrix diagonalization is prohibitive, such as configurational interaction (CI) calculations[84]. However, the original Davidson procedure requires the full matrix in order to determine its eigenvalues. The method therefore needs to be modified in order to apply to calculation of nuclear hessian eigenvalues. It can be made hessian-free by recognizing the fact that the action of the hessian matrix on the subspace vector is desired rather than the matrix itself. This can be determined approximately using finite differences[73].

$$H_{ex}b_1 = y_1 \approx \frac{\nabla E(X_0 + \xi b_1) - \nabla E(X_0 - \xi b_1)}{2\xi} \tag{3.1}$$

where X_0 is the converged geometry, b_1 is the first component of the orthonormal subspace, H_{ex} is the exact hessian, ξ is the finite difference stepsize taken to be 0.01 a_0[43], and ∇E represents gradient of the energy.

The vectors comprising the initial orthonormal subspace, $\{b_i\}$, typically span the dominant components of the desired eigenvalue(s). Depending on whether P-RFO is searching for a minimum or a TS, the subspace can be constructed using the lowest one or two eigenvectors of the updated hessian at convergence, respectively. This choice may not be reliable when the system possesses symmetry, since the initial subspace can be orthogonal to the corresponding lowest eigenvector(s). For systems with symmetry, therefore, we choose the initial guess as a linear combination of the lowest few eigenvectors of the updated hessian at convergence, with randomly determined scalar coefficients. The action of the hessian on the subspace vector(s) is determined from equation 3.1.

For characterization of minima, the first eigenvalue is given by

$$\lambda_1^{(1)} = y_1^T b_1 \tag{3.2}$$

where the superscript corresponds to the current iteration. The residual for the first iteration, therefore is

$$q_i^{(1)} = y_{i,1} - \lambda_1^{(1)} b_1, i = 1, 2, .., 3N \tag{3.3}$$

where N is the number of atoms. Subsequent iterations can be carried out using the standard Davidson procedure[80]. The diagonal elements of the P-RFO updated matrix, H, are used in the preconditioner in order to accelerate convergence towards the desired eigenvalue.

$$w_i^{(M+1)} = (\lambda_1^{(M)} - H_{i,i})^{-1} q_i^{(M)}, i = 1, 2, ..., 3N \tag{3.4}$$

The vector, $w^{(M+1)}$, is then orthonormalized against previous vectors in the subspace to generate the new subspace vector, b_{M+1}, in the M^{th} cycle. If P-RFO has found the minimum correctly, the Davidson approach should converge to an eigenvalue that is greater than or equal to zero. The iterations terminate when one of the following convergence criteria is satisfied:

$$\frac{(\lambda_k^{(M)} - \lambda_k^{(M-1)})}{\lambda_k^{(M-1)}} \leq \xi, \text{or} \tag{3.5a}$$

$$|q_k| \leq \xi \tag{3.5b}$$

where superscript denotes the iteration, λ_k corresponds to the eigenvalue ($k = 1$ for minima), and q_k is the residual corresponding to the kth eigenvalue. When the system has symmetry, only condition (ii) is imposed, with tighter tolerance, ξ^2, in order to ensure that the procedure that begins with a random guess locates the correct eigenvalue.

A subspace consisting initially of two orthonormal vectors is used to characterize TSs. The finite difference expression in equation 3.1 is used to determine the action of the hessian on both b_1 and b_2. The two sets of vectors, (b_1, b_2) and (y_1, y_2), are used to construct the smaller matrix that is then diagonalized. The original Davidson procedure is followed subsequently to obtain the lowest eigenvalue. The search for the second eigenvalue begins with the augmented subspace obtained upon convergence of the first eigenvalue. Convergence of the second eigenvalue is assumed when one of the two conditions in equation 3.5 are satisfied. A more rigorous condition is imposed on the first eigenvalue, requiring both criteria in equation 3.5 to be satisfied for convergence. This is found to be essential, particularly in cases where the P-RFO begins in the absence of any hessian information and as a result, the updated matrix is not a good approximation to the exact hessian. If the optimizer finds the TS correctly, then the lowest eigenvalue determined by the Davidson procedure is negative. The second eigenvalue is zero, since the six eigenvalues following the lowest mode correspond to translations and rotations in cartesian coordinates. A summary of the procedure for characterization of minima and transition states is given in Table 3.1.

3.3.2 Transition state search

The speed and reliability of P-RFO for TS search is vastly enhanced when a hessian input with the correct eigenvalue structure is employed as opposed to a unit-matrix or diagonal-

Stationary point	**Initial subspace $\{b_i\}$ from P-RFO updated hessian, H**	**Convergence conditions (equation 3.5)**
Minimum (no symmetry)	lowest eigenvector	(a) or (b)
Minimum (symmetry)	linear combination of lowest eigenvectors	$\|q_k\| \leq \xi^2$
Transition state	1^{st} eigenvalue - lowest eigenvector	(a) and (b)
Transition state	2^{nd} eigenvalue - second eigenvector	(a) or (b)

Table 3.1: Summary of the finite difference Davidson procedure for characterization of stationary points, for systems with and without symmetry. The lowest eigenvalue is calculated for characterizing minima, and the lowest two eigenvalues for TSs.

matrix input. Although the best input is the exact hessian at the TS guess, it is not always computationally viable. In such cases, an approximate one can be calculated either from force fields or by using a lower level of theory[3].

An approximate hessian with exactly one negative eigenvalue can also be constructed using the finite difference Davidson approach. Any double-ended interpolation method that calculates the TS guess structure from reactant and product geometries also generates an approximate reaction coordinate at the guess. In this case, the reaction coordinate generated by FSM is taken as b_1. The remaining steps are similar to the finite-difference Davidson approach for calculation of the lowest eigenvalue. The criteria for convergence are given by equation 3.5.

The converged eigenvalue and eigenvector must then be incorporated into a guess matrix. There are several possible choices for this guess, the simplest being a unit matrix. However, a better initial guess is one that contains chemical information such as bond stretches, bends, etc. Therefore, a diagonal matrix in primitive internal coordinates, H_{prim}, is transformed to delocalized internal coordinates[60], and subsequently, cartesian coordinates.

$$H_{int} = U^T H_{prim} U \tag{3.6}$$

$$H_{cart} = B^T H_{int} B \tag{3.7}$$

H_{cart} is then updated with the eigenvalue and eigenvector obtained from the Davidson method.

$$H = H_{cart} - 0.5 \sum_{j=1}^{3N} (e_j^T H_{cart} t_1)(t_1 e_j^T + e_j t_1^T) + \lambda_1 t_1 t_1^T \tag{3.8}$$

where e_js are the eigenvectors of H_{cart}, and t_1 and λ_1 are the converged eigenvector and corresponding eigenvalue, respectively. Equation 3.8 removes existing components of the guess matrix along the lowest eigenvector and replaces them with the correct components. The resulting matrix has exactly one negative eigenvalue by design, and serves as a substitute to the exact hessian input to P-RFO.

3.4 Results

3.4.1 Characterization of transition states

The reliability, performance, and scaling of the Davidson method for stationary point characterization is examined with Test Set 1. This set consists of n-butyl lithium initiated butadiene oligomerization transition state and product structures. The converged TS and product geometries for trimerization are shown in Figure 3.1. The TS guesses are generated from the monomer TS[85] by successively adding 1,3-butadiene to the growing chain. In this way, TS guesses for the formation of oligomers ranging from the trimer (44 atoms) to the undecamer (124 atoms) are generated. The guess geometries are then refined to true TS structures with the P-RFO method using exact hessian inputs. The Davidson procedure is applied when the optimization converges. In order to examine the benefit of coupling P-RFO optimization with Davidson characterization, the method is also implemented without using any information from the updated hessian.

All calculations are carried out using a developmental version of Q-Chem 4.1[65], and are run in parallel using 8 cores, each containing 4 GB RAM. Structures in Test Set 1 are treated at the B3LYP/6-31G level of theory[86, 87]. P-RFO searches are carried out in delocalized internal coordinates[60] with an upper limit on step-size per iteration of 0.1 a_0. The cost and accuracy of the Davidson method for calculating the lowest two eigenvalues and thereby characterizing converged TS geometries is compared with the cost of calculating the full hessian.

The CPU time required to calculate the lowest eigenvalues with the Davidson method is determined by multiplying the number of force calculations in the finite-difference steps with the average time to calculate the gradient. This is then compared with the CPU time required for full analytical hessian calculation. For TS characterization, the eigenvalue and eigenvector corresponding to the reaction coordinate are also compared with eigensolutions of the exact hessian in order to verify convergence of the Davidson procedure.

Figure 3.2 compares the cost of full hessian calculation with the Davidson approach for characterizing oligomerization TS's. In all cases, the Davidson approach converges to the lowest eigenvalue within 2% error. The lowest eigenvector is also fully converged as verified by calculating its scalar product with the corresponding eigenvector of the exact hessian.

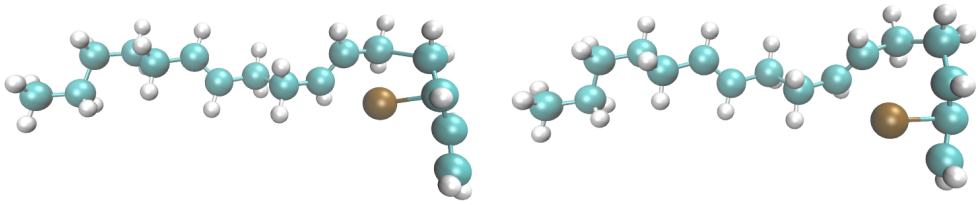

Figure 3.1: Representative structures, TS(left) and product(right) of trimerization of n-butyl lithium, for characterization of stationary points in Test set 1 comprising butadiene oligomers via alkyl lithium initiation. Brown atoms correspond to lithium, cyan represent carbon and white, hydrogen atoms. TS and product structures correspond to 1-carbon attack by 1,3-butadiene of the allyl end of the chain[85]. The chain grows linearly, and all structures correspond to trans isomers.

When the Davidson approach begins with an updated hessian, the initial guess vector is a good approximation to the true reaction coordinate. In addition, preconditioning with the diagonal elements of the approximate hessian facilitates rapid convergence. The method is largely independent of system size, whereas the full hessian scales approximately cubically. For smaller systems, therefore, the Davidson approach is twice as fast as calculating the full hessian, and nearly 5 times faster for the largest system in the test set. On the other hand, if applied independent of the optimizer with no updated hessian information, the Davidson method is much slower to converge. Although computational effort is still lower than full hessian calculation, it is clear that the method is practical only when approximate hessian information, such as the P-RFO update, is available.

Based on these observations, a compromise can be considered that not only guarantees convergence of the P-RFO but also lowers costs associated with hessian calculations, particularly for large molecules. The full hessian can be quickly calculated using a very small basis set prior to TS search. The lowest eigenvalue and eigenvector can then be incorporated into a guess matrix as discussed earlier. The resulting approximate hessian is used for optimization using the P-RFO. This will ensure convergence of the P-RFO to the right saddle point and improve the performance of the Davidson method for characterization by providing a better

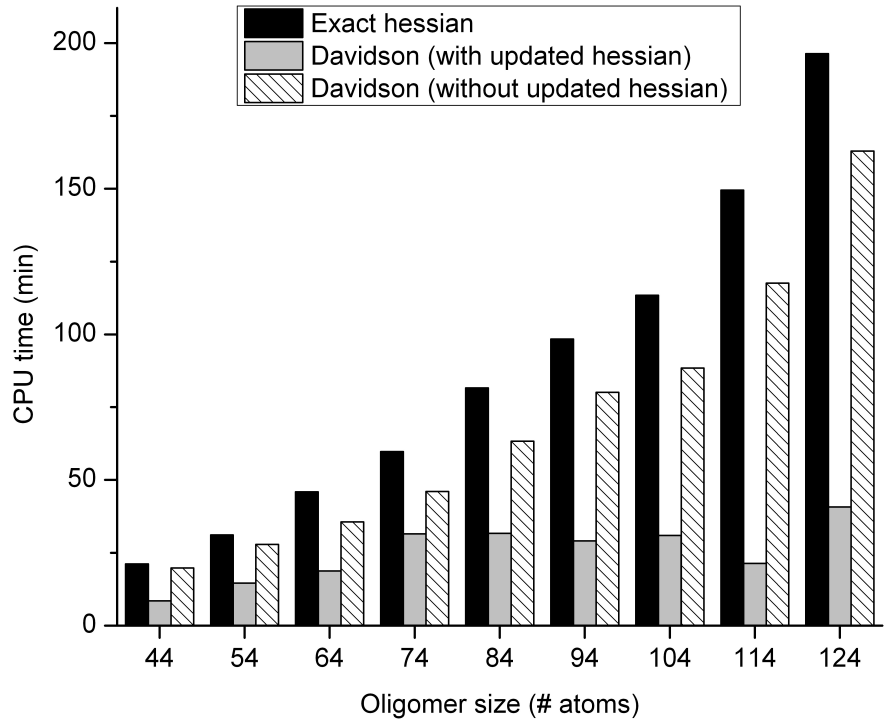

Figure 3.2: Cost comparison between Davidson method and exact hessian calculation for characterization of TSs for Test Set 1. Oligomer sizes are plotted on the horizontal axis. Vertical axis represents computational time (min) associated with either full hessian calculation or Davidson method for finding the two lowest eigenvalues. P-RFO is initiated with an exact hessian input. "with updated hessian" corresponds to when Davidson iterations begin with P-RFO updated hessian. The "without updated hessian" label represents cost of Davidson method with no hessian information.

initial guess of the subspace vector.

In order to ensure that this approach does not incorrectly characterize a higher-order saddle point as a TS, P-RFO optimization is carried out on a decanol molecule with a linear C-O-H bond. The optimization is carried out in the absence of a hessian input, and the system is treated at the B3LYP/6-31G level of theory. The converged structure corresponds to a second-order saddle point, and the hessian consists of two degenerate negative eigenvalues, both of which are correctly calculated by the Davidson method. In addition, this approach is about 1.6 times faster than full hessian calculation. Higher-order saddle points are therefore accurately detected by this procedure.

3.4.2 Characterization of minima

The connectivities of the converged oligomerization TS structures in Test Set 1 are manually modified to resemble the product oligomers. These geometries are then refined to the correct product structure using the P-RFO method. Unlike TS search, all product optimizations are carried out in the absence of exact hessian inputs. The optimization therefore, begins with a diagonal matrix as the hessian guess. The optimization parameters are identical to those for oligomer TS search.

For a minimum on a potential energy surface in cartesian coordinates, the lowest six modes typically correspond to translational and rotational degrees of freedom. Consequently, the eigenvalues corresponding to these modes are zero. In Figure 3.3, the CPU time for full hessian calculation is compared with the time taken by the Davidson approach to converge to one of these modes. For the largest system consisting of 124 atoms, the cost of calculating the hessian is nearly 60 times the cost of the gradient. On the other hand, when the Davidson approach begins with the P-RFO updated hessian, the residual converges in the first finite-difference step itself, incurring a cost equal to only 2 gradients. As a result, the Davidson method with the P-RFO input is between 20 and 29 times faster than the full hessian calculation for this test set. The method is slower to converge without the P-RFO input, similar to what is observed in TS characterization, but still twice as fast as the full hessian for the largest system in this test set.

The efficiency of applying the Davidson procedure is also tested in situations where the analytical hessian is not available. Since finite difference hessians are more expensive than analytical hessians, calculating second derivatives for even small molecules requires significant computational effort. The Davidson approach is tested in one such instance. Geometry optimization of fluoromethane (CH_3F), in the absence of a hessian input, is carried out using MP2/6-311G(d,p) level of theory with P-RFO parameters identical to those used in the oligomer optimizations. The time required to characterize the stationary point using the Davidson method is then contrasted with that for full finite difference hessian calculation. Calculation of the finite difference hessian requires 54.49 s of CPU time. The Davidson procedure can characterize the minimum in 5 iterations with a total CPU time of 7.29 s nearly 7.5 times faster than the finite difference hessian, a gain that will only increase with system size. This approach is therefore not only useful for large molecules for which analytical hessians can become intractable, but also systems that are treated with theory for which analytical hessians are unavailable.

A triflate anion in its eclipsed conformation is a molecule with Cs symmetry. Geometry optimization is carried out in parallel (8 cores) at BP86/6-311+G* level of theory[86, 88]. Although the P-RFO searches for a minimum, it converges to a first-order saddle point with the negative eigenvalue characteristic of a soft mode ($54icm^{-1}$). If the Davidson approach begins with a subspace consisting of the lowest eigenvector of the P-RFO updated hessian, it

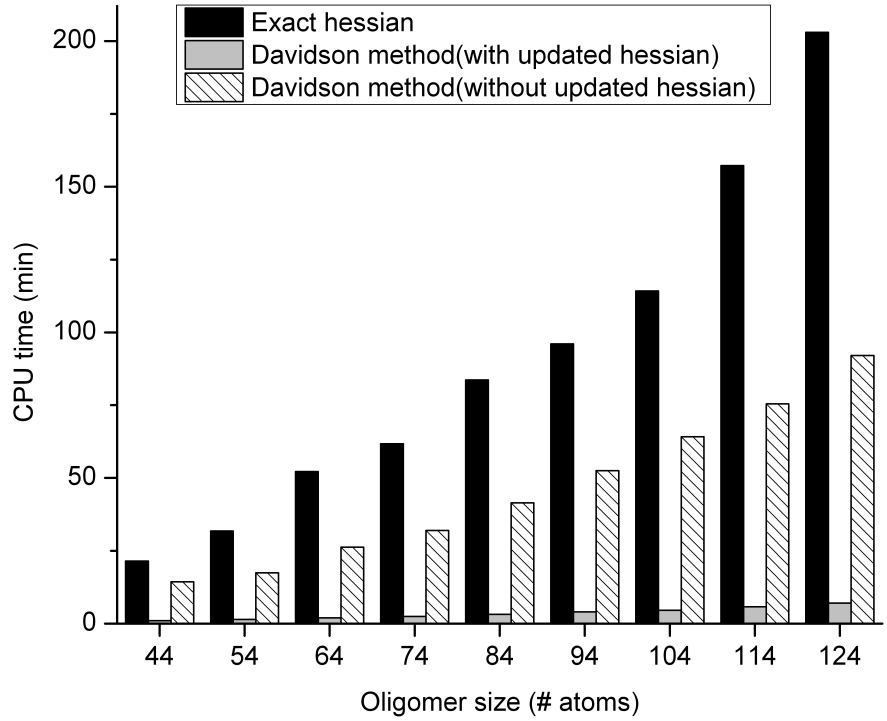

Figure 3.3: Cost comparison between Davidson method and exact hessian calculation for characterization of minima for Test Set 1. P-RFO is initiated without a hessian input, and the optimization begins with a diagonal matrix as a guess hessian.

rapidly converges to an eigenvector that is orthonormal to the soft mode. When the subspace guess is a linear combination of the lowest eigenvectors, it converges correctly to within 3% of the lowest eigenvalue. Although the Davidson approach is more expensive, requiring 39 min (40 gradients), while the full hessian calculation needs only 24 min, the former is expected to scale more favorably with system size.

3.4.3 Transition state search

A diverse set of reactions is chosen to evaluate the cost and performance of the P-RFO with the Davidson-based approximate hessian input relative to that with the full hessian. The reactions comprising Test Set 2, shown in Table 3.2, are largely similar to those used in our previous work[79]. The TS guess structures are generated using FSM with a maximum of three perpendicular steps per iteration and roughly 20 nodes on the string. They are then refined to the correct TSs using P-RFO with both exact hessian as well as Davidson-based

approximate hessian inputs. The two approaches are compared in terms of both hessian as well as optimization costs.

All calculations are carried out using a developmental version of Q-Chem 4.1 on single cores. For ease of visualization, both the hessian and optimization times are divided by the time required to calculate one energy and gradient. The resulting hessian cost is compared to the number of finite-difference steps required in the Davidson procedure. The number of P-RFO cycles required to converge to the correct TS is compared for the exact and approximate hessian inputs to determine whether the use of an approximation adversely affects the performance of P-RFO. TS searches for Test Set 2 are also carried out in delocalized internal coordinates with an upper limit on step-size per iteration of 0.1 a_0. Figure 3.4 shows the total cost of TS search with exact and approximate hessian inputs. The total cost is broken down into two components the cost of calculating the exact/approximate hessian input, and the number of optimization steps required with this input. The results are shown in increasing order of system size.

Analytical hessians are relatively inexpensive for small systems consisting of fewer than 10 atoms. Therefore, the cost of hessian calculation is only a small fraction of total TS search cost. In such cases, the Davidson method does not offer any significant cost advantage. Although there is little benefit to using the Davidson-based hessian, it is interesting to note that the convergence of the optimizer is not adversely affected when an approximation replaces the exact hessian input, as long as it has the correct eigenvalue structure.

As the size of the system increases, the relative contribution of the hessian calculation to the total computational effort also rises. The cost of the hessian calculation is in fact higher than the optimization cost for the largest system in the test set, the dehydration of cellotriose. It can be inferred that further increase in the system size will result in domination of the hessian cost in the total cost of TS search. Significant reduction in computational effort can therefore be achieved by using an approximate hessian that scales more favorably with system size.

In Test Set 2, the cost of approximate hessian construction with the Davidson method does not exceed 9 finite-difference steps, or 18 gradients. Significant savings are achieved for the largest systems, Ireland-Claisen rearrangement and cellotriose dehydration, for which this method is 3.5 and 7 times less expensive than full hessian calculation, respectively. Again, the cost penalty associated with using an approximate input for optimization in place of an exact hessian is small. For cellotriose dehydration, although P-RFO requires 26 more steps to converge with the approximate hessian input relative to the exact hessian, the total cost of the TS search is still less with the approximate input.

The combined performance of the Davidson approach in TS search and optimization is shown in Table 3.3. In addition to the costs associated with hessian construction (labeled

Reaction	**Description**	**Number of atoms**	**Basis set**	**Theory**
formaldehyde decomposition	$H_2CO \leftrightarrow H_2 + CO$	4	6-31G	B3LYP
silane formation	$SiH_2 + H_2 \leftrightarrow SiH_4$	5	6-31G	B3LYP
ethanal rearrangement	$CH_3CHO \leftrightarrow CH_2CHOH$	7	STO-3G	HF
ethane dehydrogenation	$CH_3CH_3 \leftrightarrow CH_2CH_2 + H_2$	8	6-31G**	B3LYP
bicyclobutane ring opening	bicyclobutane $\leftrightarrow CH_2CHCHCH_2$	10	STO-3G	HF
hexadiene ring formation	cis,cis-2,4-hexadiene $\leftrightarrow$ $3,4-$dimethylcyclobutene	16	STO-3G	HF
Diels Alder reaction	$CH_2CHCHCH_2 + CH_2CH_2 \leftrightarrow$ cyclohexene	16	6-31G	B3LYP
alanine dipeptide rearrangement	$C_5 \leftrightarrow C_{7AX}$	22	6-31G	B3LYP
Ireland Claisen rearrangement[64]	silyl ketene acetal $\leftrightarrow$ silyl ester	56	6-31G	B3LYP
cellotriose dehydration[89]	1,2 dehydration	66	6-31G	B3LYP

Table 3.2: Test Set 2 for comparing the costs associated with exact and Davidson-based approximate hessian inputs, and cost of TS optimization with these inputs using P-RFO. TS guesses are generated using FSM-BFGS with $ngrads = 3$ and $nnodes = 20$.

Hess.) and subsequent optimization (labeled Opt.) presented in Figure 3.4, the cost of characterization (labeled Char.) with the Davidson method is also shown. The column labeled Total also includes, in parentheses, the total cost if the full hessian is used in place of the Davidson method.

It is interesting to note that characterization costs are relatively insensitive to whether the P-RFO begins with an exact or an approximate hessian. Therefore, as long as the hessian input to P-RFO has the correct eigenstructure and reaction coordinate information, the Davidson approach is both speedy and reliable. For smaller molecules, as observed with approximate hessian construction, the cost of characterization with the Davidson method is typically higher than that of the full hessian. For the largest systems, however, using the Davidson approach for both hessian construction and TS characterization can result in nearly 40% cost reduction relative to using exact hessians.

Cost (#cycles)	**Exact hessian**				**Davidson-based hessian**			
	Hess.	Opt.	Char.	Total	Hess.	Opt.	Char.	Total
formaldehyde decomposition	7	35	12	54 (49)	8	38	14	60
silane formation	8	4	6	18 (20)	6	7	6	19
ethanal rearrangement	4	46	20	70 (54)	8	52	20	80
ethane dehydrogenation	12	34	16	62 (58)	16	39	18	73
bicyclobutane ring opening	6	73	30	109 (85)	8	83	26	117
hexadiene ring formation	7	35	22	64 (49)	10	39	20	69
Diels Alder reaction	20	29	12	61 (69)	10	30	18	58
alanine dipeptide rearrangement	26	44	34	104 (96)	18	34	34	86
Ireland Claisen rearrangement	49	42	24	115 (140)	14	48	24	86
cellotriose dehydration	54	50	22	126 (158)	8	75	16	99

Table 3.3: Costs involved in TS search and chacterization starting with the guess structure, using P-RFO with an exact hessian input and a Davidson-based hessian input. Costs are reported in terms of number of cycles obtained by dividing computational time by the time required to calculate one energy and gradient. Costs for calculation of an exact/approximate hessian prior to optimization, P-RFO optimization, and characterization using the Davidson method are labeled "Hess.", "Opt." and "Char.", respectively. "Total" indicates the sum of all three components, with the values in parentheses corresponding to the total cost if characterization is carried out with a full hessian instead of the Davidson method.

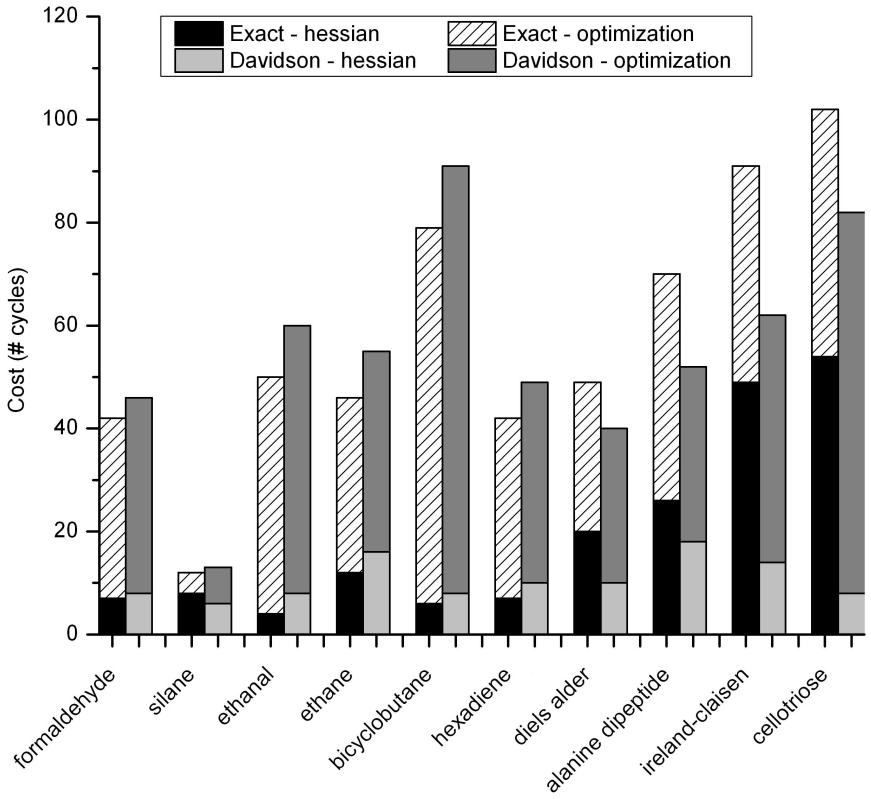

Figure 3.4: Comparison of total costs between TS searches with exact and approximate hessian inputs using Test Set 2. Vertical axis represents computational cost reported in terms of number of equivalent gradient calculations (cycles) by dividing computational time by the time required to calculate one energy and gradient. Total cost is broken down into its 2 components firstly the cost of generating the exact or Davidson-based hessian as inputs to optimization, and secondly cost of optimization using P-RFO with this hessian input.

The finite difference Davidson approach for search and characterization therefore promises significant cost reduction for saddle point searches in systems of very high dimensionality. There is an additional benefit to using a combination of FSM, Davidson-based hessian construction, P-RFO, and subsequent characterization with the Davidson method. The process of finding a TS from reactant and product structures can be fully automated with minimal user intervention, as described in our previous work[79]. However, it must be noted that in situations where the reaction coordinate is strongly coupled to other modes, construction of an approximate hessian with a single accurate eigenvalue may not be sufficient. In such cases, one may have to calculate the full hessian from force fields or by using a lower level of theory[3].

3.4.4 Applications: Catalysis

DFT calculations for studying reactions involving an organometallic complex can be very expensive owing to the presence of one or more metal atoms. In such cases, the cost of calculating the full hessian can be prohibitive. Diaryldithiolene complexes of Co with different aryl substituents have been examined as potential electrocatalysts for proton reduction in the hydrogen evolution reaction (HER), for the conversion of solar energy to fuels[90]. The transition states for the H_2 evolution step in the catalytic cycle with two such complexes are chosen in order to examine the cost reduction achieved using the Davidson approach for TS characterization.

TS optimizations are carried out in parallel (12 cores) using TS guess structures and exact hessian inputs for protonated bromo- and methoxy- derivatives of Co-diaryldithiolene. The system is treated at unrestricted BP86/6-31++G** level of theory[86, 88] with the exception of the Co atom, for which the Wachters+f basis set is used [91]. The structure of the optimized bromo-derivative TS is shown in Figure 3.5. The cost of calculating the full hessian is equivalent to 43 and 160 gradients, corresponding to about 4 and 5.4 days of computational time for the bromo- and methoxy-TS, respectively. On the other hand, the Davidson method converges within 3 iterations (6 gradients) in both cases. It is therefore 7 times faster than the full hessian calculation for the bromo-TS and nearly 27 times faster for the methoxy-TS, demonstrating substantial cost reduction in stationary point characterizations for systems containing metal atoms. It can be argued that since P-RFO begins with an exact hessian, the updated hessian input to Davidson is close to the true hessian, thereby leading to rapid convergence. However, one can also construct an approximate hessian input to P-RFO, using the methods described earlier, without adversely affecting the performance of the Davidson approach, as demonstrated by the results in Table 3.3.

Studying reaction kinetics in the pores of Brønsted acid catalysts such as zeolites can be computationally expensive since the role of the extended framework cannot be neglected[92]. The representation of the catalyst must include the non-reactive pore framework in addition to the active site containing the acidic proton. As a result, TS determination for propane dehydrogenation in H-MFI with even a small 23 tetrahedral (T) atom cluster model involves calculations on a system containing 100 atoms. The T5 region containing the active site and the adsorbate are allowed to relax. Input structures to the FSM consist of reactant and product geometries for the dehydrogenation of propane to propene and hydrogen adsorbed propane and adsorbed propene plus H_2, respectively. The FSM parameters are identical to those used in Test Set 2. The P-RFO step size is 0.05 a_0 and search is carried out in cartesian coordinates. The system is treated at B3LYP/6-31G level of theory and optimizations are run in parallel (12 cores). The optimized TS for propane dehydrogenation in MFI is shown in Figure 3.6.

The cost of calculating the full hessian is equivalent to about 62 gradients, with an

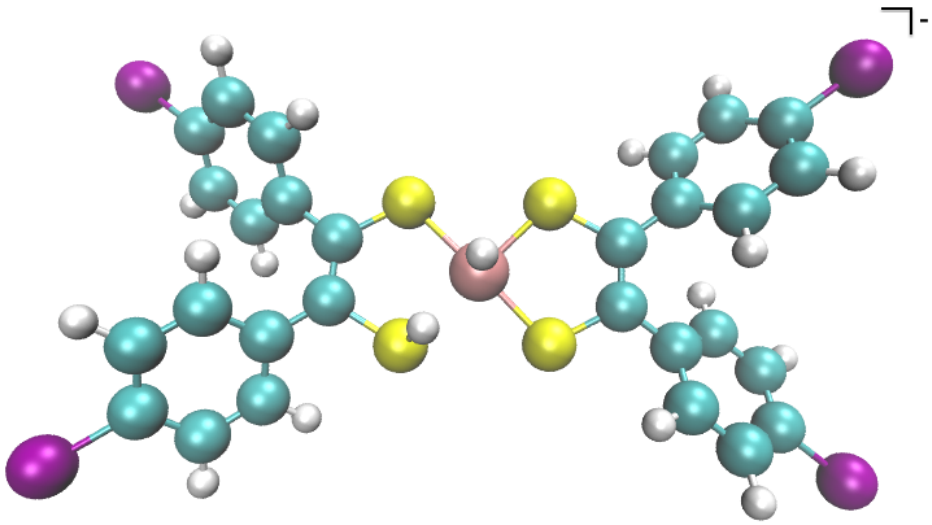

Figure 3.5: Anionic transition state for H_2 evolution of the bromo-derivative of cobalt-diaryldithioline. Cobalt is in the center surrounded by sulfur atoms (yellow), and the aryl groups are para-substituted with bromo groups (violet).

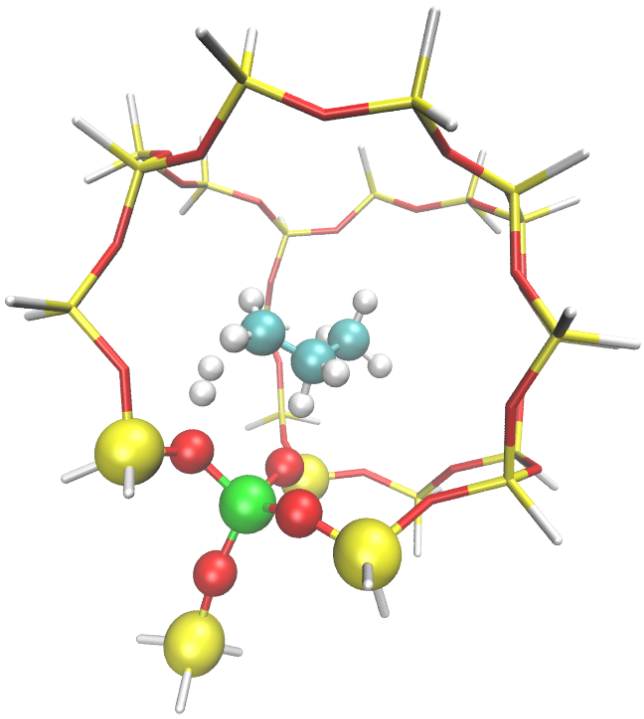

Figure 3.6: Transition state for propane dehydrogenation in a T23 cluster of H-MFI. Yellow atoms correspond to Si linked by O atoms in red, and cluster is terminated with H atoms. The Al atom, shown in green, is representative of the active site where a neighboring O contains an acidic proton. Ball-and-stick representation is used for active site and substrate, which are allowed to relax during optimization.

optimization cost of 263 gradients. The cost of constructing an approximate hessian, on the other hand, is only 10 gradients, and the optimizer performance is similar to that with the exact hessian input, costing 271 gradients. Therefore, even for complex reactions the Davidson method for approximate hessian construction is a viable alternative to full hessian input for the P-RFO, which can not only cut costs associated with hessian computation, but also not degrade the performance of the P-RFO.

3.5 Conclusions

The finite-difference implementation of the Davidson method utilizes updated hessian information generated by P-RFO for stationary point characterization to find the lowest eigenvalues of the exact hessian matrix without actually calculating the matrix itself. This approach performs remarkably well, with significant cost savings relative to full hessian calculation for both minima and saddle point characterization. In addition, the rate of convergence is independent of system size, making this method ideally suited for large molecules. The cost of characterization of the largest test case, the butyl lithium undecamer TS (124 atoms) with the Davidson method is 5 times faster than the full hessian cost, and that of the undecamer product is 29 times faster. The efficiency of this approach is also demonstrated for a small molecule with theory for which analytical hessians are not available and finite-difference hessians are possibly more expensive. A similar procedure is used to construct low-cost approximate hessian inputs for TS optimization with P-RFO. For larger systems where hessian calculation constitutes a large fraction of the total TS search cost, the Davidson approach can significantly lower the hessian component of cost without adversely affecting the convergence of the optimizer. Therefore, the finite-difference Davidson method is a useful tool for both stationary point characterizations as well TS searches, particularly when the system contains a large number of atoms, or when analytical hessians are not available.

3.6 Acknowledgements

This work was supported by a grant from Chevron Energy Technology Co.

Chapter 4

Insights into the Kinetics of Cracking and Dehydrogenation Reactions of Light Alkanes in H–MFI

4.1 Abstract

Monomolecular reactions of alkanes in H-MFI are investigated by means of a dispersion-corrected density functional, ωB97X-D, combined with a hybrid quantum mechanics/molecular mechanics (QM/MM) method applied to a cluster model of the zeolite.The cluster contains 437 tetrahedral (T) atoms, within which a T5 region containing the acid site along with the representative alkane is treated quantum mechanically. The influence of active site location on reaction energetics is examined by studying cracking and dehydrogenation reactions of n-butane at two regions in H-MFI — T12, where the proton is at the intersection of straight and sinusoidal channels, and T10, where the proton is within the sinusoidal channel. Transition states are determined using techniques described in Chapter 2 and Chapter 3. Two transition states are observed for cracking: one where the proton attacks the C–C bond and another where it attacks a C atom. Dehydrogenation proceeds via a concerted mechanism, where the transition state indicates simultaneous H_2 formation and proton migration to the framework. Intrinsic activation energies can be determined accurately with this method, although heats of adsorption are found to be higher in magnitude relative to experiments, which is most likely mainly caused by the MM dispersion parameters for the zeolite framework atoms. Intrinsic activation energies calculated for reactions at the T10 site are higher than those at T12 owing to differences in interaction of the substrate with the acid site as well as with the zeolite framework, demonstrating that Brønsted acid sites in H-MFI are not equivalent for these reactions. Apparent activation energies, determined from calculated intrinsic activation energies and experimentally measured heats of adsorption taken from the literature, are in excellent agreement with experimental results.

4.2 Introduction

Zeolites are crystalline microporous aluminosilicates formed by corner-sharing of tetrahedral silicate (SiO_4) units and aluminate (AlO_4) units. Due to the difference in the valences of Si and Al, cations such as protons, metal ions or metal-oxo species balance the anionic charge created by isomorphic substitution of Al for Si in the zeolite framework. When charge-compensation is by protons, zeolites are strong Brønsted acids. The pores and channels in zeolites are typically on the order of molecular dimensions, enabling zeolites to differentiate between molecules of different size and shape. Owing to their high Brønsted acidity and shape selectivity, zeolites find extensive use as catalysts for a broad variety of chemical reactions[8, 9].

An important area of application for zeolites is the cracking of alkanes, a key process in the conversion of petroleum to transportation fuels. Extensive information about the effects of zeolite structure, Si/Al ratio, and particle size has been obtained from experimental studies. Recent advances in the accuracy and efficiency of quantum chemical methods together with increase in computational power have enabled the use of first principles theoretical methods to study the mechanism and kinetics of zeolite-catalyzed alkane cracking. The most widely used method for this purpose is density functional theory (DFT)[93, 94] because the computational time required for this method scales with approximately the third power of the number of atoms, whereas other ab initio methods (e.g. MP2) scale with the fifth power or higher. Electronic structure calculations using DFT, together with efficient transition state search techniques, such as the nudged elastic band method[26, 27], growing string method[37], and freezing string method[42, 79] have made it feasible to carry out computational studies of complex reactions occurring in zeolites[24].

The model used to represent the catalytically active site and the surrounding portion of the zeolite framework and the exchange-correlation functional have been found to influence the accuracy of the heats of alkane adsorption and the activation energies involved in alkane reactions. Owing to high computational cost associated with large systems, small cluster representations of the zeolite were used in early studies of alkane cracking[95–97]. However, recent efforts have revealed that a large part of the zeolite surrounding the Brønsted acid site must be included in order to properly capture the effects of long-range dispersive and electrostatic interaction between the adsorbate and the zeolite framework[92]. It has also been demonstrated that the B3LYP density functional[86, 87] does not capture dispersion effects, leading to inaccurate estimates of both heats of adsorption[98] and activation energies[99]. Therefore, both large cluster models as well as density functionals that correctly describe non-bonding interactions are crucial for the development of an accurate picture of alkane chemistry in zeolites. For example, DFT calculations using periodic boundary conditions can reproduce activation energies and heats of adsorption for light alkanes with reasonable accuracy[100]. Quantum mechanical calculations performed using a 34 T-atom cluster with a density functional that includes short-range dispersion effects[101, 102] such as M06-2X[103],

can also generate accurate heat of adsorption and activation energies for n-hexane cracking in H-MFI.

The improvements in accuracy resulting from DFT calculations performed with large clusters and superior functionals result, however, in a significantly higher computational burden. This consequence has motivated the search for methods that are accurate but less costly. Zimmerman et al.[104] have recently demonstrated that very good estimates for heats of adsorption and intrinsic activation energies can be obtained by using a dispersion-corrected density functional, a large 356 T-atom cluster, and a hybrid quantum mechanics/molecular mechanics (QM/MM) technique[105–107]. In the QM/MM method, the active region of the zeolite along with the adsorbate, is treated quantum mechanically, and the interaction of the adsorbate with the remaining cluster is treated classically. Various QM/MM techniques have been applied to the adsorption and reaction of hydrocarbons in zeolites[108–110] since they allow the use of large and accurate cluster representations of the zeolite with computational time limited only by the size of the QM region.

We present here the results of a theoretical analysis of monomolecular cracking and dehydrogenation of n-butane and other light alkanes in the zeolite H-MFI. We focused first on the cracking of n-butane because this molecule produces a limited number of cracking products and experimentally measured activation energies for n-butane reported by different authors are largely in agreement.[111–113] By contrast, a wide range of activation energies have been reported experimentally for butane dehydrogenation, with some authors reporting values that are lower than those for cracking[112], whereas experiments on the zeolite MOR[114] as well as theoretical studies[96, 97] indicate that activation energies for monomolecular dehydrogenation are either similar to or higher than those for cracking. The lack of agreement on the activation barrier for dehydrogenation suggests that the differences may be due to the presence of Lewis acid sites[115] or the differences in distribution of Brønsted acid sites in H-MFI. Experimental studies on the effects of alkane chain length suggest that intrinsic activation energies are invariant to the length of the alkane chain, and that the observed increase in activity with increasing chain length is due primarily to a rise in the heat of alkane adsorption with chain length.[112, 116] Computational literature consists of models that validate this hypothesis[100], as well as trends of activation energy with respect to chain length that are highly sensitive to the level of theory used in the calculation[95]. Thus, there remains the issue of how chain length affects the kinetics of alkane cracking and dehydrogenation.

The QM/MM method[104] was used to perform DFT calculations on a large cluster representation of Brønsted acid centers in H-MFI. A large basis set and a recently developed density functional, ωB97X-D[117, 118], were used in order to achieve a high accuracy in the calculated heats of adsorption and the activation processes involved in alkane cracking and dehydrogenation. The calculated heats of adsorption and activation energies were compared with experimental results in order to demonstrate the accuracy of the method. The influence

of acid site location on these reactions was examined by comparing intrinsic activation energies at two acid sites T12 and T10. Similar calculations were performed for other alkanes to assess the impact of chain length on intrinsic activation energies. An attempt was also made to rationalize the wide range of activation energies for dehydrogenation of n-butane in the light of computational results.

4.3 Computational methods

A cluster containing 437 T atoms was used to represent the Brønsted-acid site and the surrounding zeolite framework of H-MFI. The Al atom associated with the acid center was placed at either the T12 or the T10 position in the unit cell. The Brønsted-acidic proton associated with the Al in the T12 position is located at the intersection of the straight and sinusoidal channels of H-MFI. It is noted that many previous theoretical studies of alkane cracking have located Al at the T12 site[95, 97], and comparison with the literature is enabled by this choice. The second site for Al, the T10 position, places the Brønsted-acid proton within the sinusoidal channel and hence in a more confining portion of the zeolite than that occupied by the proton associated with Al at the T12 position.

The overall cluster was divided into two regions a T5 cluster centered on the Al atom located at either the T12 or T10 position, and a 432T atom cluster surrounding the T5 cluster. The smaller T5 cluster was treated quantum mechanically, and all atoms except the vicinal Si atoms were allowed to relax during energy minimization. The larger 432T atom cluster was described by molecular mechanics and all atoms in this cluster were maintained at their crystallographic positions. In order to calculate heats of adsorption, a silicalite form of the same cluster model was employed. The QM/MM method and the MM parameters reported by Zimmerman et al.citezimmqmmm were used. Previous studies have shown that this method reproduces the enthalpy of alkene adsorption and the activation barrier for several elementary steps involving alkanes and alkenes obtained from full QM calculations performed using large cluster representations of H-MFI[119].

All calculations were performed using a developmental version of the Q-Chem software package[65]. A triple-ζ polarized basis set, 6-311G** was utilized. Geometry optimizations were carried out using the dispersion-corrected ωB97X-D functional, followed by single point dual-basis energy calculations using a basis set, 6-311++G(3df, 3pd) that includes diffuse functions. A guess for the transition state was obtained using the Freezing String Method (FSM)[42, 79]. In this method, an approximate reaction pathway is obtained by interpolating between the reactant and product. At each interpolation step, energy is minimized in the directions conjugate to the reaction coordinate. The guess obtained is then further refined using the partitioned rational function optimization (P-RFO) technique[6]. Reactant and product configurations were verified to be potential energy minima by vibrational analysis

Distance	T12		T10	
	Central	Terminal	Central	Terminal
C1-C2	1.79	1.77	1.81	1.76
C1-H, C2-H	1.39,1.45	1.37, 1.39	1.43,1.43	1.36,1.42
O-H	1.53	1.57	1.50	1.58

Table 4.1: TS bond distances (Å) for cracking of n-butane via TS1 at T12 (Figure 4.1) and T10 (Figure 4.2) active sites.

that yielded all positive frequencies. Similarly, vibrational analysis on a transition state, which is a first order saddle point, resulted in a single imaginary frequency. Zero point energy corrections were added to all ground state electronic energies. Intrinsic activation energies were calculated for cracking and dehydrogenation reactions of propane, n-butane and n-hexane at both the T12 and T10 acid sites. The rigid rotor/harmonic oscillator (RRHO) approximation was applied to the system in order to compute heats of adsorption at finite temperatures for alkanes ranging from propane to n-hexane.

4.4 Results and discussion

4.4.1 Transition states

Two distinct transition states, designated as TS1 and TS2, were calculated for cracking. TS1 involves the attack of a Brønsted-acidic proton on a terminal or central C-C bond. The TS structures calculated for acid centers associated with Al located at T12 site are shown in Figure 4.1, and those for acid centers associated with Al located at the T10 site are shown in Figure 4.2. The bond distances at both active sites are given in Table 4.1. The alkane molecule is aligned such that the C-C bond that undergoes cracking is located directly over the acidic O-H group. Interatomic distances between the reactive groups are in good agreement with computational literature on alkane cracking for which it is assumed that cracking occurs via proton attack on the C-C bond of the alkane[101, 104]. Virtually identical bond distances were obtained for cracking occurring at the T10 site.

The possibility that butane cracking may involve proton attack on a primary or secondary C atom instead of a C-C bond, suggested by recent theoretical studies, was also investigated[20, 120]. The structures for this transition state, denoted TS2, calculated for cracking occurring at the T12 and T10 sites are shown in Figures 4.3 and 4.4, respectively, and the bond distances are given in Table 4.2. In this case, the substrate is aligned such that the C atom attacked by the proton, C1, is approximately equidistant between O1 and O2. The C-C bond is cleaved by H2, and not by the Brønsted acid proton, H1. The separation between the framework oxygen (O1/O2) and the Brønsted proton is larger by about 0.4Å

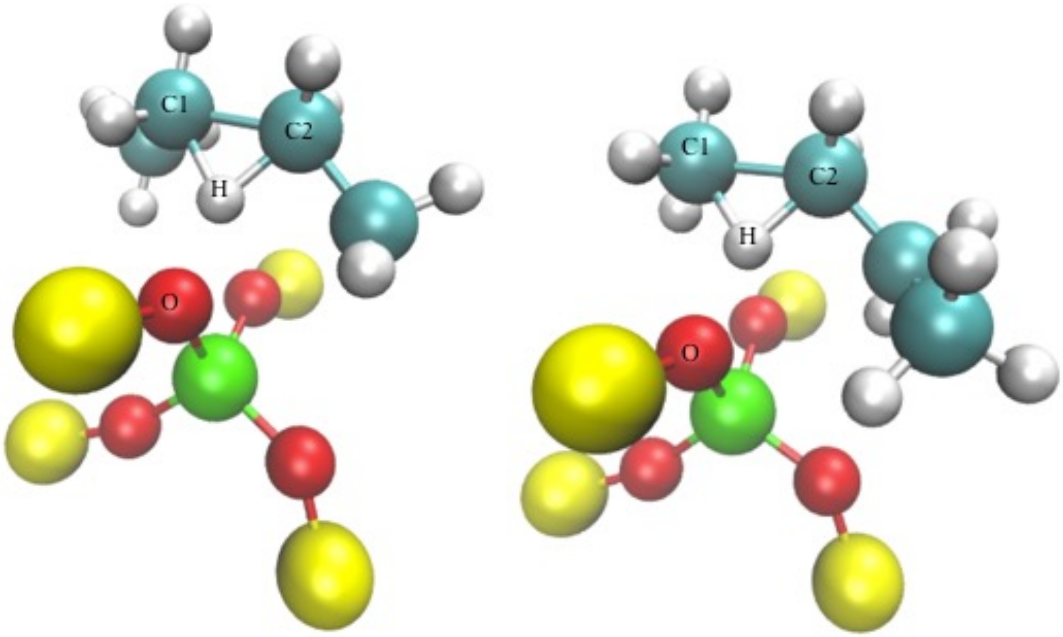

Figure 4.1: Transition states determined for central and terminal cracking of n-butane via TS1 at the T12 site in H-MFI

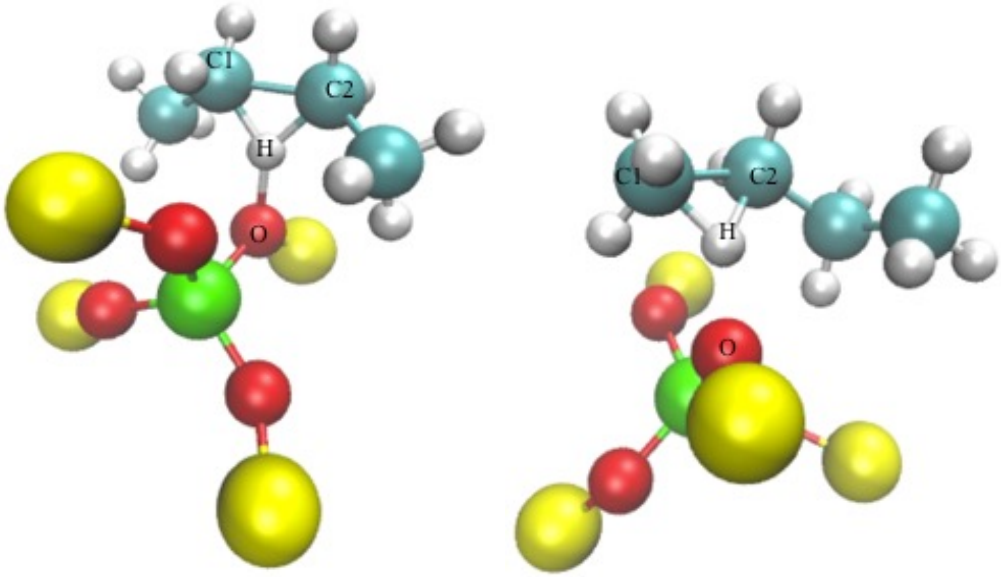

Figure 4.2: Transition states determined for central and terminal cracking of n-butane via TS1 at the T10 site in H-MFI

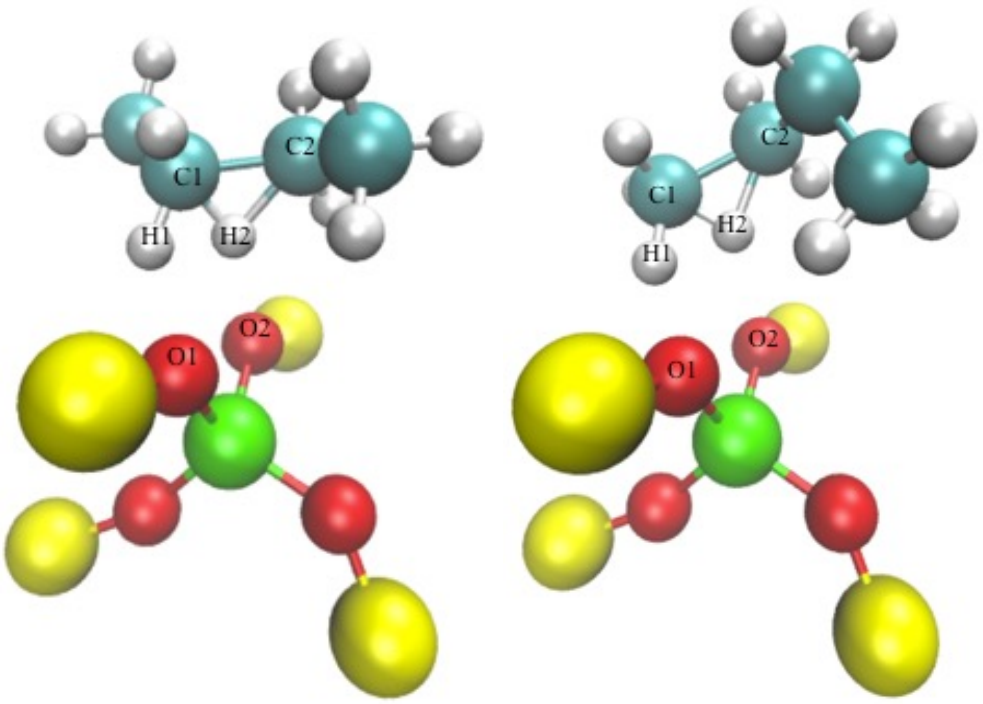

Figure 4.3: Transition states determined for central and terminal cracking of n-butane via TS2 at the T12 site in H-MFI

Distance	**T12**		**T10**	
	Central	Terminal	Central	Terminal
C1-C2	1.70	1.73	1.72	1.75
C1-H1	1.13	1.13	1.12	1.13
C1-H2, C2-H2	1.21,1.48	1.18,1.49	1.21, 1.47	1.18, 1.44
O1-H1	1.98	1.89	2.02	1.88
O2-H2	1.93	2.08	1.87	2.18

Table 4.2: TS bond distances (Å) for cracking of n-butane via TS2 at T12 (Figure 4.3) and T10 (Figure 4.4) active sites.

in TS2 compared to TS1, indicating that the TS2 is a looser transition state compared to TS1.

In the case of dehydrogenation, proton attack occurs at a C-H bond, resulting in the formation of an H_2 molecule and an alkene. The transition states for methyl and methylene dehydrogenation at T12 and T10 sites are shown in Figures 4.5 and 4.6, respectively, with the corresponding bond distances in Table 4.3. The methyl TS results from proton attack on the terminal methyl group, while the methylene TS results from a proton attack on the

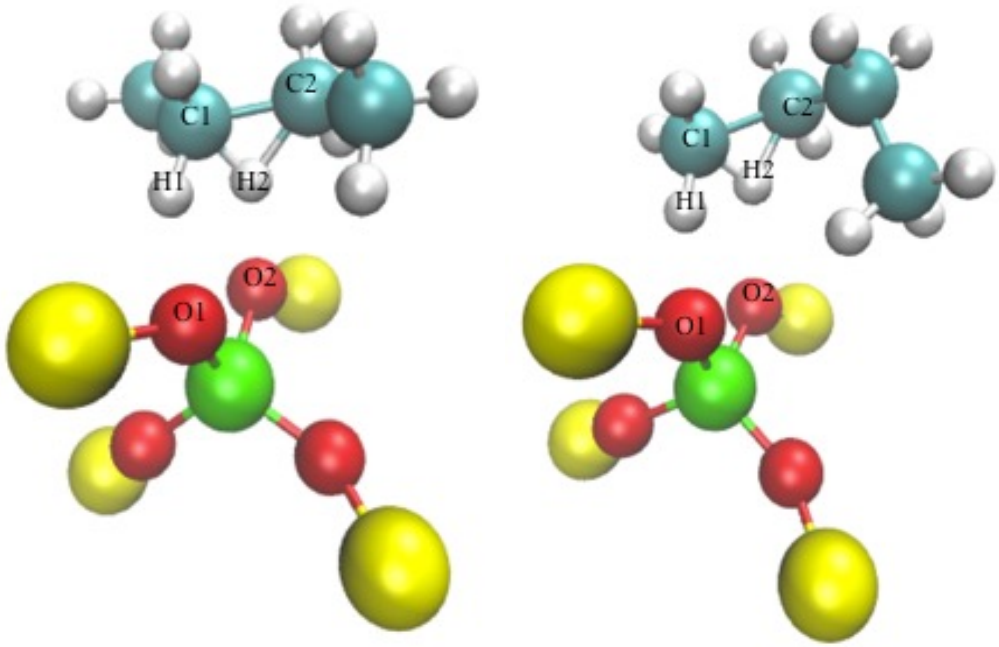

Figure 4.4: Transition states determined for central and terminal cracking of n-butane via TS2 at the T10 site in H-MFI

internal methylene group. The separation between the framework oxygen (O1/O2) and the Brønsted-acid proton is similar to that for cracking via TS2, indicating that dehydrogenation also involves a loose transition state. Table 4.3 shows that the H-H bond distance, 0.77Å (methylene) and 0.78Å (methyl), is very close to the value of 0.74Å for H_2. This indicates that H_2 is close to being fully formed in the transition state. A reduction in the C1-C2 bond length signals the initiation of alkene formation. A natural bond orbital (NBO)[121, 122] analysis of the reactant and transition states showed that the natural charge on H3 is about 67% of the total charge on a Brønsted acid proton. The magnitude of the charge on H3 shows small variations with acid site and pathway, which are reported in Appendix A. Intrinsic reaction coordinate (IRC) calculations were also performed for all dehydrogenation transition states, which confirmed the migration of H3 to the acid site and formation of the alkene. Taken together, these observations indicate that n-butane dehydrogenation proceeds via a concerted mechanism with simultaneous protonation and alkene formation coupled with proton migration to the framework. This mechanism has not been reported in the literature for dehydrogenation of linear alkanes in H-MFI. Previous theoretical studies on propane[96] and n-butane[97] dehydrogenation indicate a multi-step mechanism, with the transition state of the rate-determining step characterized only by the C-H bond cleavage and H_2 formation. The effects of the framework were absent in these studies since they were carried out using T3 and T5 clusters, which may have led to a difference in the mechanism. However, a concerted mechanism has been previously reported for isobutane dehydrogenation on a T5

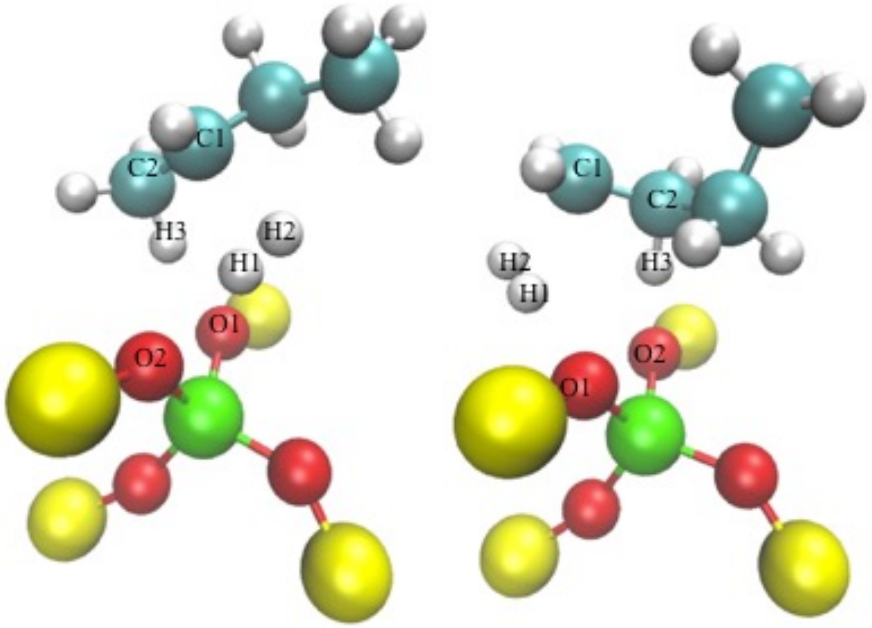

Figure 4.5: Transition states determined for dehydrogenation of n-butane at the T12 site in H-MFI via methylene and methyl routes, respectively.

cluster[123], and for linear alkanes in MFI containing nonframework Ga[124]. In addition to influence of the cluster model and presence of non-framework atoms, the mechanism is also sensitive to pore size. In the case of small-pore zeolites such as chabazite, transition state decay to alkene and H_2 via H-shift has been observed for methyl dehydrogenation of propane using a periodic model[125]. As with cracking, interatomic distances do not vary significantly with acid site location. All transition states were calculated on a potential energy surface at 0 K. However, dynamic effects arising from high reaction temperatures[20, 120, 125] can be quite significant in determining reaction pathways and product selectivity. Although temperature-induced dynamic effects were beyond the scope of this study, it is a potential area for future research.

4.4.2 Intrinsic activation energy

Table 4.4 lists the intrinsic activation energies for butane cracking (TS1) and dehydrogenation determined at the T12 acid site. Activation energies based on calculations performed in the absence of the MM region are reported in parentheses, which are compared with the results reported by Ding et al.[97] done using a T5 cluster to represent the Brønsted-acid center in H-MFI. In general, the activation energies calculated using the B3LYP functional are lower than those calculated using the ωB97X-D functional because the B3LYP functional suffers from a significant amount of self-interaction error[126]. The ωB97X-D functional reduces self-interaction error by introducing a range separation parameter in order to treat

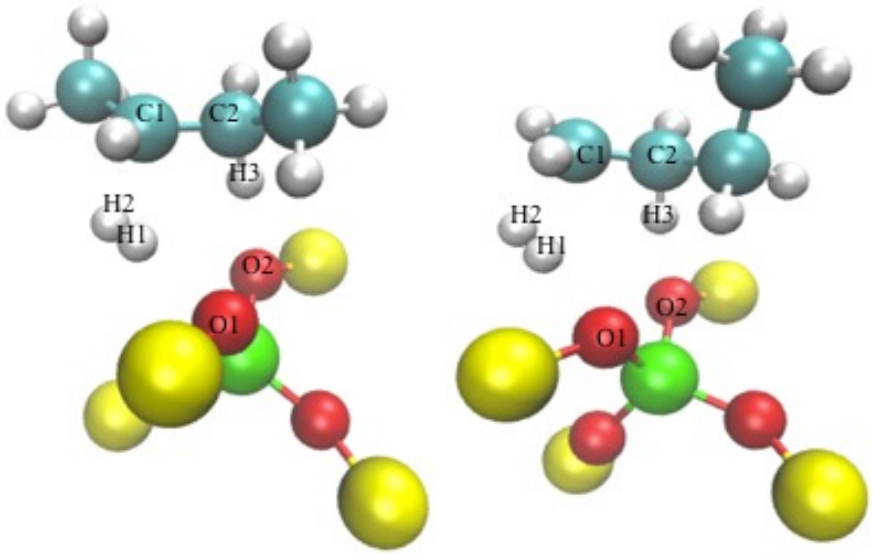

Figure 4.6: Transition states determined for dehydrogenation of n-butane at the T10 site in H-MFI via methylene and methyl routes, respectively.

Distance	**T12**		**T10**	
	Methylene	Methyl	Methylene	Methyl
C1-C2	1.45	1.42	1.46	1.42
C1-H2	1.91	1.84	1.80	1.83
C2-H3	1.12	1.14	1.11	1.14
H1-H2	0.77	0.78	0.77	0.78
O1-H1	1.89	1.96	2.07	2.02
O2-H3	1.97	1.76	1.96	1.97

Table 4.3: TS bond distances (Å) for methylene and methyl dehydrogenation at T12 (Figure 4.5) and T10 (Figure 4.6) active sites.

Source	**QM/MM**	**Tranca et al.[100]**	**Swisher et al.[95]**	**Ding et al.[97]**
Cluster size	T5 QM/ T432 MM	Periodic	T23 QM	T5 QM
Theory	ωB97X-D/ 6-311G**	RPBE	B3LYP/ SV(P)	B3LYP/ 6-311+G(3df,2p)
Central cracking	42.5 (54.9)	-	47.8	51.9
Terminal cracking	45.3 (55.2)	47.2	48.8	56.9
Methylene dehydrogenation	45.4 (63.2)	-	-	57.8
Methyl dehydrogenation	60.2 (73.0)	-	-	70.8

Table 4.4: Intrinsic activation energies (kcal/mol) for n-butane cracking (TS1) and dehydrogenation at the T12 site compared with values reported in computational literature.

short-range and long-range exchange interactions independently. It also includes an empirical dispersion correction that accounts for long-range attractive interactions, which are not taken into account in the B3LYP functional. These differences in functionals manifest themselves not only in the absolute values of the activation energies, but also in the differences in the activation energies between the alternative pathways for cracking and dehydrogenation. The differences in the observed mechanisms for dehydrogenation may also be a contributing factor to dissimilarities in activation energy. The QM/MM cracking activation energies are also compared with QM calculations carried out using a T23 cluster and the B3LYP functional by Swisher et al.[95] The values reported by these authors are higher by 3-5 kcal/mol than those reported here. In addition to the differences in cluster size and density functional, this deviation can be ascribed to the use a smaller basis set, SV(P). Within error, the calculated activation energy for terminal cracking is in agreement with more recent calculations on a periodic model using the RPBE functional by Tranca et al.[100] In summary, the data presented in Table 4.4 emphasizes the importance of using sufficiently large zeolite representations, an exchange-correlation functional that properly accounts for effects of dispersion and long-range interaction errors in the QM region, as well as the importance of accounting for long-range effects of dispersive and electrostatic interactions of adsorbed species with the zeolite framework. The latter effects can lower the activation barrier by as much as 17 kcal/mol and therefore, cannot be neglected.

4.4.3 Influence of acid site location

A recent computational study indicated that activation energies for cracking in MFI are a strong function of the location of the acid site[104]. The influence of acid site location on reaction energetics, therefore, was investigated by comparing intrinsic activation energies for butane cracking and dehydrogenation at two distinct acid sites. Results for the T12 and T10 sites are shown in Table 4.5. The "QM/MM" values denote results obtained for the full cluster model. The "QM/MM-partial" values were obtained by calculating electronic energies and zero-point corrections for the QM/MM-optimized transition states in the absence of non-bonding interactions (electrostatic and dispersive) between the framework and substrate. An approximation to the activation energy lowering due to non-bonding interactions of the substrate with the zeolite framework can be obtained by the difference between these two values. In the absence of these interactions, the activation energies for all cracking pathways do not vary significantly (less than 2.2 kcal/mol) with acid site location. The observed difference between T12 and T10, therefore, arise from the orientation of the transition state with respect to the channels in the zeolite, which are shown in Figures 4.7 and 4.8 for central cracking, and Figures 4.9 and 4.10 for terminal cracking. Since the framework contribution to activation energy lowering is larger at the T12 site than the T10 site (2.6 to 3 kcal/mol for central, 1.9 to 2.2 kcal/mol for terminal cracking), the cracking activation energies are lower at the T12 site. Unlike cracking, the activation energies determined in the absence of non-bonding forces for both dehydrogenation mechanisms are higher at the T10 site by about 3 kcal/mol relative to the T12 site. Although there are differences in orientation of the TS, as shown in Figures 4.11 and 4.12, the contribution of the framework is similar at both the acid sites. Dehydrogenation transition states, therefore, vary in the nature of the interaction of the substrate with the acid site but not so much with the framework environment. The difference in QM/MM activation energies between the two acid sites for dehydrogenation translates to approximately an order of magnitude difference in rate coefficients at 773 K, assuming that the pre-exponential factors are identical.

From these results, it can also be seen that the contribution of the framework in lowering the activation energy is generally greater in the case of looser transition states, i.e. cracking via TS2 and dehydrogenation reactions. It is therefore hypothesized that a looser transition state can orient itself more readily so as to maximize its stabilization through non-bonding interactions with the framework. It is also shown, as reported in Appendix A, that the contribution of dispersion interactions is negligible compared to electrostatic forces in lowering the activation energy for all the reactions studied.

Intrinsic activation energies were calculated for cracking (TS1) and dehydrogenation reactions of propane and n-hexane in order to capture trends with respect to chain length. The trends in activation energies at the T12 and T10 site are shown in Figures 4.13 and 4.14, respectively. Activation energies for propane and n-hexane are comparable to those calculated for n-butane within computational error, demonstrating the invariance of intrinsic

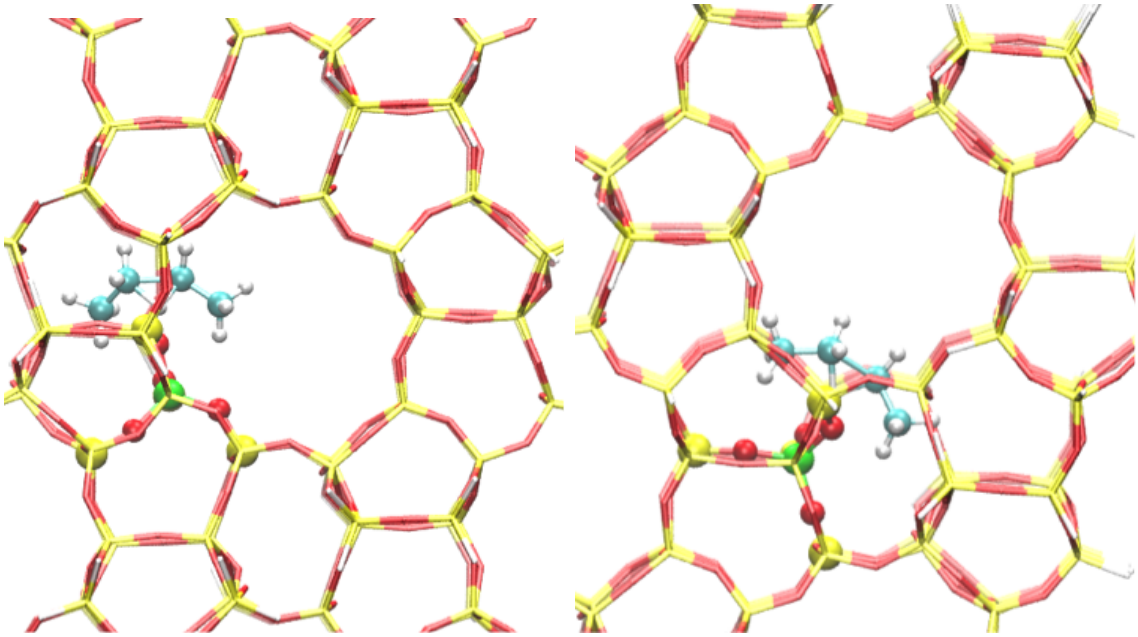

Figure 4.7: Alignment of the central cracking transition state (TS1) within the zeolite framework at the (a) T12, and (b) T10 acid site.

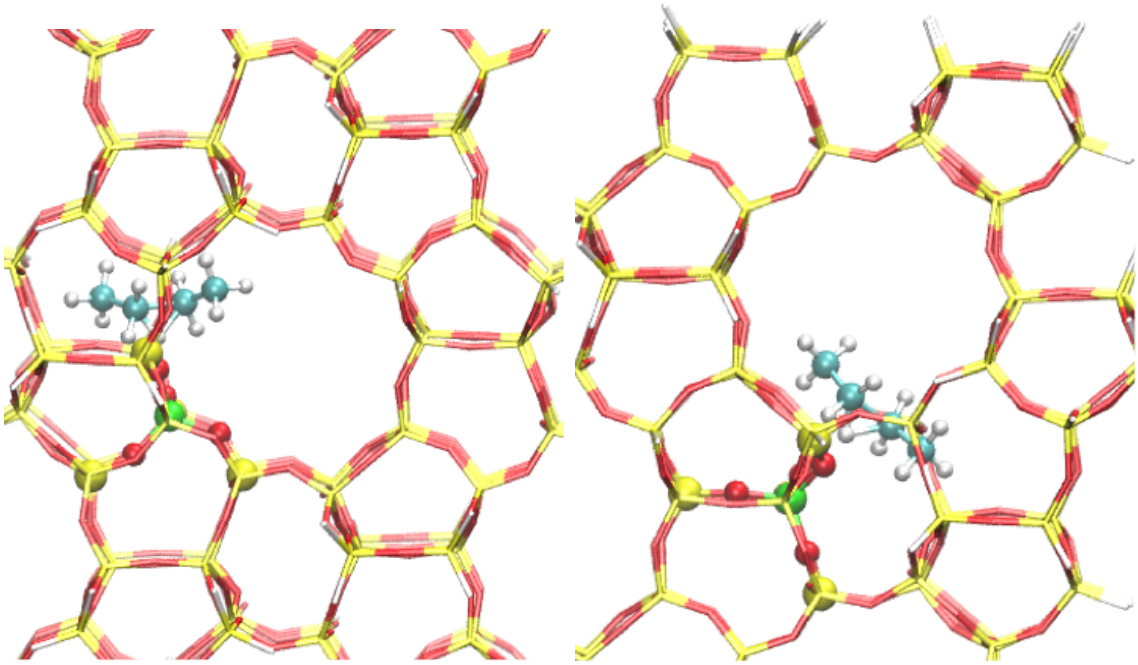

Figure 4.8: Alignment of the central cracking transition state (TS2) within the zeolite framework at the (a) T12, and (b) T10 acid site.

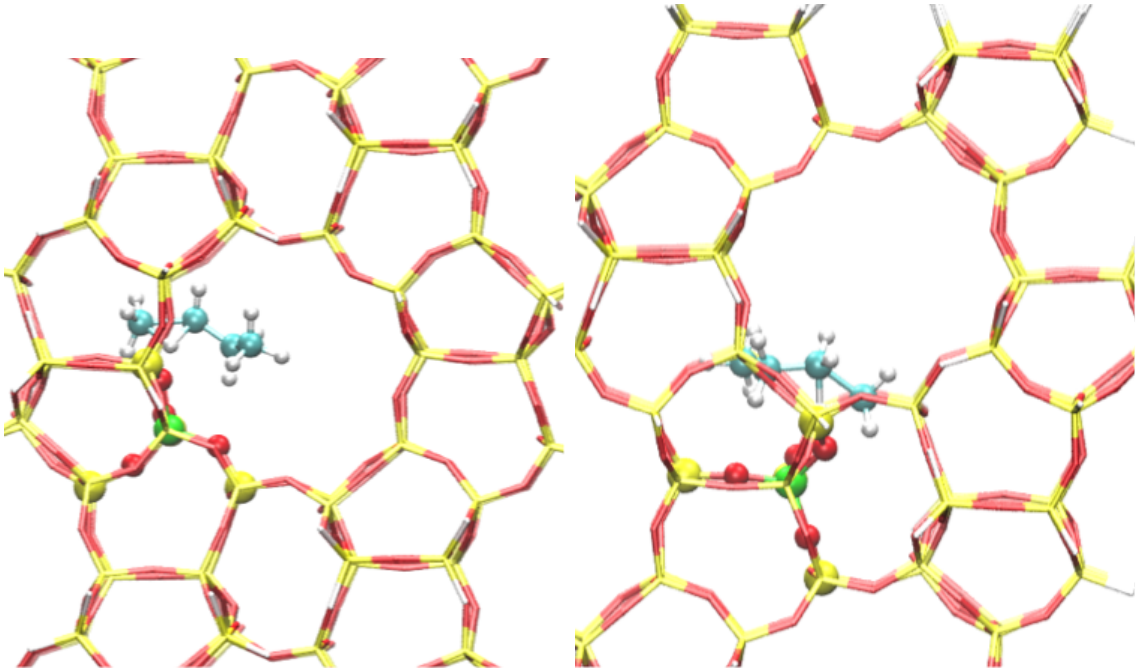

Figure 4.9: Alignment of the terminal cracking transition state (TS1) within the zeolite framework at the (a) T12, and (b) T10 acid site.

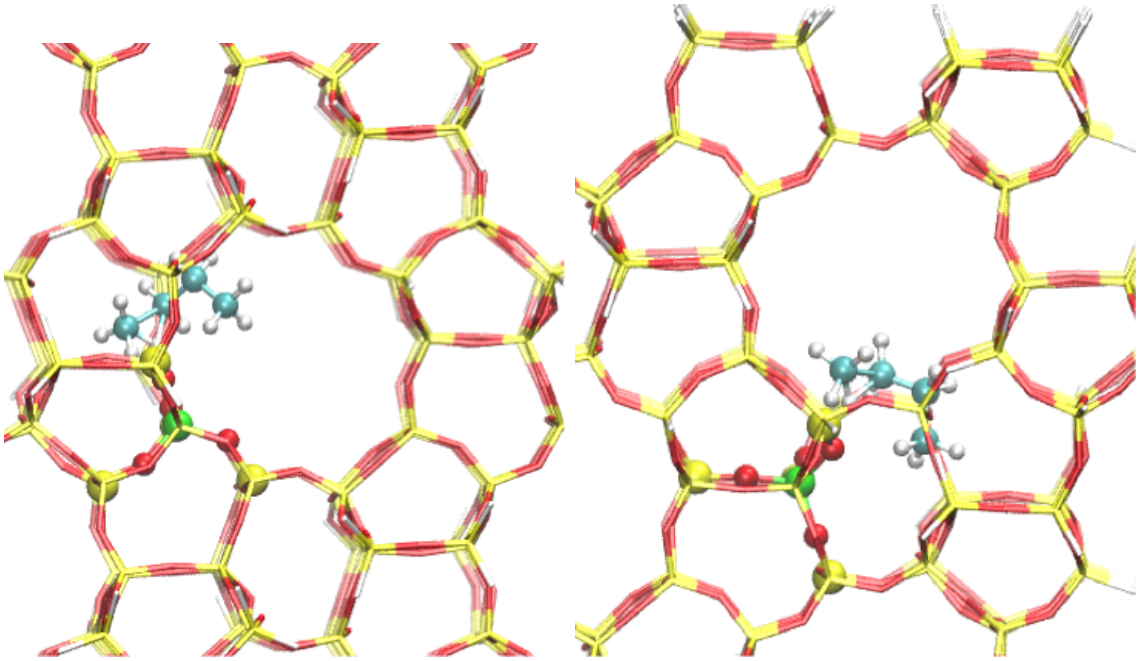

Figure 4.10: Alignment of the terminal cracking transition state (TS2) within the zeolite framework at the (a) T12, and (b) T10 acid site.

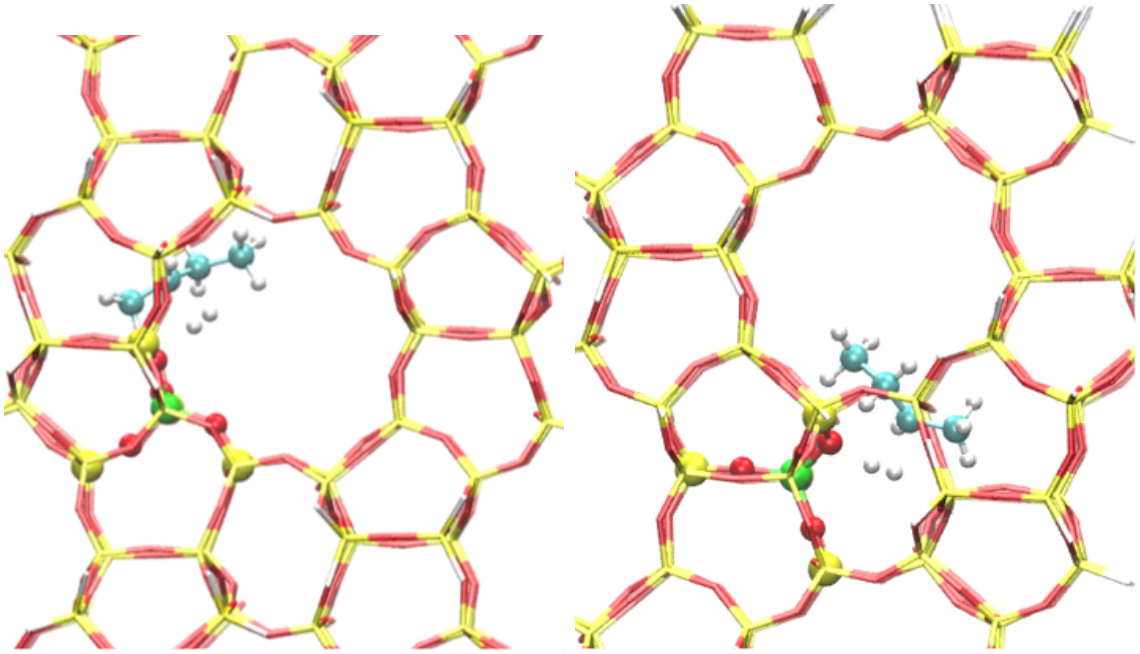

Figure 4.11: Alignment of the methylene dehydrogenation transition state within the zeolite framework at the (a) T12, and (b) T10 acid site.

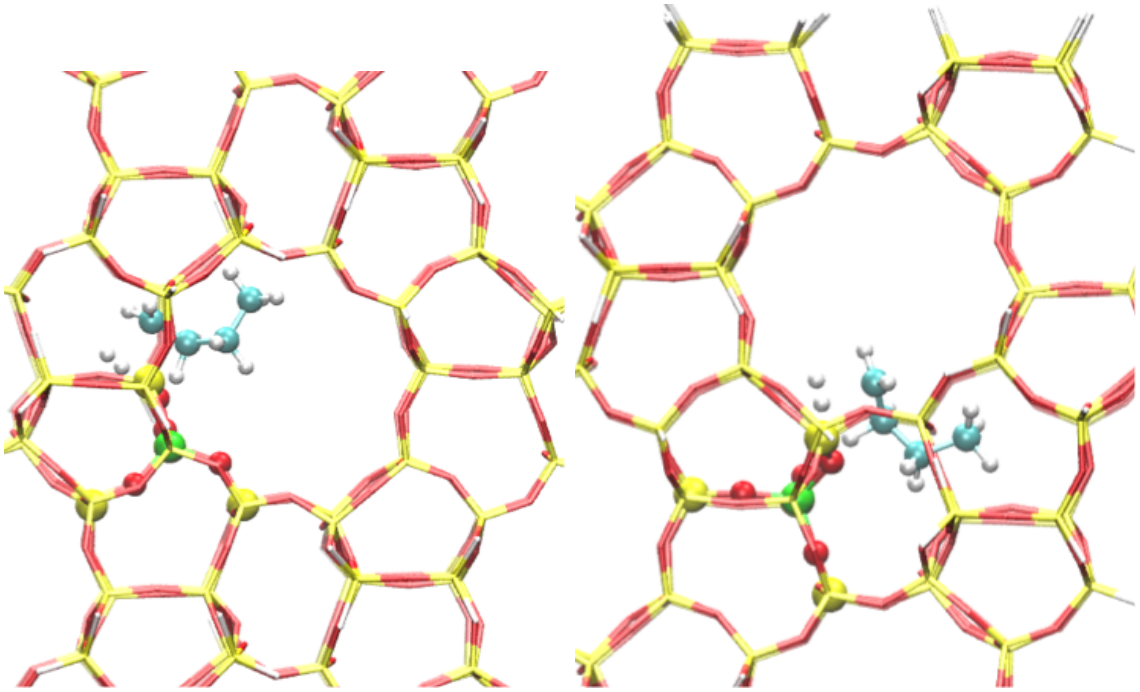

Figure 4.12: Alignment of the methyl dehydrogenation transition state within the zeolite framework at the (a) T12, and (b) T10 acid site.

Acid site	**T12**			**T10**		
Model	QM/MM partial	QM/MM	Difference	QM/MM partial	QM/MM	Difference
Central cracking (TS1)	54.9	42.5	12.4	57.0	47.6	9.4
Central cracking (TS2)	50.1	36.1	14.0	52.6	41.2	11.4
Terminal cracking (TS1)	55.1	45.3	9.8	53.8	46.2	7.6
Terminal cracking (TS2)	55.6	40.2	15.4	57.8	44.3	13.5
Methylene dehydrogenation	63.2	45.4	17.8	66.7	49.7	17.0
Methyl dehydrogenation	72.9	60.2	12.7	76.3	63.5	12.8

Table 4.5: Comparison of intrinsic activation energies (kcal/mol) between T12 and T10 sites. "QM/MM" contains activation energies calculated taking into account all possible interactions occurring in the model. "QM/MM-partial" contains activation energies calculated in the absence of non-bonding framework-substrate interactions. Difference between the two is an indicator of the framework contribution to energy lowering.

barriers with alkane chain length. This supports the claim in experimental literature that the decrease in apparent activation energy with increase in alkane chain length is primarily due to a corresponding increase in the enthalpy of adsorption of the alkane[111]. The differences in activation energies between T12 and T10 sites are also invariant with alkane chain length.

4.4.4 Heats of adsorption

Heats of adsorption were calculated at 773 K for light alkanes ranging from propane to n-hexane and the results are shown in Figure 4.15. They are higher for adsorption near a T10 site located in the sinusoidal channel than near a T12 site located in the intersection between straight and sinusoidal channels. The difference between the two sites is relatively large for propane, but decreases steadily with increase in C number until hexane. At both locations, the hexane molecule is located in the center of the channel and aligned almost parallel to it, resulting in similar interactions with the framework at both sites, unlike smaller alkanes. Figure 4.15 also reports the heats of alkane adsorption determined experimentally. Since the measurements of alkane adsorption are carried out at temperatures below those at which cracking and dehydrogenation occur, it is important to assess the sensitivity of

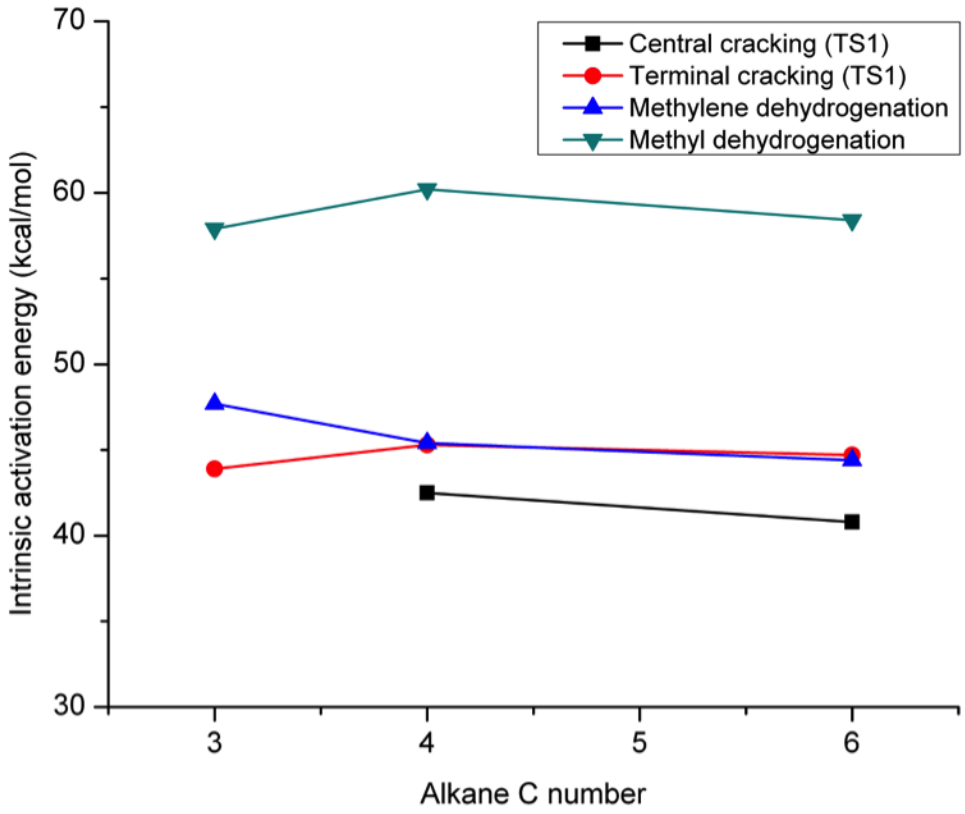

Figure 4.13: Intrinsic activation energies (kcal/mol) for propane, n-butane and n-hexane reactions in H-MFI at the T12 acid site.

ΔH_{ads} to temperature. Heats of alkane adsorption in MFI measured by de Moor et al.[127] for temperatures ranging from 301–400 K show little dependence on temperature. ΔH_{ads} values calculated using QM/MM also vary by less than 2 kcal/mol over the temperature range of 400–773 K. The calculated values, however, are much higher in magnitude than experimentally measured heats of adsorption. The magnitude of over-binding increases with alkane chain length, as indicated by the slopes of the fitted curves. The magnitudes of the slope: 4.7 kcal/mol/CH_2 unit at the T12 site and 3.6 kcal/mol/CH_2 unit at the T10 site are much larger than the experimental value, 2.5 kcal/mol/CH_2 unit. However, at finite temperatures, the alkane is very weakly bound to any particular acid site, as demonstrated using molecular dynamics simulations by Goltl et al[128]. An experimental value of heat of adsorption therefore represents an ensemble average over all possible locations of the adsorbate. Hence, purely quantum calculations at a few representative acid sites may not generate

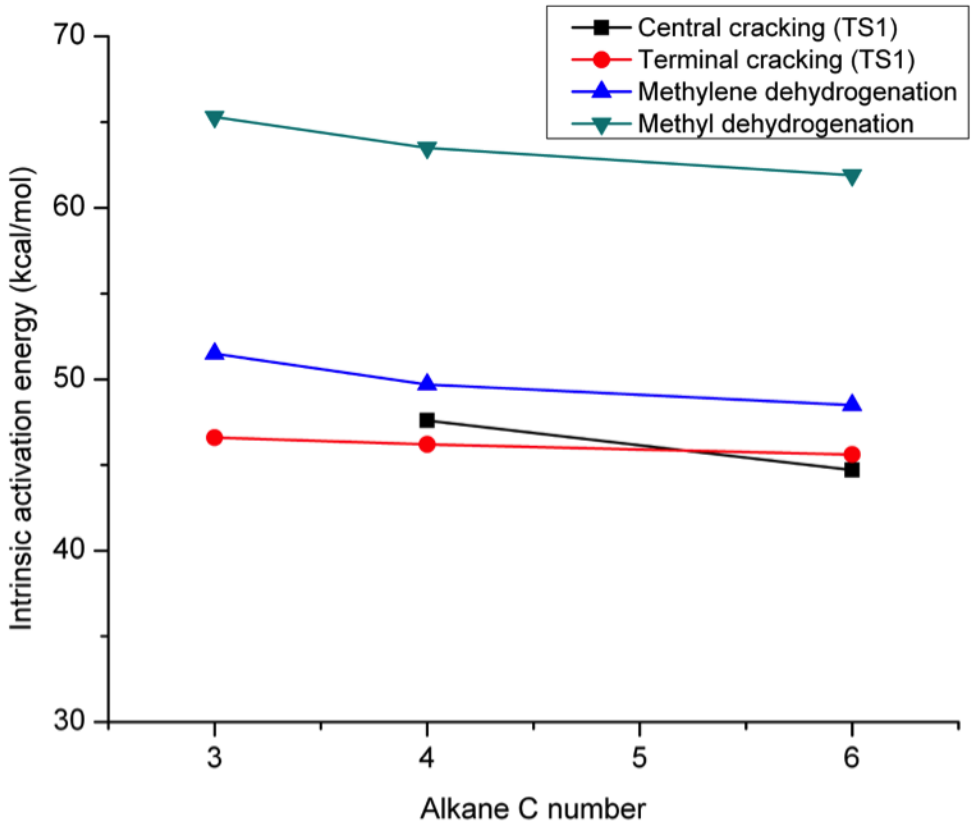

Figure 4.14: Intrinsic activation energies (kcal/mol) for propane, n-butane and n-hexane reactions in H-MFI at the T10 acid site.

an accurate picture of adsorption behavior. Averaged values, such as those calculated using Monte Carlo simulations by Swisher et al.[95], are much closer to experiment, as shown in Figure 4.15.

Although the current analysis is restricted to the study of two sites, and therefore cannot produce an accurate estimate of heat of adsorption, the QM/MM model clearly overbinds the alkane to the zeolite framework. A recent study by Tranca et al.[100] demonstrated that by using a periodic model and the PBE functional with a dispersion correction identical to the one employed in this study, heats of adsorption can be estimated to within 10% of the experimental values. The optimized MM dispersion parameters for the framework, therefore, are largely responsible for the overbinding, which was verified via pure MM energy calculations. The parameters result in higher heats of adsorption since they were optimized

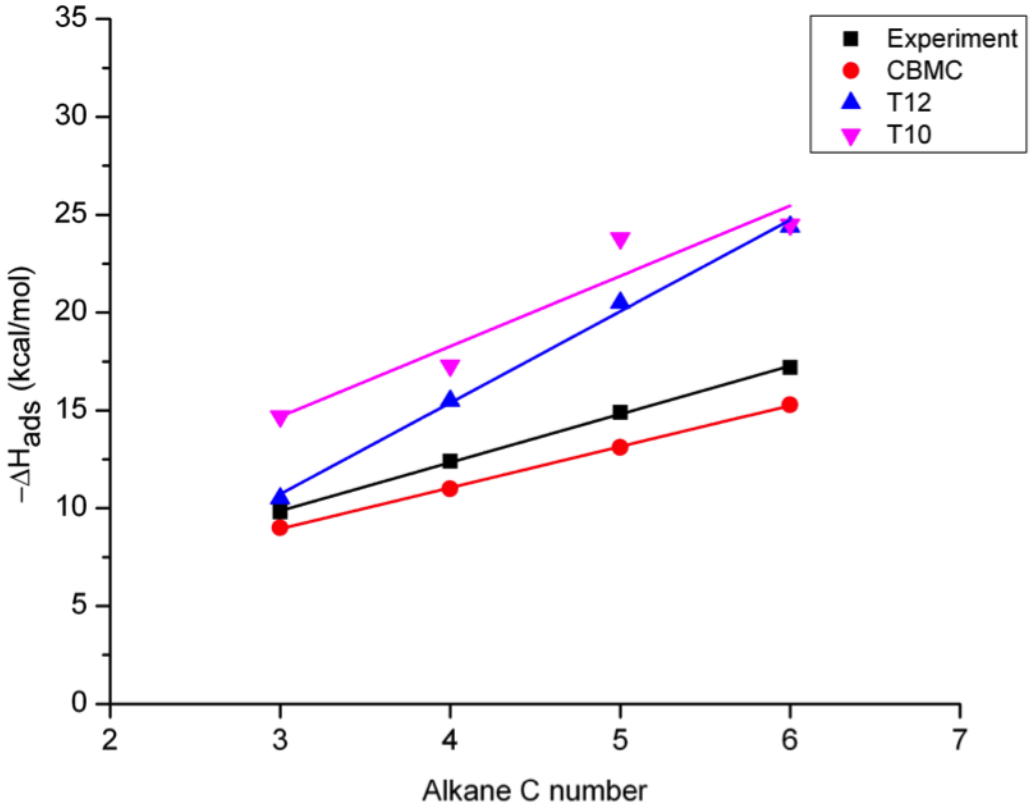

Figure 4.15: Heats of adsorption ($-\Delta H_{ads}$) (kcal/mol) of $C_3 - C_6$ alkanes calculated at the T12 and T10 sites for silicalite at 773K, and comparison with experimental[127] as well as computational[95] literature using configurational bias Monte Carlo (CBMC).

for a small 23 T–atom MFI cluster using a smaller basis set, 6-31+G**. In addition, although the dual basis correction brings the result closer to the complete basis set limit, it only increases the overbinding of the alkane to the zeolite. The dual-basis corrected values are reported in Appendix A. These overbinding errors, however, are cancelled out in intrinsic activation energy calculations since both the transition state and the reactant are in the adsorbed state, and electrostatic interactions dominate over dispersion in cracking and dehydrogenation transition states.

4.4.5 Apparent activation energy

The apparent activation energy is given by the sum of the enthalpy of adsorption and the intrinsic activation energy. Since the calculated enthalpy of butane adsorption is significantly

Reaction	**Calculated**		**Experiment**	
	T12	T10	Narbeshuber et al.[112]	Kranilla et al. [113]
Central cracking (TS1)	30.1	35.2	32.3	32.0
Central cracking (TS2)	23.7	28.8		
Terminal cracking (TS1)	32.9	33.8		33.9
Terminal cracking (TS2)	27.8	31.9		
Methylene dehydrogenation	33.0	37.3	27.5	35.6
Methyl dehydrogenation	47.8	51.1		

Table 4.6: Apparent activation energies (kcal/mol) for reactions of n-butane at both T12 and T10 acid sites compared with experimental data.

higher than the experimental value (see Figure 4.15), we used the experimental value of -12.4 kcal/mol, reported by de Moor et al[127]. The apparent activation energies, thus obtained, are not entirely accurate since they do not include the influence of adsorption specific to the acid site. From adsorption calculations, this difference between the acid sites is known to be about 2.7 kcal/mol. Moreover, since the heat of adsorption at the T10 site is higher than at T12, the differences in apparent activation energies at the two sites is likely to be smaller than differences in intrinsic activation energies.

Apparent activation energies for n-butane cracking and dehydrogenation are compared with experimental values in Table 4.6. There is a general agreement in the experimental literature regarding the activation energies for both terminal and central cracking. Based on a comparison between calculated and experimental activation energies for cracking, it is likely that the T10 site is more favorable to cracking, and the reaction preferentially occurs via both TS1 and TS2 mechanisms at T10. It is also likely that cracking is favorable at both acid sites, but the TS2 mechanism is not, in spite of lower activation barrier compared to TS1. Calculation of the pre-exponential factor is essential for further insight into the preferred mechanism as well as preferred acid site for cracking, but it was beyond the scope of this investigation. In general, the calculated energies for cracking are consistent with experimental results, thereby validating the accuracy of the QM/MM cluster model in determining intrinsic activation energies. Under the assumption that intrinsic activation energies are insensitive to alkane chain length, intrinsic barriers for n-butane cracking were added to experimental heats of adsorption reported for C_3-C_6 alkanes by de Moor et al[127]. The apparent barriers thus obtained are in good agreement with experimental data, as can be seen in Table 4.7, thereby suggesting that cracking via TS1 at both acid sites (or via both TS1 and TS2 at the T10 site) is preferred under experimental conditions.

In contrast to cracking, the experimentally determined activation energies for butane de-

Alkane	**Calculated**				**Experiment**
	T12 (TS1)	T12 (TS2)	T10 (TS1)	T10 (TS2)	
propane	35.5	30.4	36.4	34.5	37.0
n-butane	30.1, 32.9	23.7, 27.8	35.2, 33.8	28.8, 31.9	32.3
n-pentane	27.6, 30.4	21.2, 25.3	32.7, 31.3	26.3, 29.4	28.7
n-hexane	25.3, 28.1	18.9, 23.0	30.4, 29.0	24.0, 27.1	25.1

Table 4.7: Apparent activation energies (kcal/mol) for cracking (central, terminal) of C3-C6 alkanes compared with experimental values reported by Narbeshuber et al[112].

hydrogenation show significant variation. Since the product alkenes from dehydrogenation rapidly isomerize, experiments cannot determine the reaction pathway from the product distribution. Only the work of Narbeshuber et al. (Si/Al = 35)[112] reports activation barriers for dehydrogenation which are lower than those for cracking, a consequence possibly of the presence of Lewis acid sites in the zeolite.[115] Therefore, the activation energies were compared with the value reported at zero conversion values by Kranilla et al. (Si/Al = 35)[113]. This value corresponds well with the calculated values for methylene dehydrogenation at both acid sites. Based on these observations, it can be concluded that dehydrogenation prefers the energetically favorable methylene pathway, with little preference for acid site location. Although the activation energy for the methyl pathway is significantly higher than any experimental value, the difference between the methyl and methylene pathways is in agreement with theoretical calculations on both MFI[97] and chabazite[125].

4.5 Conclusions

Energetics of alkane reactions in zeolites can be captured accurately and at reasonable cost using a hybrid QM/MM method and dispersion-corrected density functional theory. The method was applied to a large cluster model of H-MFI in order to study the cracking and dehydrogenation of n-butane. Two transition states were found for terminal and central cracking of butane one involving proton attack at a C-C bond and the second involving direct attack on a C atom. The activation barriers for both terminal and central cracking of C-C bonds depend on the mode of proton attack. A single transition state was observed in the case of both methyl and methylene dehydrogenation. The structure of these transition states indicates that dehydrogenation occurs towards the product side of the reaction trajectory via a concerted mechanism involving simultaneous protonation and alkene formation. The non-equivalence of different acid sites in H-MFI was demonstrated through a comparison of intrinsic activation energies as well as heats of adsorption at two distinct sites one located at the channel intersection, and the other within the sinusoidal channel. Heats of adsorption, calculated for C_3 to C_6 linear alkanes, are higher than those measured experimentally, with a large fraction of the error occurring due to the MM dispersion parameters employed for

the framework Si and O atoms. Calculations of the apparent activation energies for butane cracking and dehydrogenation and for the terminal cracking of C_3-C_6 linear alkanes were compared with experimentally determined values. These calculations used experimental values for the heat of alkane adsorption. The apparent activation energies calculated in this manner for butane agree very well with those determined from experiments, from which is concluded that the intrinsic activation energies determined using the QM/MM method are accurate. The calculated activation energies for cracking of C_3-C_6 alkanes also compare well with values reported from experiments, and confirm that the decrease in the magnitude of the barrier with increasing carbon number is due to the increase in the heat of adsorption with carbon number.

4.6 Acknowledgements

Dr. Paul Zimmerman was a collaborator on this project. This work was supported by a grant from Chevron Energy Technology Co.

Chapter 5

Computational Examination of the Influence of Pore Geometry on Monomolecular Reactions of n-Butane in Brønsted Acid Zeolites

5.1 Abstract

The computational approach described in Chapter 4 is extended to examine sensitivity of intrinsic kinetics of monomolecular reactions of n-butane to zeolite pore topology. Monomolecular cracking and dehydrogenation reactions of n-butane are examined in six zeolite frameworks - TON, SVR, MFI, MEL, STF and MWW, with active sites located within channels, channel intersections and cage geometries. A hybrid quantum mechanics/molecular mechanics (QM/MM) approach is employed to treat cluster models of these frameworks, along with dispersion-corrected density functional theory (DFT), and a quasi-rigid rotor harmonic oscillator (quasi-RRHO) for thermochemical corrections. Calculated intrinsic enthalpies and entropies of activation are then compared with experiments in order to examine the accuracy of this approach, gain insights into preferred active site locations, and examine the influence of pore geometry on reaction pathways and rate parameters. In general, enthalpies of activation are estimated accurately with this procedure. Entropies of activation are in good agreement with experiments only for active sites located in narrow channels, since the thermodynamic approximation is unable to capture anharmonic contributions arising from adsorbates within less confined pore spaces or loose transition states (TSs). Cracking enthalpies are relatively uniform across pore geometries. However, since the reactant is far less confined relative to the TS in larger pores, entropies of activation for central cracking in intersections and cages are markedly lower than in channels. We also find what may be the first evidence of pathway selectivity with varying pore geometry for alkane dehydrogenation. Based on a comparison between experiment and calculated intrin-

sic enthalpies, the methylene route for dehydrogenation is preferred in most channels and channel intersections. Within active sites in cages, however, methyl dehydrogenation seems to occur almost exclusively, which can be attributed to entropy compensation occurring in larger, less confined pore geometries.

5.2 Introduction

Zeolites find extensive applications in industry as solid acid catalysts for petrochemicals and refining owing to their high acid strength and thermal stability[8, 9]. Rational design of zeolite catalysts requires knowledge of the number and distribution of active sites, the differences in acid strengths of each Brønsted proton, as well as the role played by the extended framework in adsorption and reaction kinetics.

Although it is difficult to experimentally determine the exact location of protons in most frameworks, there is sufficient evidence to prove that the siting is non-random, and dependent on the synthesis route[10]. Recent reviews [129, 130] discuss various experimental and computational attempts to quantify acidity and understand the relationship between acidity and catalytic activity. They conclude that description of activity is far more complex, and that reaction rates are governed not only by acidity, but also confinement effects resulting from varying pore sizes and geometries. Therefore, researchers employ probe reactions to directly examine the role of acidity and framework effects on adsorption and reaction kinetics. Monomolecular cracking and dehydrogenation reactions of small alkanes such as propane and butane are useful probe reactions owing to their prevalence at high temperatures and low pressures [111], and the relatively simple product distributions.

Owing to its complexity, the effect of pore topology on adsorption and intrinsic reaction kinetics has been debated extensively in the literature. Experimental studies of alkane cracking demonstrated the invariance of activation enthalpies across various zeolite frameworks, and concluded that either confinement tends to affect only adsorption equilibria[11], or that similar intrinsic rates result from a cancellation of Brønsted acidity and interactions between the transition state (TS) and extended framework[131]. More recent studies showed that adsorption alone may be insufficient to explain reaction rate differences[12], and that entropy changes govern trends in intrinsic rates of cracking with respect to framework topology and alkane chain length.

By varying active site distributions in MOR, Gounder and Iglesia[114] showed that cracking and dehydrogenation reactions of propane preferably occur in the 8-MR side pockets relative to the larger 12-MR main channels. Since enthalpies were invariant with active site distribution, they attributed this preference to partial confinement in the side pockets that leads to higher entropies of activation. A recent molecular dynamics study by Bučko and Hafner[132] demonstrated that this difference is a consequence of alkane confinement and

not of the TS. The intrinsic entropies of activation are lower in the 12-MR channels relative to the side pockets because the reactant state is far less confined, and the alkane loses translational and rotational freedom upon activation. Since the reactant is already highly confined in the 8-MR side pockets, the entropy loss on activation is also lower.

The critical role played by entropy has also been examined for other zeolite frameworks. Janda and Bell [133] demonstrated that variations in the locations of Brønsted acid sites caused by changes in Al concentration affect the kinetics of n-butane cracking and dehydrogenation in MFI. Higher Al content results in increased selectivity towards terminal cracking and dehydrogenation relative to central cracking. These changes were attributed to preferential Al siting in the channel intersection, where lower confinement results in higher entropies of activation for reactions that occur via loose TSs such as dehydrogenation.

Intrinsic enthalpies of activation were also found to be sensitive to active site location in MFI. In an earlier computational study, we calculated enthalpies of adsorption and activation for monomolecular cracking and dehydrogenation of n-butane at two distinct active sites[134]. Reaction energetics are highly sensitive to whether the active site is located at the channel intersection or sinusoidal channel owing to differences in acid site strength and electrostatic stabilization of the TS by the extended framework. However, this is an incomplete picture of reaction kinetics since limited active sites were examined, and an analysis of entropies of activation was not carried out.

The goal of this work, therefore, is to investigate how pore shapes and sizes affect reaction pathways and kinetics. We extend the previous QM/MM approach to calculate both intrinsic enthalpies as well as entropies of activation for monomolecular reactions of n-butane in six zeolite frameworks with the active sites located in pore geometries varying from narrow channels to large supercages. Distinct trends emerge for cracking and dehydrogenation when calculated activation parameters are analyzed along with experiment. In particular, dehydrogenation exhibits a preference for the energetically unfavorable methyl pathway in cage structures, which we propose is a consequence of a strong entropy compensation effect.

5.3 Methods

5.3.1 Computational procedure

The computational approach adopted in this study is largely similar to previous work on reaction kinetics in the MFI framework [134, 135]. All calculations were performed using hybrid quantum mechanics/molecular mechanics (QM/MM)[104, 136]. For each framework, a large cluster containing the active site of interest was chosen, and terminated with H atoms. The smaller five tetrahedral atom (T5) cluster containing the active site, along with the

substrate, was treated quantum mechanically, and MM was used to represent the rest of the framework. The cluster model and active site for each zeolite framework is described in the following section. TS guesses were calculated using the freezing string method (FSM)[42, 79] and optimized using the partitioned-rational function optimization (P-RFO) technique[6]. TSs for cracking correspond to the TS1 geometry described in our previous work[134] since TS2 significantly underestimates activation enthalpies, and therefore may not correspond to the true rate-limiting step for cracking. Apart from minor differences in bond distances, the TSs and therefore the mechanism for each cracking or dehydrogenation pathway remained largely invariant with active site location.

All calculations were performed using a developmental version of Q-Chem 3.2[65]. Geometry optimizations as well as vibrational analyses were carried out using ωB97X-D/6-311G** level of theory[117, 118] to describe the QM region. The vibrational spectrum of an adsorbed molecule in a zeolite typically consists of several low-lying frequencies that correspond to restricted translational and rotational movement of the adsorbate. By erroneously treating these modes as vibrations under the rigid rotor-harmonic oscillator approximation (RRHO), the loss in entropy associated with adsorption is typically overestimated[16, 127]. In order offset some of these errors in the estimation of thermochemical corrections from vibrational frequencies, a quasi-RRHO approach[17, 136], was employed instead. By interpolating between a one-dimensional free rotor at low frequencies to a harmonic oscillator at high frequencies, this method attempts to capture the thermochemical contributions from low-lying modes more accurately. In a previous study, we were able to estimate intrinsic activation enthalpies and entropies for central and terminal cracking of n-butane in MFI using this technique[135] within experimental accuracy. Therefore, we applied this approach to calculate intrinsic enthalpies (ΔH_{int}) and entropies (ΔS_{int}) of activation for cracking and dehydrogenation of n-butane across active sites in six zeolite frameworks at 773K. The influence of pore topology on activation parameters was examined using these results, taken along with intrinsic parameters determined from combined experimental and Configurational Bias Monte Carlo (CBMC) studies, described in a later section.

5.3.2 Zeolite cluster models

In order to examine the influence of the extended framework on intrinsic kinetics, six zeolite frameworks were chosen, and classified into three categories based on location of the active site in the QM/MM cluster model. Both the framework topologies (left)[137] as well as active site locations (right) are described in Figures 5.1 - 5.6. In the pore topology representations, channels/cages are labeled by color based on their sizes - yellow corresponds to medium channels (4–6Å), orange to large channels (>6Å), cyan to medium pores or intersections (6–8Å), and purple to large cages (>8Å). The largest cavity diameter for the framework is also given in each figure caption in parentheses[137]. The sizes of the cluster models, given by the number of T-atoms, are listed in Table 5.1.

Type	Framework	T-atoms
1	TON	280
	SVR	348
2	MFI	437
	MEL	264
3	STF	398
	MWW	292

Table 5.1: Number of T-atoms in each zeolite cluster model. Sizes were chosen based on QM/MM benchmark studies[119]. Subtracting 5 from the total T-atoms yields the size of the MM region.

The first category, labeled Type 1, consists of active sites located within straight or sinusoidal channels. Two frameworks with similar cavity diameters but different channel geometries, TON and SVR, were chosen. In TON, which consists of one-dimensional 10-MR straight channels and 4 distinct tetrahedral (T) sites, the Al atom was located at the T2 site, based on siting probabilities estimated in a combined NMR and QM/MM study[138]. Both the framework topology as well as the active site location is described in Figure 5.1. The SVR framework is three-dimensional, consisting of 10-MR sinusoidal channels and smaller side pockets[139]. The structured vacancies terminated by oxygen were replaced with silanol groups[140], and the Al atom was located such that the acidic proton is located in the sinusoidal channel, as shown in Figure 5.2.

The second category, labeled Type 2, consists of active sites located at channel intersections of MFI and MEL frameworks. MFI is a three-dimensional framework consisting of 12 distinct T-sites, of which T12 was chosen so that the acidic proton is located at the intersection of 10-MR straight and sinusoidal channels, as shown in Figure 5.3. Both MFI and MEL consist of intersecting channels of similar diameters. The key features that distinguish MEL are the presence of only straight channels[141], and a larger cavity. The Al atom was chosen such that the acidic proton is situated at the intersection of straight channels, as shown in Figure 5.4.

The third category, labeled Type 3, consists of active sites located in cages larger than 8Å within the MWW and STF frameworks. STF consists of one-dimensional 10-MR portals connecting large 18-MR pores[142]. The acidic proton was located within the larger pore, as shown in Figure 5.5. MWW consists of two independent pore networks, one consisting of 10-MR sinusoidal channels, and the other consisting of 12-MR supercages accessible via 10-MR openings[143]. Out of 8 possible distinct T sites, the active site was located within the supercage at the T4 site, as shown in Figure 5.6. The active site was chosen based on the results of computational studies that determined the most energetically stable T-sites

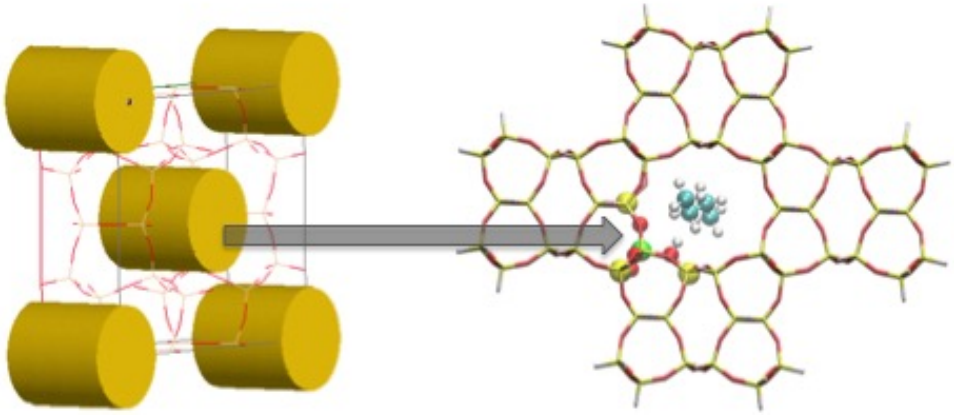

Figure 5.1: Type 1 - TON with acidic proton in straight channel (5.7Å). The QM region in the cluster model (right) is depicted using ball-and-stick representation. In all cluster representations, yellow corresponds to Si atoms, red to O, green to Al, white to H, and cyan to C atoms.

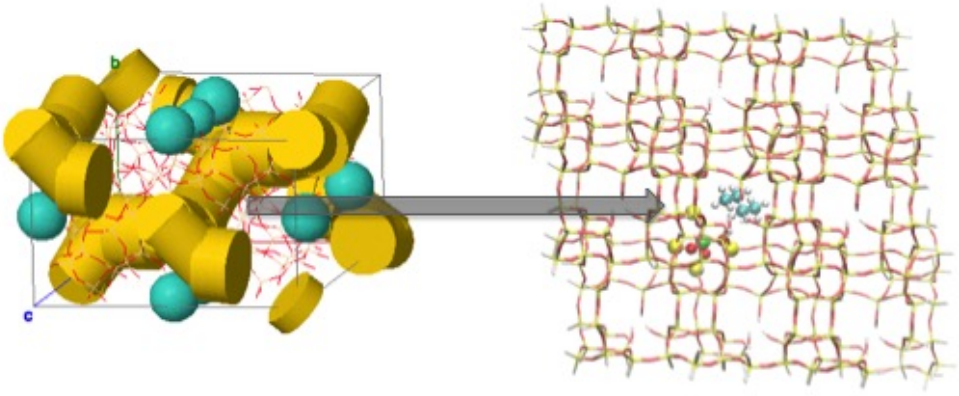

Figure 5.2: Type 1 - SVR with acidic proton in sinusoidal channel (5.7Å)

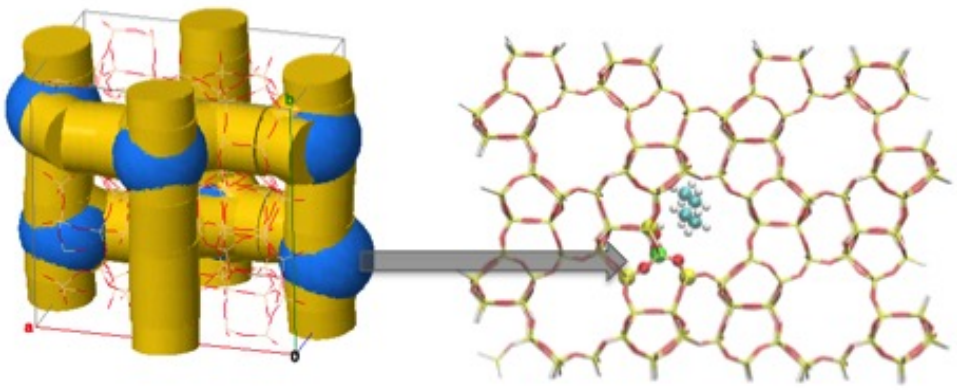

Figure 5.3: Type 2 - MFI with acidic proton in intersection of straight and sinusoidal channels (7.0Å)

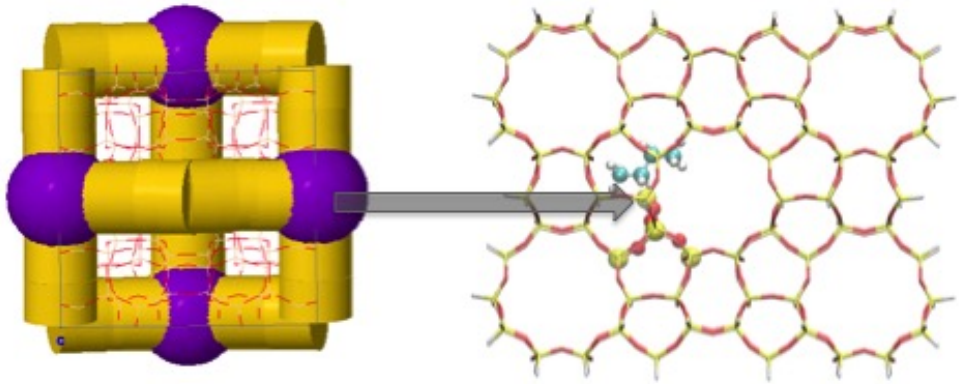

Figure 5.4: Type 2 - MEL with acidic proton in intersection of two straight channels (8.4Å)

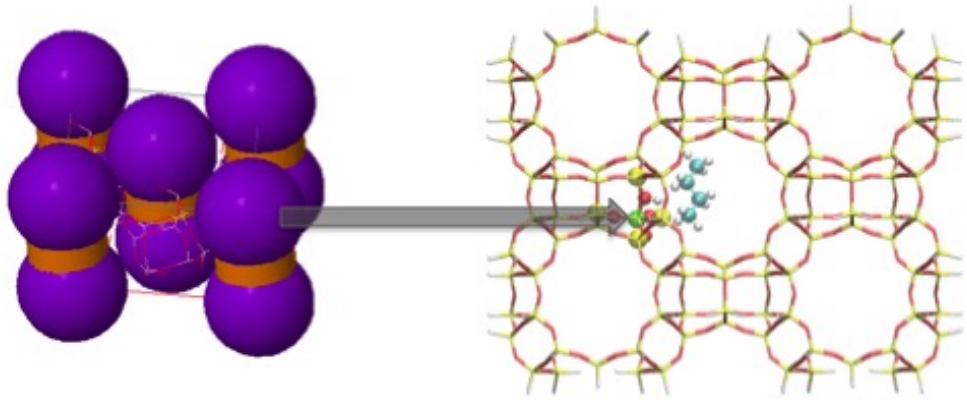

Figure 5.5: Type 3 - STF with acidic proton in the cage (8.3Å)

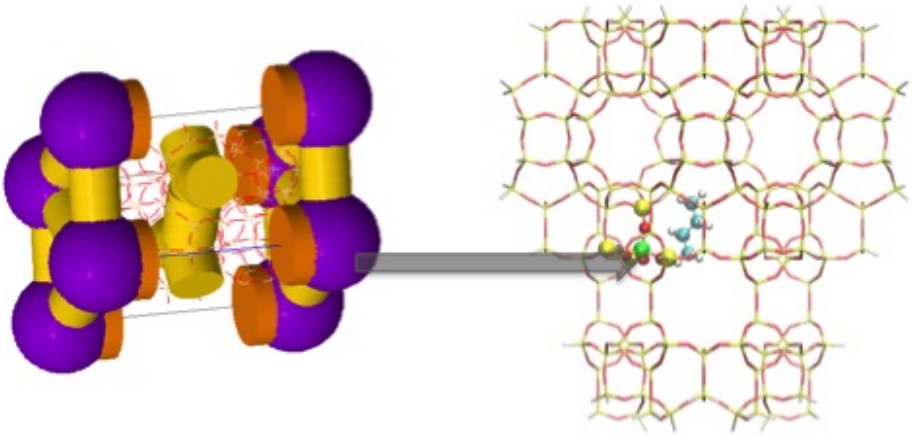

Figure 5.6: Type 3 - MWW with acidic proton in the supercage (10.3Å)

for Al substitution[144, 145].

Theoretical studies on alkane adsorption justify the choice of active site placement within the largest pore openings in Type 2 and 3 zeolite frameworks. Ab initio molecular dynamics[132] and CBMC[146] adsorption studies have demonstrated that, although adsorption is favored in narrow pores at lower temperatures owing to energetically favorable dispersion interactions between the framework and adsorbate, large pores are entropically favorable, and are therefore preferred sites for adsorption at reaction temperatures.

Framework	Si/Al ratio
TON	49
SVR	71, 84
MFI	44, 142
MEL	29
STF	18
MWW	14, 16, 18

Table 5.2: Si/Al ratios of zeolite samples employed in experiments[146]. In cases where multiple samples were used for the same framework, the average parameters were calculated for comparison with computations.

5.3.3 Experiments: Intrinsic activation parameters

Previous studies on alkane adsorption concluded that adsorption enthalpies and entropies are relatively insensitive to temperature changes, based on observed invariance of these parameters between 300 and 400K [127]. However, a recent investigation using CBMC simulations for MFI by Janda et al.[135] demonstrated that the distribution of adsorbate across T-sites, and adsorption parameters as a consequence, vary significantly with temperature. At cracking temperatures, the authors reported a preference for adsorption at the channel intersection since the entropy loss is lower relative to that for adsorption at active sites located within channels. By calculating a Boltzmann average over adsorption parameters across all T-sites at 773K, and adding those to experimentally determined apparent activation enthalpies and entropies, they were able to rigorously calculate intrinsic activation enthalpies and entropies for a range of zeolite frameworks[146]. The adsorbed alkane configurations at all active sites calculated using QM/MM satisfy the cut-off radius criterion specified by Janda et al[135]. Therefore, a direct comparison is possible between calculated and experimentally derived[146] intrinsic activation parameters. The Si/Al ratios for the zeolite samples used in experiments are shown in Table 5.2. In cases where multiple experimental values were available for the same framework, the averaged intrinsic parameters were compared with calculated results.

The reported error bars in experiments correspond to measurement errors associated with apparent activation parameters only. Errors in estimation of adsorption parameters arise from the choice of cut-off radius, and were estimated to be about 2 kJ/mol for the enthalpy, and 10 J/mol-K for the entropy of adsorption at an active site.

5.4 Results and discussion

5.4.1 Central cracking

Figure 5.7 shows experimental as well as calculated intrinsic enthalpies of activation (ΔH_{int}) for central cracking of n-butane at 773 K in all frameworks. In Figure 5.7 and all subsequent figures, the frameworks are arranged in order of types 1 through 3 from left to right. Although the comparison between experiment and theory is based on assumptions regarding the preferred location of the active site, calculated results are generally in good agreement with experiments. The small deviation observed in SVR is probably a consequence of the choice of MM charge parameters for the silanol hydroxyl groups in the vacancy sites. Rather than re-optimizing the parameters to reproduce energies calculated using pure QM on large clusters[104], we utilized the same parameters as those for the other frameworks, and adjusted the charges on the silanol groups to maintain charge neutrality of the entire cluster.

There is no discernible influence of the pore topology on experimental or calculated intrinsic enthalpies. The results are consistent with earlier cracking studies with MFI, BEA, MOR, and FAU[11], which concluded that intrinsic kinetics are similar across frameworks, and the differences in framework shape and size are reflected in adsorption parameters. Maihom et al.[102] arrived at similar conclusions based on a computational study of cracking using large cluster models of MFI and FAU. These observations are also consistent with the early character of the central cracking TS[134], in which the substrate is tightly bound to the active site, and is therefore less influenced by the size and geometry of the extended framework.

However, ΔH_{int} alone is insufficient to examine the variation of intrinsic kinetics with pore topology. Unlike enthalpies of activation, entropies are highly sensitive to the location of the active site. Experimental and calculated intrinsic entropies of activation (ΔS_{int}) for central cracking are shown in Figure 5.8. Entropy changes calculated using the quasi-RRHO approach are in good agreement with experiments for Type 1 active sites. Experimental entropies of activation in Type 2 and Type 3 frameworks are typically lower than in Type 1. Bučko and Hafner[132] observed that in the larger main channels in MOR, the adsorbed alkane has greater freedom to rotate and translate relative to the narrow side pockets. Entropy loss associated with the transformation from adsorbate to bound TS, therefore, is higher in the main channels than in the side pockets. A similar situation is conceivable for adsorbates in Type 2 and 3 active sites, where the entropy loss from a relatively free adsorbate to highly bound central cracking TS is higher than in Type 1 sites. The quasi-RRHO approach is unable to completely capture the entropy contributions from the free adsorbate modes, and therefore overestimates the entropy of activation in Type 2 and Type 3 active sites. Better agreement with experiment is achieved in the narrow Type 1 active sites since both the reactant and the TS are less free to translate or rotate, and entropy contributions from these modes are either small or similar in magnitude.

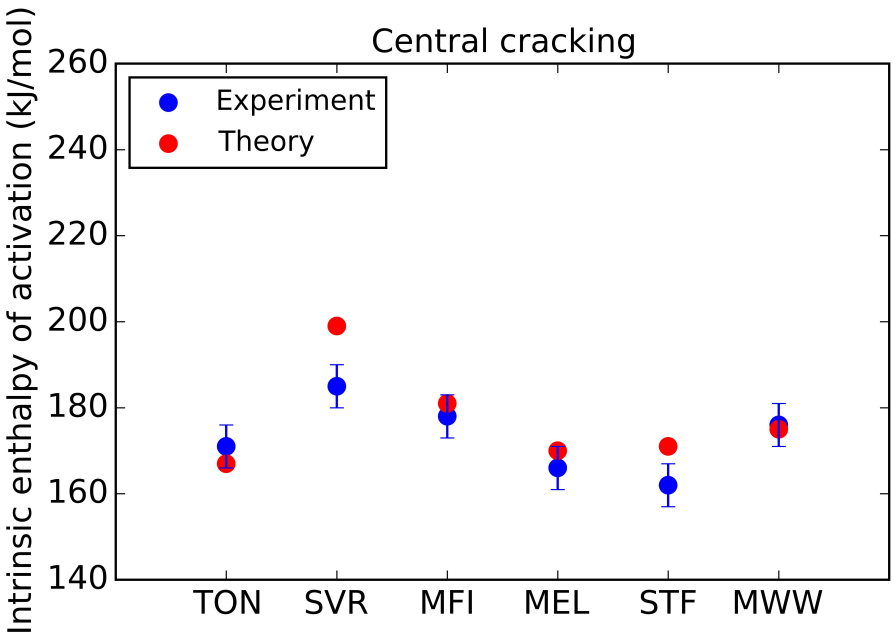

Figure 5.7: Intrinsic enthalpies of activation (ΔH_{int}) in kJ/mol for central cracking of n-butane from experiment and theory.

The exception to low entropies of activation for active sites in larger intersections and cages is MWW, for which ΔS_{int} is comparable to active sites in channels. It is possible that experimental results correspond to active sites in the sinusoidal channel in MWW, or the average over active sites in both channels and supercages. This can be verified via calculations for an active site located in the sinusoidal channel. The calculated value of ΔH_{int} for central cracking over an active site in the sinusoidal channel (T3) is 183 kJ/mol, which is comparable to the value of ΔH_{int} calculated for a site in both a supercage (175 kJ/mol) as well as the averaged experimental value of 176 kJ/mol. Entropies of activation in the sinusoidal channel also corroborate this hypothesis; the calculated value of ΔS_{int} is -13 J/mol-K, which is in good agreement with the experimental average of -20 J/mol-K.

5.4.2 Terminal cracking

Intrinsic enthalpies and entropies of activation for terminal cracking are shown in Figures 5.9 and 5.10, respectively. Higher enthalpies for terminal cracking relative to central have also been observed in previous experimental studies[133, 147] and are a consequence of lower proton affinity of the terminal C-C bond[148]. Calculated values of ΔH_{int} are in good agreement with experimentally observed values with the exception of Type 3 active sites. In STF, calculation for an active site along the 10-MR portal yields a value for ΔH_{int}

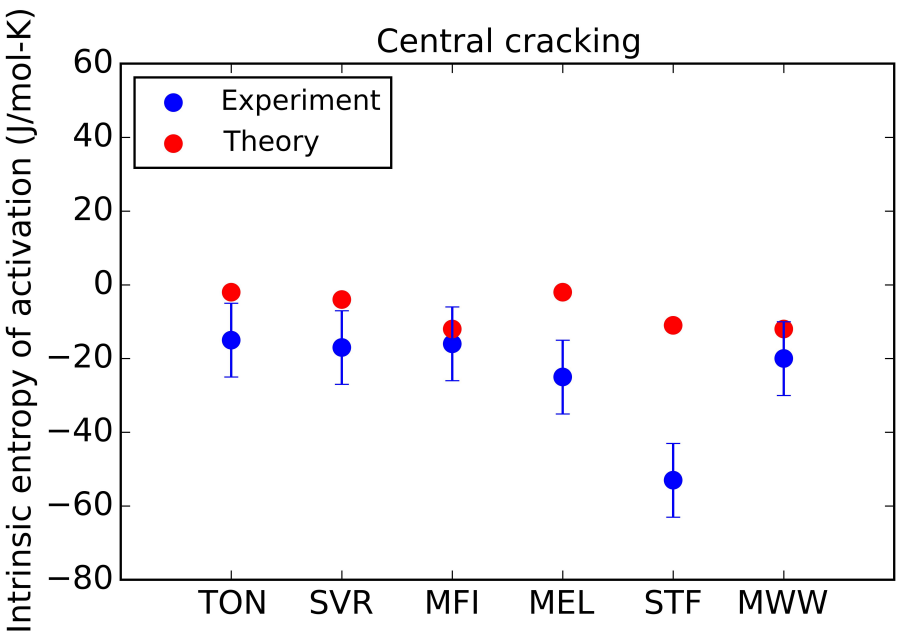

Figure 5.8: Intrinsic entropies of activation (ΔS_{int}) in J/mol-K for central cracking of n-butane from experiment and theory.

of 200 kJ/mol, which is lower than that for the supercage, 229 kJ/mol. The experimental value of ΔH_{int} lies in between the two calculated values (215 kJ/mol), indicating that terminal cracking may occur at both active sites. In MWW, experimental enthalpies range from 196 to 225 kJ/mol, whereas calculated values in the supercage and sinusoidal channel correspond to 184 and 173 kJ/mol respectively. The lower limit of experimental data is in agreement with calculated enthalpy for the supercage, consistent with preferential adsorption in less confined spaces at high temperatures. However, based on the experimental and calculated results, it is clear that more active sites, and not just T3 and T4, need to be examined in order to obtain an accurate picture of intrinsic kinetics in the MWW framework.

In general, the experimental values of ΔS_{int} for terminal cracking are higher than those for central cracking due to the presence of a dangling ethyl group in the TS that possesses rotational degrees of freedom[147]. In less confined pore geometries, the entropy gain of the TS compensates for the loss from a relatively mobile adsorbate. Since larger pores provide more rotational freedom, ΔS_{int} is highest at active sites located in the larger intersection and cages. In contrast to the case for central cracking, calculated values of ΔS_{int} are in good agreement with experiments, although slightly underestimated for MEL and Type 3 sites. However, the accurate estimation of ΔS_{int} for terminal cracking across active sites is most likely the result of fortunate cancellation of errors, because the quasi-RRHO approximation tends to underestimate both adsorbate as well as TS entropies.

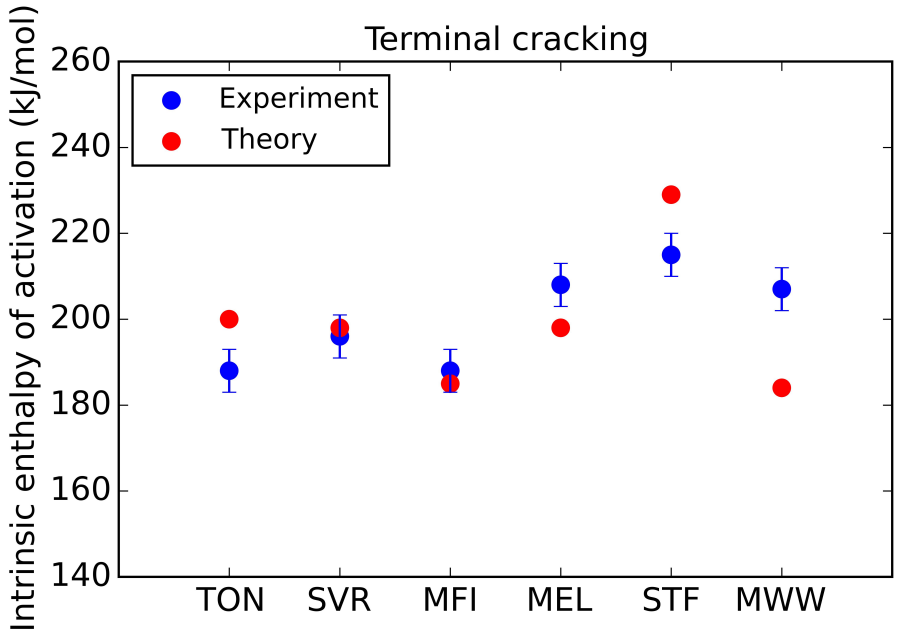

Figure 5.9: Intrinsic enthalpies of activation (ΔH_{int}) in kJ/mol for terminal cracking of n-butane from experiment and theory.

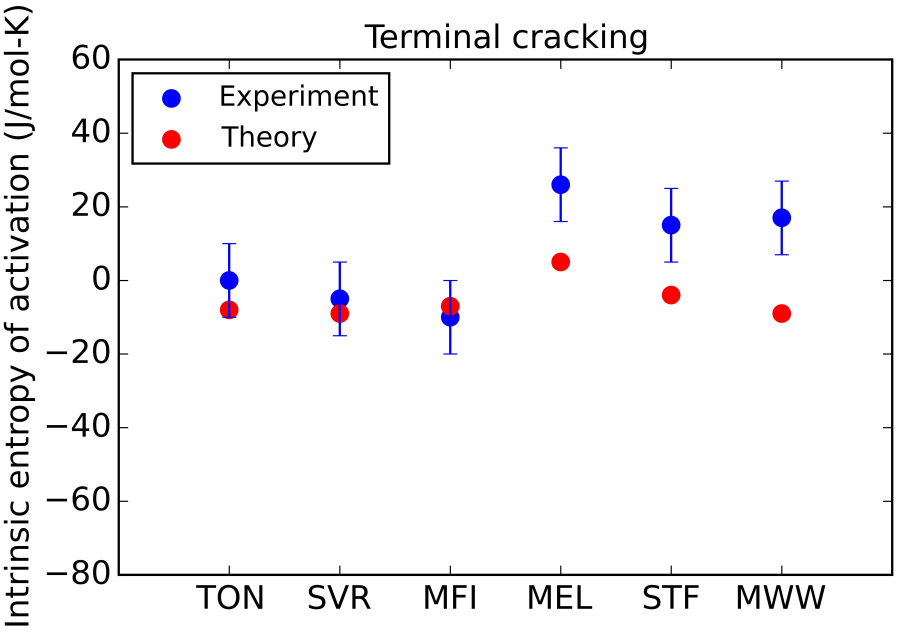

Figure 5.10: Intrinsic entropies of activation (ΔS_{int}) in J/mol-K for terminal cracking of n-butane from experiment and theory.

5.4.3 Dehydrogenation

Since butene isomers, the products of monomolecular dehydrogenation of n-butane, rapidly equilibrate at reaction temperatures, experiments cannot distinguish reaction pathways based on product distributions. Therefore, computed intrinsic activation parameters for both pathways must be contrasted with experiment to gain mechanistic insights. Figures 5.11 and 5.12 compare experimentally observed and calculated values of ΔH_{int} for the methylene and methyl pathway, respectively.

For active sites in narrow channels of TON and SVR, experimental values of ΔH_{int} are in close agreement with those determined for the methylene pathway. Since ΔH_{int} for methyl C-H activation is significantly higher than methylene C-H at all active sites, the preference for the energetically favorable methylene pathway is not surprising. The methylene pathway is also preferred in MEL, but not in MFI. It is possible that experimental data for MFI is based on an active site distribution with fewer sites at the channel intersection. Therefore, calculations were also carried out for an active site located within the sinusoidal channel of MFI, corresponding to Al siting at the T10 position[134]. ΔH_{int} for methylene dehydrogenation at the sinusoidal channel is 221 kJ/mol. The result is in agreement with the experimental value of 232 kJ/mol reported for a Si/Al ratio of 142. ΔH_{int} for the sample with higher Al content (Si/Al = 44) is 250 kJ/mol, equal to the calculated value of 250

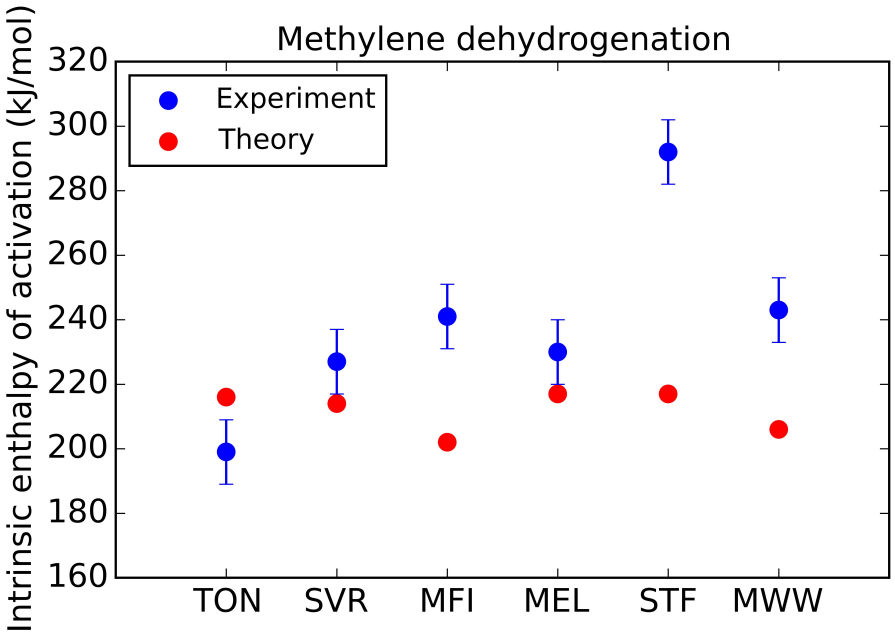

Figure 5.11: Intrinsic enthalpies of activation (ΔH_{int}) in kJ/mol for dehydrogenation (experiment) and methylene dehydrogenation (theory) of n-butane.

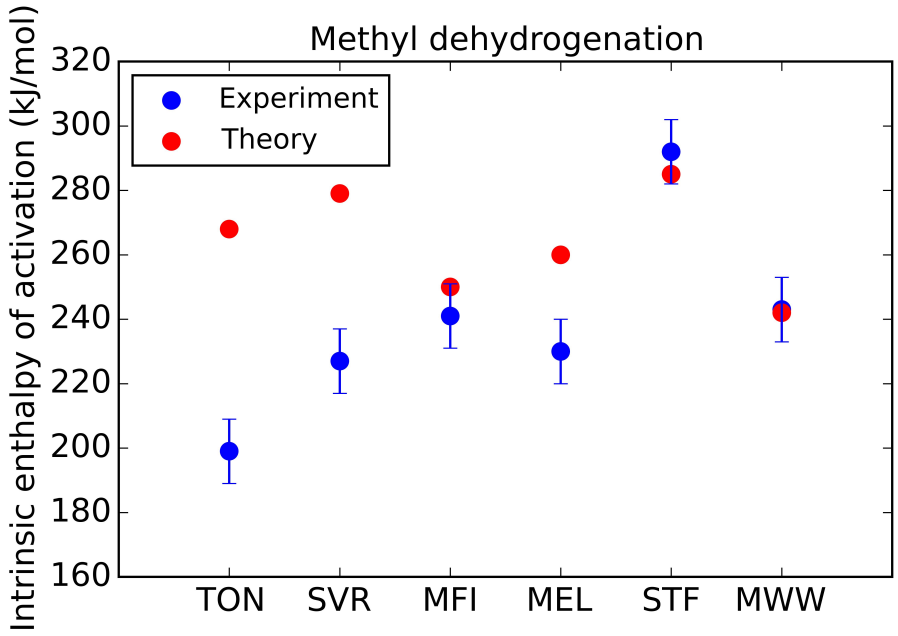

Figure 5.12: Intrinsic enthalpies of activation (ΔH_{int}) in kJ/mol for dehydrogenation (experiment) and methyl dehydrogenation (theory) of n-butane.

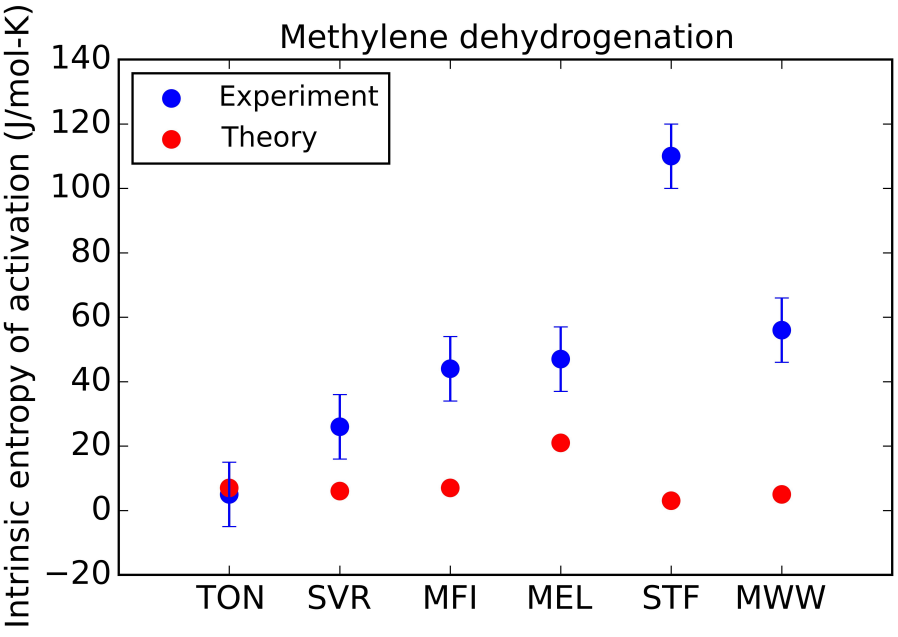

Figure 5.13: Intrinsic entropies of activation (ΔS_{int}) in J/mol-K for dehydrogenation (experiment) and methylene dehydrogenation (theory) of n-butane.

kJ/mol for the methyl pathway occurring at the channel intersection. This agreement between experiment and an intersection site is consistent with a recent study that concluded that increasing Al content in MFI resulted in a larger fraction of protons at the channel intersection[133]. However, in order to explain the preference for the energetically unfavorable methyl pathway, an investigation of activation entropies is necessary. Unlike the case for MFI, ΔH_{int} for methylene dehydrogenation at an active site located in the straight channel of MEL is very close to that for a site located at the intersection.

The results for dehydrogenation on Type 3 active sites are most intriguing. Enthalpies of activation for the methyl pathway are in excellent agreement with experiments, even though the values of ΔH_{int} are about 36 kJ/mol and 68 kJ/mol higher than the methylene barrier for the cage sites of MWW and STF, respectively. In an experimental study of propane dehydrogenation in MOR, FAU, MFI, and BEA, Xu et al.[149] reported similar enthalpies of adsorption across these frameworks, and a wide range in apparent activation energies (123-178 kJ/mol) but did not observe any trend with respect to pore size. Although they attribute these differences to varying stability of the alkoxide intermediate, the results can also be explained by preference for methylene or methyl dehydrogenation pathway depending on the active site distribution in each framework. The preference for the methyl pathway in cages may be a consequence of entropy compensation, and ΔS_{int} is high enough to surmount the enthalpy barrier only in large cage-like geometries, where the TS is far less confined

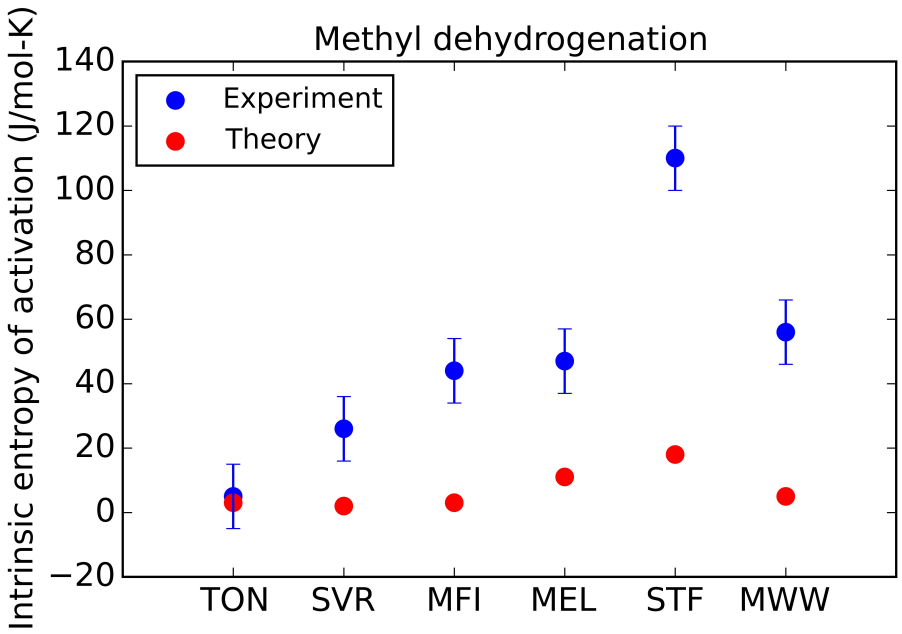

Figure 5.14: Intrinsic entropies of activation (ΔS_{int}) in J/mol-K for dehydrogenation (experiment) and methyl dehydrogenation (theory) of n-butane.

relative to narrow channels. Just as the terminal cracking TS is higher in entropy relative to central cracking, the methyl pathway may be more entropically favorable than the methylene pathway.

To test this hypothesis, values of ΔS_{int} were calculated for the methyl and methylene pathways. Figures 5.13 and 5.14 compare these values with those observed experimentally. Experimental and calculated values of ΔS_{int} for dehydrogenation are higher than those for cracking and are positive, consistent with the late and loose nature of the dehydrogenation TS, in which the H_2 molecule is nearly fully formed[125, 134]. Previous experimental studies on multiple frameworks have also reported higher activation entropies of dehydrogenation relative to cracking[114, 150].

Unfortunately, the computational approach used in this study not only underestimates activation entropies for dehydrogenation, but in addition, unlike the case for cracking, is unable to capture entropy differences between the two dehydrogenation pathways. Dehydrogenation is characterized by a loose TS much like terminal cracking. However, the favorable cancellation of errors that occurred during entropy estimation for terminal cracking is insufficient in the case of dehydrogenation. A closer examination of the vibrational spectrum of the dehydrogenation TS reveals the presence of certain frequencies, typically much higher than the cut-off frequency specified by quasi-RRHO ($100 cm^{-1}$), which correspond to relative translation and rotation of the nascent H_2 molecule, strongly coupled with vibrations. Simple thermodynamic calculations can be carried out to show that a lone H_2 molecule in the channel intersection of MFI can contribute up to 61 J/mol-K in 2-D translational entropy. Therefore, by treating the relative translational and rotational modes of H_2 in the TS as harmonic or quasi-harmonic vibrational frequencies, ΔS_{int} values are being severely underestimated. The quasi-RRHO approximation, as a result, is not applicable to late TSs (such as dehydrogenation) that possess highly anharmonic modes.

It is also interesting to note that experimental ΔS_{int} in MWW is significantly lower than that in STF, and similar to entropies in Type 2 active sites. This further strengthens our proposition that, in addition to the supercage, the independent sinusoidal channel in MWW may also be involved in reaction kinetics, in which case the averaged entropy of activation will be lower than if only the T4 site in the supercage was the active center.

5.5 Conclusions

Intrinsic enthalpies of activation for monomolecular cracking and dehydrogenation of n-butane can be accurately estimated for various zeolite frameworks using the QM/MM model together with dispersion-corrected DFT and a quasi-RRHO approximation. Although it is difficult to deduce active centers from experimental data, an examination of representative active sites using computations can shed light on the preferred sites and pore geometries

for each reaction pathway. Enthalpies of activation for both central and terminal cracking are relatively insensitive to the location of the active site. On the other hand, comparison between experiments and computations reveals a distinct pathway preference for dehydrogenation. In general, the methylene pathway is preferred for active sites in both channels as well as channel intersections owing to lower enthalpic barrier that occurs there than for the methyl pathway. Within active sites in cages, however, methyl dehydrogenation seems to be occur almost exclusively, which can be attributed to entropy compensation occurring in larger, less confined cavities.

However, it is difficult to evaluate entropy compensation effects owing to the limited accuracy of the quasi-RRHO approach in the presence of soft degrees of freedom and anharmonicities. As a result, application of the quasi-RRHO approach is limited to active sites in the narrow channels of 10-MR zeolite frameworks where both the reactant and TS are highly confined relative to intersections and cages. For more accurate entropies of activation, therefore, there is a need for superior methods to handle anharmonic vibrations[18, 151], which utilize anharmonic potential functions to calculate diagonal corrections to harmonic vibrational frequencies. Future work will involve the application of such computational tools, which can calculate both enthalpies and entropies accurately, to the detailed examination of the impact of active site location and pore geometry on reaction selectivity.

5.6 Acknowledgements

This work was supported by a grant from Chevron Energy Technology Co. We also thank Amber Janda for helpful discussions on confinement effects, and for providing experimental data.

Chapter 6

Wavefunction Stability Analysis without Analytical Electronic Hessians: Application to Orbital-Optimized Second Order Møller–Plesset Theory and VV10-containing Density Functionals

6.1 Abstract

Wavefunction stability analysis is commonly applied to converged self-consistent field (SCF) solutions to verify whether the electronic energy is a local minimum with respect to second order variations in the orbitals. By iterative diagonalization, the procedure calculates the lowest eigenvalue of the stability matrix or electronic hessian. However, analytical expressions for the electronic hessian are unavailable for most advanced post-Hartree Fock (HF) wave function methods and even some Kohn-Sham (KS) density functionals. To address such cases, we formulate the hessian-vector product within the iterative diagonalization procedure as a finite difference of the electronic gradient with respect to orbital perturbations in the direction of the vector. As a model application, following the lowest eigenvalue of the orbital-optimized second order Møller–Plesset perturbation theory (OOMP2) hessian during H_2 dissociation reveals the surprising stability of the spin-restricted solution at all separations, with a second independent unrestricted solution. We show that a single stable solution can be recovered by using the regularized OOMP2 method (δ-OOMP2), which contains a level shift. Internal and external stability analyses are also performed for SCF solutions of a recently developed range-separated hybrid density functional, ωB97X-V, for which the analytical hessian is not yet available due to the complexity of its long-range non-local VV10

correlation functional.

6.2 Introduction

Self-consistent field (SCF) solutions to wavefunction theory and Kohn-Sham (KS)[93, 94] formalism of density functional theory (DFT) are typically determined by imposing constraints on the spin orbitals. These constraints not only lower SCF costs, but also allow the approximate wavefunction to share some properties in common with the exact wavefunction such as spin or spatial symmetry. Variational minimization ensures that the energy is stationary with respect to first order changes in the spin orbitals. Therefore, second derivatives with respect to spin orbital coefficients must be positive for the energy to be a true local minimum, and the procedure to verify this condition is termed stability analysis.

Thouless originally derived the conditions for stability of HF wavefunctions from second quantization[152]. This was followed by a density matrix-based approach[153], and a reformulation of the Thouless conditions to treat both closed and open-shell systems[154, 155]. Seeger and Pople[21] devised a systematic approach to treat HF instability beginning with real spin-restricted HF orbitals, and progressively removing each of these constraints. For each case, they obtained the conditions for internal stability, where spin orbitals are varied within the space of defined constraints, as well as external stability where one constraint is removed at a time. Stability analysis for HF involves the calculation of the lowest eigenvalue of a stability matrix (or electronic hessian). Since diagonalization of the large stability matrix (whose elements form a fourth rank tensor) may be prohibitive, stability analysis employs iterative diagonalization techniques such as the Davidson method[80]. Fortunately, the critical step in iterative diagonalization, which involves contraction of the stability matrix with a trial vector, can be performed in a manner very similar to forming a Fock matrix. Therefore the cost of SCF stability analysis is comparable to SCF costs.

The HF solution is typically used as a reference for advanced methods that incorporate correlation such as second order Møller–Plesset perturbation theory (MP2) and coupled cluster (CC) theory, although HF orbitals quite commonly suffer from spatial or spin symmetry-breaking. To address these problems, orbital-optimized second-order perturbation theory (OOMP2)[156] distinguishes itself from standard MP2 by optimizing the zeroth order orbitals in the presence of correlation in an approach based on approximate Brueckner orbitals[157]. By optimizing the single reference, artificial spin contamination can be removed[156–159] and energies as well as properties of open shell molecules can be significantly improved[156–158, 160–162]. Because the energy is made stationary to changes in the orbitals, a Hellman-Feynman condition applies and all first order properties will be continuous as the orbitals change continuously[163]. Recently, δ-OOMP2 has been developed as a simple way to regularize the method against small HOMO-LUMO gaps as well as removing systematic errors in the method[164]. While approximate forms have been applied in previous

studies[158], full analytical expressions for the electronic hessian are unavailable and finite difference electronic hessians are intractable. As a result, the stability of spin-restricted and unrestricted formalisms of OOMP2 has not been properly investigated. For the same reason, stability analysis is not available for size-consistent, Brueckner orbital-based coupled cluster techniques such as Brueckner theory doubles (BD)[165] and optimized-orbital coupled cluster doubles (OD)[157, 160, 166].

The stability conditions for density functionals are essentially analogous to HF, and have been derived by Bauernschmitt and Ahlrichs for internal (singlet) and external (triplet) stability of restricted KS-DFT [167]. The formalism, however, requires calculation of second derivatives of the exchange-correlation energy. Analytical expressions for the second derivative of the exchange correlation term in KS-DFT are not available for all functionals. ωB97X-V, for instance, is a minimally parameterized range-separated hybrid functional that can accurately capture both non-covalent interactions as well as thermochemistry[168]. The functional includes non-local correlation described by VV10[169], for which an analytical form of the hessian has not yet been derived. In such cases, stability analysis can prove intractable since calculation and diagonalization of the full finite difference electronic hessian is not feasible.

Our aim is to establish a technique for stability analysis that is readily applicable to any post-HF or KS-DFT method, regardless of the availability of analytical second derivatives of electronic energy. We have previously reported a finite differences implementation of the Davidson method to calculate the lowest eigenvalue of a nuclear hessian, which can determine whether a stationary point calculated using geometry optimization is a minimum or saddle point. The same approach can be extended to wavefunction space, where the finite differences Davidson method is applied to perturbations in the molecular orbitals in order to calculate the lowest eigenvalue of the electronic hessian[170]. Potential curves for dissociation of H_2 are calculated to analyze the stability of SCF solutions for OOMP2 and δ-OOMP2 theory, with some interesting and in some ways remarkable results. Additionally, finite-difference based stability analysis is applied to the ωB97X-V functional in order to demonstrate the utility of this technique when second derivatives are unavailable.

6.3 Method

The Davidson method is an iterative diagonalization procedure to determine a few extreme eigenvalues of large symmetric matrices when full diagonalization is prohibitive. The algorithm is described in detail elsewhere[80, 171]. Briefly, the procedure employs a small orthonormal subspace of vectors, $B_k = [b_i]$ at each iteration k, consisting of dominant components of the desired eigenvector of a matrix, A. A smaller interaction matrix, $B_k^T A B_k$, is constructed and diagonalized to obtain the lowest/highest eigenpair, (λ_k, y_k). The Ritz vector, $x_k = B_k y_k$, is then used to estimate the residual error between the exact and approx-

imate eigenvector, $r_k = -(\lambda_k I - A)x_k$. The initial subspace is augmented with a new vector that contains this information, and the procedure is iterated until convergence.

The Davidson method was originally applied to large-scale configurational interaction (CI) treatment of wavefunctions[80, 172]. The finite difference implementation of the Davidson method can be used when the matrix calculation itself is intractable. For instance, if the matrix A corresponds to the hessian of the energy with respect to nuclear displacements, the exact matrix-vector product, Ab_1, is replaced with a finite difference approximation in terms of the gradient of the energy (∇E)

$$Ab_1 \approx \frac{\nabla E(X_0 + \xi b_1) - \nabla E(X_0 - \xi b_1)}{2\xi} \tag{6.1}$$

where b_1 is the subspace guess, X_0 corresponds to nuclear coordinates of a system, and ξ is the finite difference step. This expression can be used to calculate a few key eigenvectors as inputs to mode-following methods for transition state searches on nuclear potential energy surfaces[73–75]. The same principle can also be applied to selective mode tracking in vibrational analysis[76, 77], and characterization of stationary points[78, 170], where the lowest one or two eigenvalues of the nuclear hessian are sufficient to verify whether a geometry corresponds to a minimum or transition state, respectively.

Wavefunction stability analysis also requires only the lowest eigenvalue of the electronic hessian. Therefore, the finite difference Davidson approach can be extended to stability analysis in cases where analytical hessians are either expensive or unavailable. Since rotations between occupied-occupied or virtual-virtual orbitals do not affect the total energy, stability analysis is carried out in the space of occupied-virtual rotations. The most obvious choice for the initial subspace guess, therefore, corresponds to a HOMO-LUMO rotation. To avoid possible orthogonality between the guess and the exact eigenvector, a small amount of randomness is added in to the subspace guess.

Orbital perturbation in the occupied-virtual space along the subspace guess closely follows the procedure outlined by Van Voorhis and Head-Gordon[173]. A skew-symmetric unitary transformation matrix,$U_{1\pm}$, is determined by first scaling the guess,

$$\Delta_{1\pm} = \pm\xi b_1 \tag{6.2}$$

where b_1 is the subspace guess corresponding to HOMO-LUMO rotation, $\xi(= 0.01)$ is the finite difference step, and the number in the subscript corresponds to the iteration. The transformation matrix is then given by

$$U_{1\pm} = e^{\Delta_{1\pm}} \tag{6.3}$$

The off-diagonal elements of this matrix correspond to rotations in the occupied-virtual space. The rotated orbitals are given by a unitary transformation of the converged SCF

orbital coefficients, C_0^σ, where corresponds to α- or β-spin.

Rotations of α-spin and β-spin orbital coefficients are identical during internal stability analysis of restricted or unrestricted spin orbitals. In order to examine external stability of restricted spin orbitals, on the other hand, spin symmetry needs to be broken. Therefore, α-spin and β-spin orbital coefficients are rotated in opposite directions.

$$C_{1+}^\beta = -C_{1+}^\alpha \quad \text{and} \quad C_{1-}^\beta = -C_{1-}^\alpha \tag{6.4}$$

The hessian-vector product Davidson iterations is then calculated similar to equation 6.1 using finite differences of gradients with respect to the rotated coefficients

$$Ab_1 \approx \left[\frac{\nabla E(C_{1+}^\alpha) - \nabla E(C_{1-}^\alpha)}{2\xi}, \frac{\nabla E(C_{1+}^\beta) - \nabla E(C_{1-}^\beta)}{2\xi} \right]^T \tag{6.5}$$

where A corresponds to the electronic hessian. The Davidson algorithm proposed by Sleijpen and van der Vorst[174] is then employed to iteratively calculate the lowest eigenvalue.

Convergence can be accelerated using a good preconditioner for the residual. In the original Davidson algorithm, the preconditioner at the k^{th} iteration, Ξ_k, is given by

$$\Xi_k = (\lambda_k I - D)^{-1} \tag{6.6}$$

where D is a matrix consisting of the diagonal elements of A. A reasonable guess for the diagonal hessian is the difference between orbital eigenvalues, ϵ, in the occupied-virtual space[173],

$$D_{ia,jb} = (\epsilon_a - \epsilon_i)\delta_{ij}\delta_{ab} \tag{6.7}$$

where subscripts (i, j) correspond to occupied orbitals and (a, b) to virtual orbitals. In order to ensure the convergence of the method to the lowest eigenvalue, the preconditioner must be negative definite[171]. In cases where preconditioning exceeds a certain cutoff, the cutoff value replaces the difference between the eigenvalue and diagonal element. The chosen value, $\Delta E = -0.1E_h$, is determined using simple benchmarking of the H_2 molecule at equilibrium separation with B3LYP[86, 87], and correlation-consistent basis sets. The technique is implemented in a developmental version of Q-Chem 4.2[175], in order to examine internal stability of real restricted or unrestricted orbitals, as well as external stability of restricted orbitals for OOMP2 theory and any KS-DFT.

6.4 Results

6.4.1 HF vs. orbital-optimized MP2 for bond dissociation

Bond dissociation problems are an important application of stability analysis. The reason is that many orbital optimization methods will not automatically change the character of

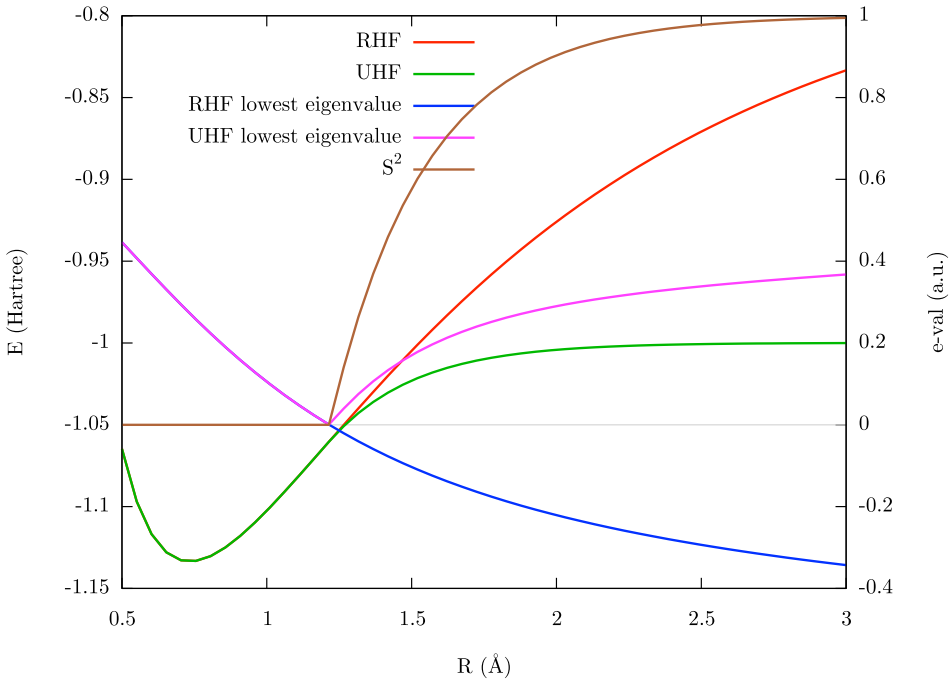

Figure 6.1: Potential curves (green for unrestricted and red for restricted, where it differs from unrestricted) for the dissociation of H_2 and the associated lowest eigenvalues of the stability matrix (purple for internal stability of the unrestricted solution, blue for external stability of the restricted solution, where it differs from unrestricted) at the Hartree-Fock (HF) level. The lowest energy solution changes character from restricted to unrestricted when the former becomes unstable.

the orbitals from restricted to unrestricted as the bond is stretched, and therefore stability analysis is needed to detect such a change. Figure 6.1 illustrates the standard result seen for Hartree-Fock theory for the toy problem of H_2 dissociation. The RHF to UHF instability is detected by a sign change of the smallest eigenvalue, which occurs at a bond-length of about 1.2Å. Beyond this distance, the UHF solution exhibits an increasing positive smallest eigenvalue and becomes a distinct, lower energy solution, whilst the smallest eigenvalue of the RHF solution becomes steadily more negative.

How does the inclusion of electron correlation in the OOMP2 method affect this picture? The results are shown in Figure 6.2, and at first glance the ROOMP2 and UOOMP2 energy curves look qualitatively similar to the RHF and UHF ones. However the ROOMP2 energy reaches a maximum value around 2.8Å and then begins to turn over, as a result of the HOMO-LUMO gap decreasing. The ROOMP2 and UOOMP2 curves actually cross again at still larger separations than are shown on the figure. What are the implications for orbital stability analysis? Using the finite difference stability analysis code yields very interesting

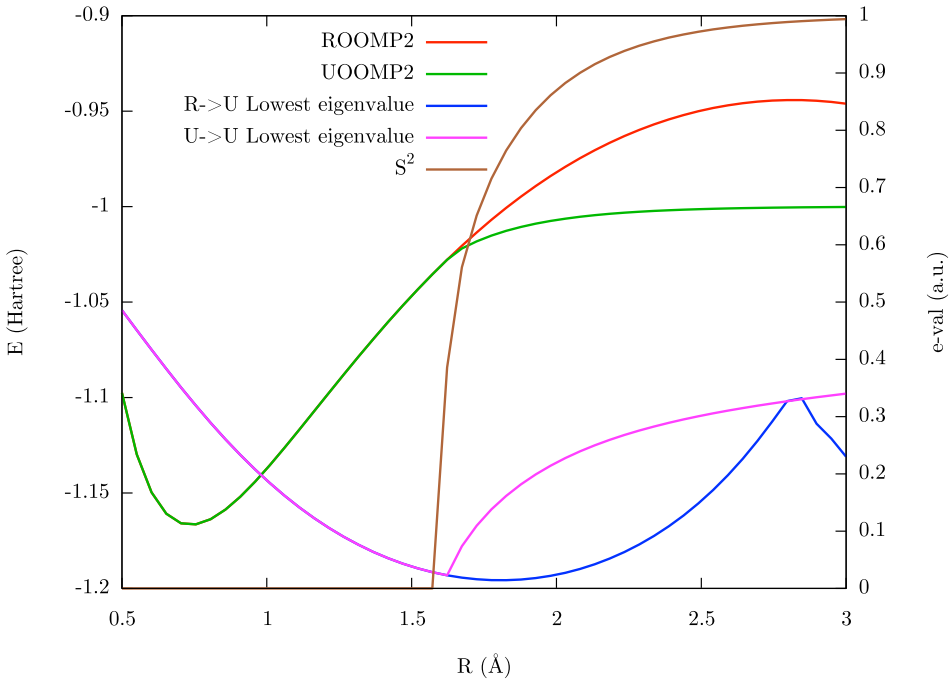

Figure 6.2: Potential curves for the dissociation of H_2 and the associated lowest eigenvalues of the stability matrix using orbital optimized MP2 (OOMP2) in the cc-pVDZ basis. The format follows Figure 6.1. OOMP2 behaves qualitatively differently from HF (see Figure 6.1). Restricted solution is stable (positive eigenvalue) to spin-polarization at all bond-lengths, and a distinct stable unrestricted solution appears at partially stretched bondlengths.

results. The ROOMP2 and UOOMP2 solutions are in fact both stable when they are distinct solutions. They apparently do not coalesce upon going to shorter bond-lengths.

As a surprising consequence, despite the Hellman-Feynman condition for OOMP2, there are still first derivative discontinuities in the dissociation curve for single bond dissociations such as H_2. It is scarcely visible in Figure 6.2, but this is nonetheless a real effect. As a result of the ROOMP2 solution always being a true minimum in orbital space, the UOOMP2 solution must cross it in the energy coordinate without crossing in orbital space.

To better understand the topography of the solutions we look at the UOOMP2 energy for H_2 as a function of spin-polarization from the ROOMP2 solution in the minimal basis case where there is only a single orbital rotation angle (θ_α and θ_β) in each of the α and β spaces. A spin polarization angle, ϕ, can therefore be defined such that $\theta_\alpha = \phi$ and $\theta_\beta = -\phi$. Figure 6.3 shows the OOMP2 energy as a function of ϕ for a number of bond lengths close to the crossing, from ROOMP2 being lowest energy to UOOMP2 being lowest. The key observation from Figure 6.3 is the appearance of a second minimum at non-zero ϕ as the

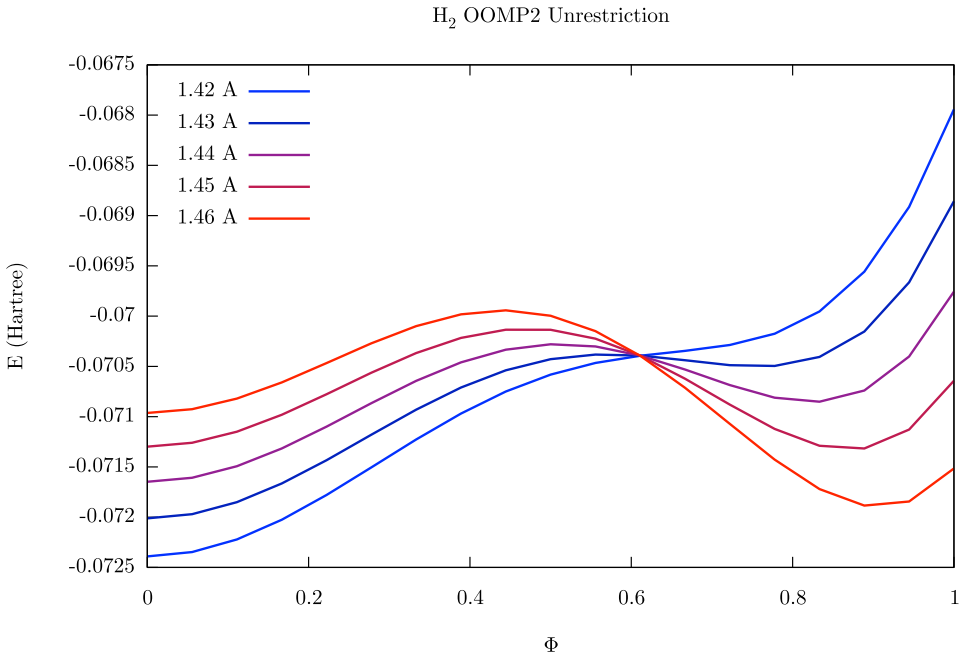

Figure 6.3: The dependence of the OOMP2 energy of H_2 in a minimal basis on the spin polarization angle (see text for definition) at a series of bond-lengths around the critical value at which the character of the lowest energy solution changes. There are two local minima, one restricted and one unrestricted, at these bond-lengths, and at the critical bond-length the nature of the lowest energy solution switches discontinuously.

bond is stretched, whilst the first stationary point ($\phi = 0$) remains a minimum. As the bond-length increases, the second solution eventually becomes the global minimum leading to the discontinuous change in orbitals as we follow the lowest energy orbitals.

While there is no reason to assume that the global minimum of a nonlinear problem will not jump between multiple minima as parameters change, it is still surprising to see it here due to our experience with HF (as exemplified by Figure 6.1). HF is a diagonalization-based approach, and so two states with the same energy that can couple through the Hamiltonian should split in energy. OOMP2 on the other hand adds a perturbative correction, which in this case preferentially stabilizes the restricted solution and lowers its energy relative to the unrestricted orbitals bringing their energies to coalescence. Similar observations have been made in the context of orbital optimization in active space methods[176, 177]. In cases such as these, as a consequence of the discontinuous change in orbitals, the potential energy surface exhibits a first derivative discontinuity at the point of the jump in orbital solutions (here, the ROOMP2 to UOOMP2 transition).

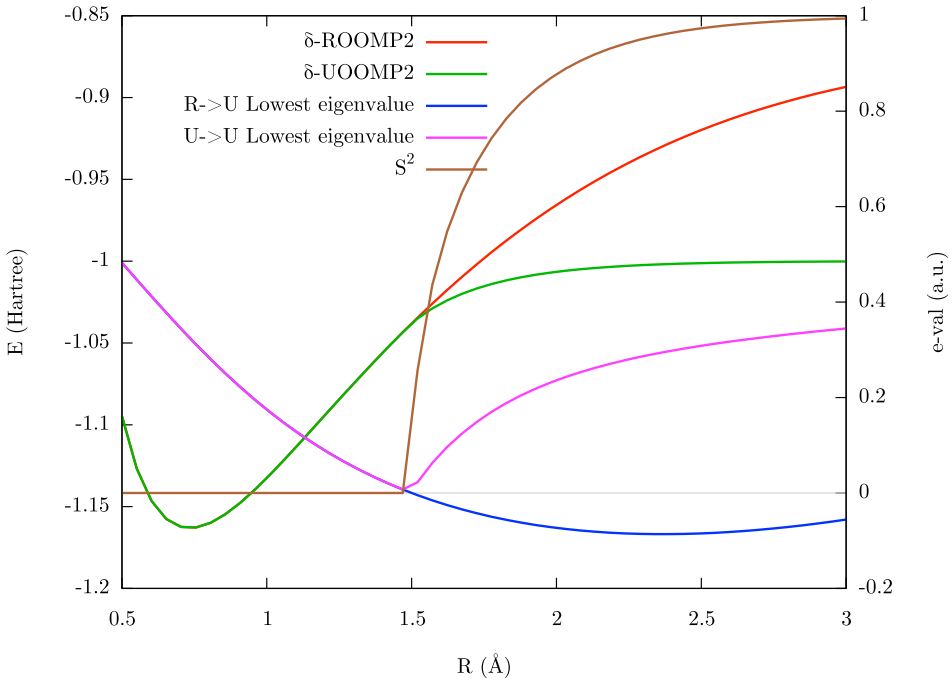

Figure 6.4: Potential curves for the dissociation of H_2 and the associated lowest eigenvalues of the stability matrix using regularized orbital optimized MP2 (δ-OOMP2) in the cc-pVDZ basis. The format follows Figure 6.1. δ-OOMP2 behaves qualitatively differently from OOMP2 (see Figure 6.2), but is similar to HF (see Figure 6.1). The restricted solution becomes unstable at a critical bond-length, beyond which the unrestricted solution is lowest in energy.

How might one overcome this unphysical behavior of OOMP2, and recover smoother potential energy surfaces? We cannot give a complete answer here, but we can apply stability analysis to a modified form of OOMP2 that includes a fixed level shift of 0.4 a.u., termed δ-OOMP2. δ-OOMP2 has been shown to yield systematic improvements relative to OOMP2 across a broad range of properties while being robust to divergences during orbital optimization[164]. The performance of δ-OOMP2 for the dissociation of H_2 is shown in Figure 6.4, and presents a striking contrast with OOMP2 shown in Figure 6.2. δ-OOMP2 shows only one stable solution at any geometry, like HF, and unlike OOMP2. As a consequence, as shown in Figure 6.5 for minimal basis H_2, the optimized orbitals for the global minimum do not change discontinuously as the bond is stretched, and thus the potential energy surface is continuous through first derivatives. Further calculations on a much larger range of molecules are required to test the generality of the present positive result, and the stability analysis method introduced here is a crucial tool for this purpose.

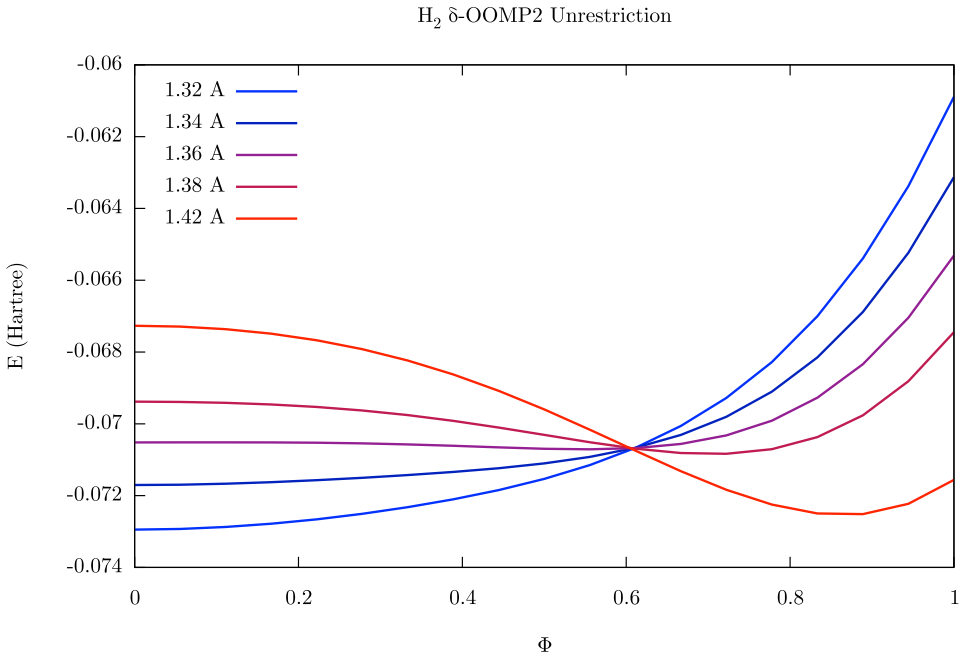

Figure 6.5: The dependence of the δ-OOMP2 energy of H_2 in a minimal basis on the spin polarization angle (see text for definition) at a series of bond-lengths around the critical value at which the character of the lowest energy solution changes. For any given bond-length there is only one local minimum, which changes character from restricted to unrestricted at the critical bond-length.

6.4.2 Density functional theory

Using their formulation of stability analysis for KS-DFT, Bauernschmitt and Ahlrichs[167] calculate critical distances for the onset of external instability in dissociating systems. Along similar lines, dissociation calculations are performed on H_2, and results are compared for restricted HF, B3LYP, and ωB97X-V, and the finite difference Davidson approach is employed to calculate the lowest eigenvalue for the latter. Since ωB97X-V is trained using very large basis sets in the absence of counterpoise corrections[168], the aug-cc-pVTZ[178] basis set is employed. The critical distances determined with HF, B3LYP and ωB97X-V are 1.21, 1.49 and 1.53Å, respectively, consistent with the fact that onset of external instability occurs later in density functionals owing to the inclusion of approximate correlation.

In addition to external stability of restricted ωB97X-V, internal stability analysis of the unrestricted formalism is also a useful diagnostic tool since the SCF solution can depend heavily on the quality of the initial guess. For instance, SCF minimization of singlet methylene[179] (C-H bond distance = 1.11Å, H-C-H angle = 101.896^0) with unrestricted

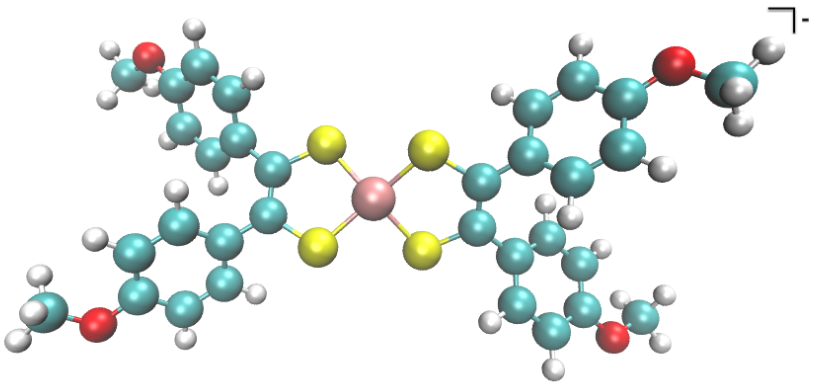

Figure 6.6: Structure of dimeric cobalt-diaryldithiolene complex, a potential catalyst for electrocatalytic proton reduction in nonaqueous media. Cobalt is in the center surrounded by sulfur atoms (yellow), and the aryl groups are para-substituted with methoxy groups (oxygen atoms in red).

ωB97X-V/aug-cc-PVQZ converges to an unstable solution if the initial SCF guess consists of superposition of atomic densities. The lowest eigenvector corresponding to the unstable solution, calculated either with ωB97X-V or a lower level of theory, can then be used to search for a lower energy solution with ωB97X-V. The resulting orbital coefficients constitute a significantly better SCF guess that converges to the correct singlet ground state, which is 0.004 E_h lower in energy than the unstable solution.

Stability analysis is also essential for molecules containing transition metals, where multiple spin states can emerge from SCF calculations. To illustrate, we examine the stability of an organometallic electrocatalyst for cathodic hydrogen evolution reaction (HER), with potential application in the conversion of solar energy to fuels. The catalyst, shown in Figure 6.6, is a dimeric cobalt-diaryldithiolene complex with methoxy groups substituted in the aryl

para positions[90]. The structure is optimized at the BP86/6-31G* level of theory[86, 88]. If the SCF cycles in the subsequent unrestricted single point energy calculation at ωB97X-V/6-31G* converge to a spin singlet, finite difference stability analysis shows that the solution is internally unstable. The stable solution, with $\langle S^2 \rangle$ of 0.94, is 0.023 E_h lower in energy. While calculation and diagonalization of the full finite difference hessian within the original stability analysis framework can be prohibitive for systems of this size, applying the finite difference Davidson method to the stable solution costs only about 44 SCF steps. This procedure is therefore not only useful to study bond dissociation characteristics in the absence of analytical electronic hessians, but is also a practical tool for examining the stability of large, complex systems.

6.5 Conclusions

Stability analysis has thus far been limited to formalisms for which analytical second derivatives are available since the cost of full finite difference hessian calculation is prohibitive. We describe a hessian-free approach in which the hessian-vector product required for iterative diagonalization within the Davidson method is approximated by finite differences of the gradients with respect to rotation of molecular orbital coefficients in the occupied-virtual space. The procedure is implemented for both orbital-optimized post-HF methods such as OOMP2 as well as DFT, and can successfully examine internal and external stability with respect to spin symmetry constraints. In future, the implementation will also include internal and external stability analysis for complex as well as general spin orbitals. The technique will also be made available for other orbital-optimized methods such as coupled cluster-based BD and OD, for which stability analysis has hitherto not been performed.

6.6 Acknowledgements

David Stück and Dr. Eric Sundstrom were collaborators on this project. This research was supported by a grant from Chevron Energy Technology Co., by the Department of Energy Office of Science Graduate Fellowship Program (DOE SCGF), made possible in part by the American Recovery and Reinvestment Act of 2009, administered by ORISE-ORAU under contract no. DE-AC05- 06OR23100, and by the Office of Science, Office of Basic Energy Sciences, of the (U.S.) Department of Energy under Contract No. DE-AC02-05CH11231. We are also grateful to Narbe Mardirossian for providing instructive examples for the stability analysis with the ωB97X-V functional, and Dr. Julien Panetier for electrocatalyst geometries. We acknowledge computational resources obtained under National Science Foundation (NSF) Award No. CHE-1048789 and NSF CHE-0840505.

Bibliography

(1) McIver, J. W.; Komornicki, A. *J. Am. Chem. Soc.* **1972**, *94*, 2625–2633.

(2) Cerjan, C. J.; Miller, W. H. *J. Chem. Phys.* **1981**, *75*, 2800–2806.

(3) Schlegel, H. B. *WIREs Comput. Mol. Sci.* **2011**, *1*, 790–809.

(4) Henkelman, G.; Uberuaga, B. P.; Jónsson, H. *J. Chem. Phys.* **2000**, *113*, 9901–9904.

(5) Henkelman, G.; Jónsson, H. *J. Chem. Phys.* **1999**, *111*, 7010–7022.

(6) Baker, J. *J. Comput. Chem.* **1986**, *7*, 385–395.

(7) Schlegel, H. B. *J. Comput. Chem.* **1982**, *3*, 214–218.

(8) Corma, A. *Chem. Rev.* **1995**, *95*, 559–614.

(9) Vermeiren, W.; Gilson, J.-P. *Top. Catal.* **2009**, *52*, 1131–1161.

(10) Dědeček, J.; Sobalík, Z.; Wichterlová, B. *Catal. Rev.* **2012**, *54*, 135–223.

(11) Ramachandran, C.; Williams, B.; Bokhoven, J. van; Miller, J. *J. Catal.* **2005**, *233*, 100 –108.

(12) Bhan, A.; Gounder, R.; Macht, J.; Iglesia, E. *J. Catal.* **2008**, *253*, 221–224.

(13) Grimme, S. *J. Comput. Chem.* **2004**, *25*, 1463–1473.

(14) Rozanska, X.; Santen, R. A. van; Hutschka, F.; Hafner, J. *J. Am. Chem. Soc.* **2001**, *123*, 7655–7667.

(15) Bakowies, D.; Thiel, W. *J. Phys. Chem.* **1996**, *100*, 10580–10594.

(16) De Moor, B. A.; Reyniers, M.-F.; Marin, G. B. *Phys. Chem. Chem. Phys.* **2009**, *11*, 2939–2958.

(17) Grimme, S. *Chem. Eur. J.* **2012**, *18*, 9955–9964.

(18) Beste, A. *Chem. Phys. Lett.* **2010**, *493*, 200 –205.

(19) Bučko, T. *J. Phys. Condens. Matter* **2008**, *20*, 064211.

(20) Zimmerman, P. M.; Tranca, D. C.; Gomes, J.; Lambrecht, D. S.; Head-Gordon, M.; Bell, A. T. *J. Am. Chem. Soc.* **2012**, *134*, 19468–19476.

(21) Seeger, R.; Pople, J. A. *J. Chem. Phys.* **1977**, *66*, 3045–3050.

(22) Schlegel, H. B. *J. Comput. Chem.* **2003**, *24*, 1514–1527.

(23) Berti, P. J.; Blanke, S. R.; Schramm, V. L. *J. Am. Chem. Soc.* **1997**, *119*, 12079–12088.

(24) Bell, A. T.; Head-Gordon, M. *Annu. Rev. Chem. Biomol. Eng.* **2011**, *2*, PMID: 22432627, 453–477.

(25) Keil, F. In *Multiscale Molecular Methods in Applied Chemistry*, Kirchner, B., Vrabec, J., Eds.; Topics in Current Chemistry, Vol. 307; Springer Berlin Heidelberg: 2012, pp 69–107.

(26) Mills, G.; Jónsson, H. *Phys. Rev. Lett.* **1994**, *72*, 1124–1127.

(27) Henkelman, G.; Jónsson, H. *J. Chem. Phys.* **2000**, *113*, 9978–9985.

(28) Trygubenko, S. A.; Wales, D. J. *J. Chem. Phys.* **2004**, *120*, 2082–2094.

(29) Chu, J.-W.; Trout, B. L.; Brooks, B. R. *J. Chem. Phys.* **2003**, *119*, 12708–12717.

(30) E, W.; Ren, W.; Vanden-Eijnden, E. *Phys. Rev. B* **2002**, *66*, 052301.

(31) E, W.; Ren, W.; Vanden-Eijnden, E. *J. Phys. Chem. B.* **2005**, *109*, 6688–6693.

(32) E, W.; Ren, W.; Vanden-Eijnden, E. *J. Chem. Phys.* **2007**, *126*, 164103.

(33) Burger, S. K.; Yang, W. *J. Chem. Phys.* **2006**, *124*, 054109.

(34) Burger, S. K.; Yang, W. *J. Chem. Phys.* **2007**, *127*, 164107.

(35) Chaffey-Millar, H.; Nikodem, A.; Matveev, A. V.; Krüger, S.; Rösch, N. *J. Chem. Theory Comput.* **2012**, *8*, 777–786.

(36) Granot, R.; Baer, R. *J. Chem. Phys.* **2008**, *128*, 184111.

(37) Peters, B.; Heyden, A.; Bell, A. T.; Chakraborty, A. *J. Chem. Phys.* **2004**, *120*, 7877–7886.

(38) Quapp, W. *J. Chem. Phys.* **2005**, *122*, 174106.

(39) Goodrow, A.; Bell, A. T.; Head-Gordon, M. *J. Chem. Phys.* **2008**, *129*, 174109.

(40) Goodrow, A.; Bell, A. T.; Head-Gordon, M. *J. Chem. Phys.* **2009**, *130*, 244108.

(41) Goodrow, A.; Bell, A. T.; Head-Gordon, M. *Chem. Phys. Lett.* **2010**, *484*, 392 –398.

(42) Behn, A.; Zimmerman, P. M.; Bell, A. T.; Head-Gordon, M. *J. Chem. Phys.* **2011**, *135*, 224108.

(43) Heyden, A.; Bell, A. T.; Keil, F. J. *J. Chem. Phys.* **2005**, *123*, 224101.

(44) Simons, J.; Joergensen, P.; Taylor, H.; Ozment, J. *J. Phys. Chem.* **1983**, *87*, 2745–2753.

(45) Wales, D. J. *J. Chem. Soc. Faraday Trans.* **1992**, *88*, 653–657.

(46) Wales, D. J. *J. Chem. Soc. Faraday Trans.* **1993**, *89*, 1305–1313.

(47) Munro, L. J.; Wales, D. J. *Phys. Rev. B* **1999**, *59*, 3969–3980.

(48) Maeda, S.; Ohno, K.; Morokuma, K. *J. Chem. Theory Comput.* **2009**, *5*, 2734–2743.

(49) Ayala, P. Y.; Schlegel, H. B. *J. Chem. Phys.* **1997**, *107*, 375–384.

(50) Campo, J. M. del; Köster, A. M. *J. Chem. Phys.* **2008**, *129*, 024107.

(51) Cancès, E.; Legoll, F.; Marinica, M.-C.; Minoukadeh, K.; Willaime, F. *J. Chem. Phys.* **2009**, *130*, 114711.

(52) Johnson, B. G.; Fisch, M. J. *J. Chem. Phys.* **1994**, *10*, 7429–7442.

(53) Amos, R. D.; Rice, J. E. *Comput. Phys. Rep.* **1989**, *10*, 147–187.

(54) Halgren, T. A.; Lipscomb, W. N. *Chem. Phys. Lett.* **1977**, *49*, 225 –232.

(55) Behn, A.; Zimmerman, P. M.; Bell, A. T.; Head-Gordon, M. *J. Chem. Theory Comput.* **2011**, *7*, 4019–4025.

(56) Fletcher, R., *Practical Methods of Optimization Vol 1: Unconstrained Optimization*; Wiley, NY: 1980.

(57) Head, J. D.; Zerner, M. C. *Chem. Phys. Lett.* **1985**, *122*, 264 –270.

(58) Bernhard Schlegel, H. *Theor. Chim. Acta.* **1984**, *66*, 333–340.

(59) Lindh, R.; Bernhardsson, A.; Karlström, G.; Malmqvist, P.-Å. *Chem. Phys. Lett.* **1995**, *241*, 423 –428.

(60) Baker, J.; Kessi, A.; Delley, B. *J. Chem. Phys.* **1996**, *105*, 192–212.

(61) Pulay, P.; Fogarasi, G. *J. Chem. Phys.* **1992**, *96*, 2856–2860.

(62) Wilson, E. B.; Decius, J. C.; Cross, P. C., *Molecular vibrations: The theory of infrared and Raman vibrational spectra.* 6th ed.; New York: McGraw-Hill.: 1955.

(63) Anoshkina, E. V.; Belyaev, A. G.; Seidel, H.-P. In, 2002; Chapter Asymptotic Analysis of Three-Point Approximations of Vertex Normals and Curvatures.

(64) Gül, Ş.; Schoenebeck, F.; Aviyente, V.; Houk, K. N. *J. Org. Chem.* **2010**, *75*, 2115–2118.

(65) Shao, Y. et al. *Phys. Chem. Chem. Phys.* **2006**, *8*, 3172–3191.

(66) Fukui, K. *J. Chem. Phys.* **1970**, *74*, 4161–4163.

(67) Ishida, K.; Morokuma, K.; Komornicki, A. *J. Chem. Phys.* **1977**, *66*, 2153–2156.

(68) Page, M.; McIver, J. W. *J. Chem. Phys.* **1988**, *88*, 922–935.

(69) Gonzalez, C.; Schlegel, H. B. *J. Phys. Chem.* **1990**, *94*, 5523–5527.

(70) Melissas, V. S.; Truhlar, D. G.; Garrett, B. C. *J. Chem. Phys.* **1992**, *96*, 5758–5772.

(71) Jackels, C. F.; Gu, Z.; Truhlar, D. G. *J. Chem. Phys.* **1995**, *102*, 3188–3201.

(72) Kumeda, Y.; Wales, D. J.; Munro, L. J. *Chem. Phys. Lett.* **2001**, *341*, 185 –194.

(73) Sawamura, A. *JSIAM Letters* **2011**, *3*, 17–19.

(74) Vreven, T.; Frisch, M. J.; Kudin, K. N.; Schlegel, H. B.; Morokuma, K. *Mol. Phys.* **2006**, *104*, 701–714.

(75) Olsen, R. A.; Kroes, G. J.; Henkelman, G.; Arnaldsson, A.; Jónsson, H. *J. Chem. Phys.* **2004**, *121*, 9776–9792.

(76) Reiher, M.; Neugebauer, J. *J. Chem. Phys.* **2003**, *118*, 1634–1641.

(77) Kaledin, A. L. *J. Chem. Phys.* **2005**, *122*, 184106.

(78) Deglmann, P.; Furche, F. *J. Chem. Phys.* **2002**, *117*, 9535–9538.

(79) Mallikarjun Sharada, S.; Zimmerman, P. M.; Bell, A. T.; Head-Gordon, M. *J. Chem. Theory Comput.* **2012**, *8*, 5166–5174.

(80) Davidson, E. R. *J. Comput. Phys.* **1975**, *17*, 87 –94.

(81) Baglama, J.; Calvetti, D.; Reichel, L. *BIT* **1996**, *36*, 400–421.

(82) Cullum, J.; Willoughby, R. A. *J. Comput. Phys.* **1981**, *44*, 329 –358.

(83) Sorensen, D. C.; Yang, C. *SIAM J. Matrix Anal. A* **1998**, *19*, 1045–1073.

(84) Butscher, W.; Kammer, W. *J. Comput. Phys.* **1976**, *20*, 313 –325.

(85) Margl, P. *Can. J. Chemistry* **2009**, *87*, 891–903.

(86) Becke, A. D. *Phys. Rev. A* **1988**, *38*, 3098–3100.

(87) Lee, C.; Yang, W.; Parr, R. G. *Phys. Rev. B* **1988**, *37*, 785–789.

(88) Perdew, J. P. *Phys. Rev. B* **1986**, *33*, 8822–8824.

(89) Zhang, M.; Geng, Z.; Yu, Y. *Energy Fuels* **2011**, *25*, 2664–2670.

(90) Letko, C. S.; Panetier, J. A.; Head-Gordon, M.; Tilley, T. D. *J. Am. Chem. Soc.* **2014**, *136*, 9364–9376.

(91) Wachters, A. J. H. *J. Chem. Phys.* **1970**, *52*, 1033–1036.

(92) Tuma, C.; Sauer, J. *Phys. Chem. Chem. Phys.* **2006**, *8*, 3955–3965.

(93) Hohenberg, P.; Kohn, W. *Phys. Rev.* **1964**, *136*, B864–B871.

(94) Kohn, W.; Sham, L. J. *Phys. Rev.* **1965**, *140*, A1133–A1138.

(95) Swisher, J. A.; Hansen, N.; Maesen, T.; Keil, F. J.; Smit, B.; Bell, A. T. *J. Phys. Chem. C.* **2010**, *114*, 10229–10239.

(96) Zheng, X.; Blowers, P. *J. Phys. Chem. A.* **2005**, *109*, 10734–10741.

(97) Ding, B.-J.; Huang, S.-P.; Wang, W.-C. *Chinese J. Chem.* **2008**, *26*, 1173–1180.

(98) Zhao, Y.; Truhlar, D. G. *J. Phys. Chem. C.* **2008**, *112*, 6860–6868.

(99) Zhao, Y.; Schultz, N. E.; Truhlar, D. G. *J. Chem. Theory Comput.* **2006**, *2*, 364–382.

(100) Tranca, D. C.; Hansen, N.; Swisher, J. A.; Smit, B.; Keil, F. J. *J. Phys. Chem. C.* **2012**, *116*, 23408–23417.

(101) Choomwattana, S.; Maihom, T.; Boekfa, B.; Pantu, P.; Limtrakul, J. *Can. J. Chem. Eng.* **2012**, *90*, 865–872.

(102) Maihom, T.; Pantu, P.; Tachakritikul, C.; Probst, M.; Limtrakul, J. *J. Phys. Chem. C.* **2010**, *114*, 7850–7856.

(103) Zhao, Y.; Truhlar, D. G. *Acc. Chem. Res.* **2008**, *41*, 157–167.

(104) Zimmerman, P. M.; Head-Gordon, M.; Bell, A. T. *J. Chem. Theory. Comput.* **2011**, *7*, 1695–1703.

(105) Lin, H.; Truhlar, D. *Theor. Chem. Acc.* **2007**, *117*, 185–199.

(106) Bakowies, D.; Thiel, W. *J. Phys. Chem.* **1996**, *100*, 10580–10594.

(107) Vries, A. H. de; Sherwood, P.; Collins, S. J.; Rigby, A. M.; Rigutto, M.; Kramer, G. J. *J. Phys. Chem. B.* **1999**, *103*, 6133–6141.

(108) Clark, L. A.; Sierka, M.; Sauer, J. *J. Am. Chem. Soc.* **2004**, *126*, 936–947.

(109) Lomratsiri, J.; Probst, M.; Limtrakul, J. *J. Mol. Graph. Model* **2006**, *25*, 219 –225.

(110) Shor, A. M.; Shor, E. A. I.; Laletina, S.; Nasluzov, V. A.; Vayssilov, G. N.; Rösch, N. *Chem. Phys.* **2009**, *363*, 33 –41.

(111) Haag, W. O.; Dessau, R. M. In *Proceedings of The Eighth International Congress on Catalysis*, ed. by Main, F. am, 1984; Vol. 2, pp 305–316.

(112) Narbeshuber, T.; Vinek, H.; Lercher, J. *J. Catal.* **1995**, *157*, 388 –395.

(113) Krannila, H.; Haag, W.; Gates, B. *J. Catal.* **1992**, *135*, 115 –124.

(114) Gounder, R.; Iglesia, E. *J. Am. Chem. Soc.* **2009**, *131*, 1958–1971.

(115) Al-majnouni, K. A.; Yun, J. H.; Lobo, R. F. *ChemCatChem.* **2011**, *3*, 1333–1341.

(116) Bokhoven, J. A. van; Williams, B. A.; Ji, W.; Koningsberger, D. C.; Kung, H. H.; Miller, J. T. *J. Catal.* **2004**, *224*, 50–59.

(117) Chai, J.-D.; Head-Gordon, M. *J. Chem. Phys.* **2008**, *128*, 084106.

(118) Chai, J.-D.; Head-Gordon, M. *Phys. Chem. Chem. Phys.* **2008**, *10*, 6615–6620.

(119) Gomes, J.; Zimmerman, P. M.; Head-Gordon, M.; Bell, A. T. *J. Phys. Chem. C.* **2012**, *116*, 15406–15414.

(120) Bučko, T.; Benco, L.; Hafner, J.; Ángyán, J. G. *J. Catal.* **2011**, *279*, 220–228.

(121) Foster, J. P.; Weinhold, F. *J. Am. Chem. Soc.* **1980**, *102*, 7211–7218.

(122) Weinhold, F. In, Kutateladze, A. G., Ed.; Taylor and Francis: 2005; Chapter Computational Methods in Photochemistry, pp 393–477.

(123) Furtado, E.; Milas, I.; Albuquerque Lins, J. Milam de; Chaer Nascimento, M. *Phys. Status Solidi A* **2001**, *187*, 275–288.

(124) Pereira, M. S.; Chaer Nascimento, M. A. *J. Phys. Chem. B.* **2006**, *110*, 3231–3238.

(125) Bučko, T.; Benco, L.; Dubay, O.; Dellago, C.; Hafner, J. *J. Chem. Phys.* **2009**, *131*, 214508.

(126) Zhao, Y.; González-García, N.; Truhlar, D. G. *J. Phys. Chem. A.* **2005**, *109*, 2012–2018.

(127) De Moor, B. A.; Reyniers, M.-F.; Gobin, O. C.; Lercher, J. A.; Marin, G. B. *J. Phys. Chem. C.* **2011**, *115*, 1204–1219.

(128) Göltl, F.; Grüneis, A.; Bučko, T.; Hafner, J. *The Journal of Chemical Physics* **2012**, *137*, 114111.

(129) Boronat, M.; Corma, A. *Catal. Lett.* **2015**, *145*, 162–172.

(130) Gounder, R.; Iglesia, E. *Chem. Commun.* **2013**, *49*, 3491–3509.

(131) Babitz, S.; Williams, B.; Miller, J.; Snurr, R.; Haag, W.; Kung, H. *Appl. Catal. A-Gen.* **1999**, *179*, 71 –86.

(132) Bučko, T.; Hafner, J. *J. Catal.* **2015**, *329*, 32–48.

(133) Janda, A.; Bell, A. T. *J. Am. Chem. Soc.* **2013**, *135*, 19193–19207.

(134) Mallikarjun Sharada, S.; Zimmerman, P. M.; Bell, A. T.; Head-Gordon, M. *J. Phys. Chem. C.* **2013**, *117*, 12600–12611.

(135) Janda, A.; Vlaisavljevich, B.; Lin, L.-C.; Mallikarjun Sharada, S.; Smit, B.; Head-Gordon, M.; Bell, A. T. *J. Phys. Chem. C.* **2015**, *119*, 10427–10438.

(136) Li, Y.-P.; Gomes, J.; Mallikarjun Sharada, S.; Bell, A. T.; Head-Gordon, M. *J. Phys. Chem. C.* **2015**, *119*, 1840–1850.

(137) First, E. L.; Gounaris, C. E.; Wei, J.; Floudas, C. A. *Phys. Chem. Chem. Phys.* **2011**, *13*, 17339–17358.

(138) Sklenak, S.; Dedecek, J.; Li, C.; Gao, F.; Jansang, B.; Boekfa, B.; Wichterlová, B.; Sauer, J. *Czech. Chem. Commun.* **2008**, *73*, 909–920.

(139) Baerlocher, C.; Xie, D.; McCusker, L. B.; Hwang, S.-J.; Chan, I. Y.; Ong, K.; Burton, A. W.; Zones, S. I. *Nat Mater* **Aug. 2008**, *7*, 631–635.

(140) Bushuev, Y. G.; Sastre, G. *J. Phys. Chem. C.* **2009**, *113*, 10877–10886.

(141) Kokotailo, G. T.; Chu, P.; Lawton, S. L.; Meier, W. M. *Nature* **1978**, *275*, 119–120.

(142) Wagner, P.; Nakagawa, Y.; Lee, G. S.; Davis, M. E.; Elomari, S.; Medrud, R. C.; Zones, S. I. *J. Am. Chem. Soc.* **2000**, *122*, 263–273.

(143) Leonowicz, M. E.; Lawton, J. A.; Lawton, S. L.; Rubin, M. K. *Science* **1994**, *264*, 1910–1913.

(144) Zhou, D.; Bao, Y.; Yang, M.; He, N.; Yang, G. *J. Mol. Catal. A-Chem.* **2006**, *244*, 11 –19.

(145) Li, Y.; Guo, W.; Fan, W.; Yuan, S.; Li, J.; Wang, J.; Jiao, H.; Tatsumi, T. *J. Mol. Catal. A-Chem.* **2011**, *338*, 24 –32.

(146) Janda, A.; Vlaisavljevich, B.; Lin, L.-C.; Smit, B.; Bell, A. T. *In preparation* **2015**.

(147) Gounder, R.; Iglesia, E. *Acc. Chem. Res.* **2012**, *45*, 229–238.

(148) Hunter, K. C.; East, A. L. L. *J. Phys. Chem. A.* **2002**, *106*, 1346–1356.

(149) Xu, B.; Sievers, C.; Hong, S. B.; Prins, R.; Bokhoven, J. A. van *J. Catal.* **2006**, *244*, 163 –168.

(150) Liu, D.; Bhan, A.; Tsapatsis, M.; Al Hashimi, S. *ACS Catal.* **2011**, *1*, 7–17.

(151) Piccini, G.; Sauer, J. *J. Chem. Theory Comput.* **2013**, *9*, 5038–5045.

(152) Thouless, D. *Nucl. Phys.* **1960**, *21*, 225 –232.

(153) Adams, W. H. *Phys. Rev.* **1962**, *127*, 1650–1658.

(154) Čížek, J.; Paldus, J. *J. Chem. Phys.* **1967**, *47*, 3976–3985.

(155) Paldus, J.; Čížek, J. *Phys. Rev. A* **1970**, *2*, 2268–2283.

(156) Lochan, R. C.; Head-Gordon, M. *J. Chem. Phys.* **2007**, *126*, 164101.

(157) Sherrill, C. D.; Krylov, A. I.; Byrd, E. F. C.; Head-Gordon, M. *J. Chem. Phys.* **1998**, *109*, 4171–4181.

(158) Bozkaya, U.; Turney, J. M.; Yamaguchi, Y.; Schaefer, H. F.; Sherrill, C. D. *J. Chem. Phys.* **2011**, *135*, 104103.

(159) Stück, D.; Baker, T. A.; Zimmerman, P.; Kurlancheek, W.; Head-Gordon, M. *J. Chem. Phys.* **2011**, *135*, 194306.

(160) Scuseria, G. E.; III, H. F. S. *Chem. Phys. Lett.* **1987**, *142*, 354 –358.

(161) Krylov, A. I.; Sherrill, C. D.; Byrd, E. F. C.; Head-Gordon, M. *J. Chem. Phys.* **1998**, *109*, 10669–10678.

(162) Neese, F.; Schwabe, T.; Kossmann, S.; Schirmer, B.; Grimme, S. *J. Chem. Theory Comput.* **2009**, *5*, 3060–3073.

(163) Kurlancheek, W.; Head-Gordon, M. *Mol. Phys.* **2009**, *107*, 1223–1232.

(164) Stück, D.; Head-Gordon, M. *J. Chem. Phys.* **2013**, *139*, 244109.

(165) Handy, N. C.; Pople, J. A.; Head-Gordon, M.; Raghavachari, K.; Trucks, G. W. *Chem. Phys. Lett.* **1989**, *164*, 185 –192.

(166) Purvis, G. D.; Bartlett, R. J. *J. Chem. Phys.* **1982**, *76*, 1910–1918.

(167) Bauernschmitt, R.; Ahlrichs, R. *J. Chem. Phys.* **1996**, *104*, 9047–9052.

(168) Mardirossian, N.; Head-Gordon, M. *Phys. Chem. Chem. Phys.* **2014**, *16*, 9904–9924.

(169) Vydrov, O. A.; Van Voorhis, T. *J. Chem. Phys.* **2010**, *133*, 244103.

(170) Sharada, S. M.; Bell, A. T.; Head-Gordon, M. *J. Chem. Phys.* **2014**, *140*, 164115.

(171) Crouzeix, M.; Philippe, B.; Sadkane, M. *SIAM J. Sci. Comput.* **1994**, *15*, 62–76.

(172) Sherrill, C. D.; III., H. F. S. In, Per-Olov Löwdin John R. Sabin, M. C. Z., Brändas, E., Eds.; Advances in Quantum Chemistry, Vol. 34; Academic Press: 1999, pp 143 –269.

(173) Voorhis, T. van; Head-Gordon, M. *Mol. Phys.* **2002**, *100*, 1713–1721.

(174) Sleijpen, G.; Vorst, H. van der; Ruhe, A.; Bai, Z.; Ericsson, T.; Kowalski, T.; Kågström, B.; Li, R. In *Templates for the Solution of Algebraic Eigenvalue Problems*; Chapter 8, pp 233–279.

(175) Shao, Y. et al. *Mol. Phys.* **2015**, *113*, 184–215.

(176) Beran, G. J.; Head-Gordon, M. *J. Phys. Chem. A.* **2006**, *110*, 9915–9920.

(177) Lawler, K. V.; Small, D. W.; Head-Gordon, M. *J. Phys. Chem. A.* **2010**, *114*, 2930–2938.

(178) Dunning, T. H. *J. Chem. Phys.* **1989**, *90*, 1007–1023.

(179) Karton, A.; Daon, S.; Martin, J. M. *Chem. Phys. Lett.* **2011**, *510*, 165 –178.

Appendix A

Insights into the Kinetics of Cracking and Dehydrogenation Reactions of Light Alkanes in H-MFI

A.1 Contribution of non-bonding interactions

The relative contributions of dispersion and electrostatic interactions to the lowering of intrinsic activation energy were calculated using the QM/MM model, by removing one or both of these components from the model system. The results for the T12 site are shown in Figure A.1. The difference between activation energies with and without these interactions ranges from 10 to 18 kcal/mol, demonstrating conclusively that the presence of substrate-framework interactions is essential for modeling zeolite-based kinetics. Moreover, the activation energy lowering is almost entirely due to electrostatic interactions, with negligible contribution from dispersion.

A.2 Validation of the cluster model

In order to demonstrate that calculated intrinsic activation energies show low sensitivity to the size of the QM region, a larger T33 QM region is considered. Without re-optimizing the previously calculated transition states, single point electronic energies were calculated for cracking reactions at the T12 site with the T33 QM model. The resulting activation energies are compared with the T5 QM model in Table A.1. The difference between T33 and T5 ranges from 2.5 kcal/mol to 3 kcal/mol, which is higher than the computational error margin of 2 kcal/mol. However, the differences in activation energies between various cracking pathways are preserved with respect to the QM cluster size. The QM/MM cluster model containing a small T5 region and a large T432 MM region, therefore, is a reasonable representation of an acid site in the H-MFI framework.

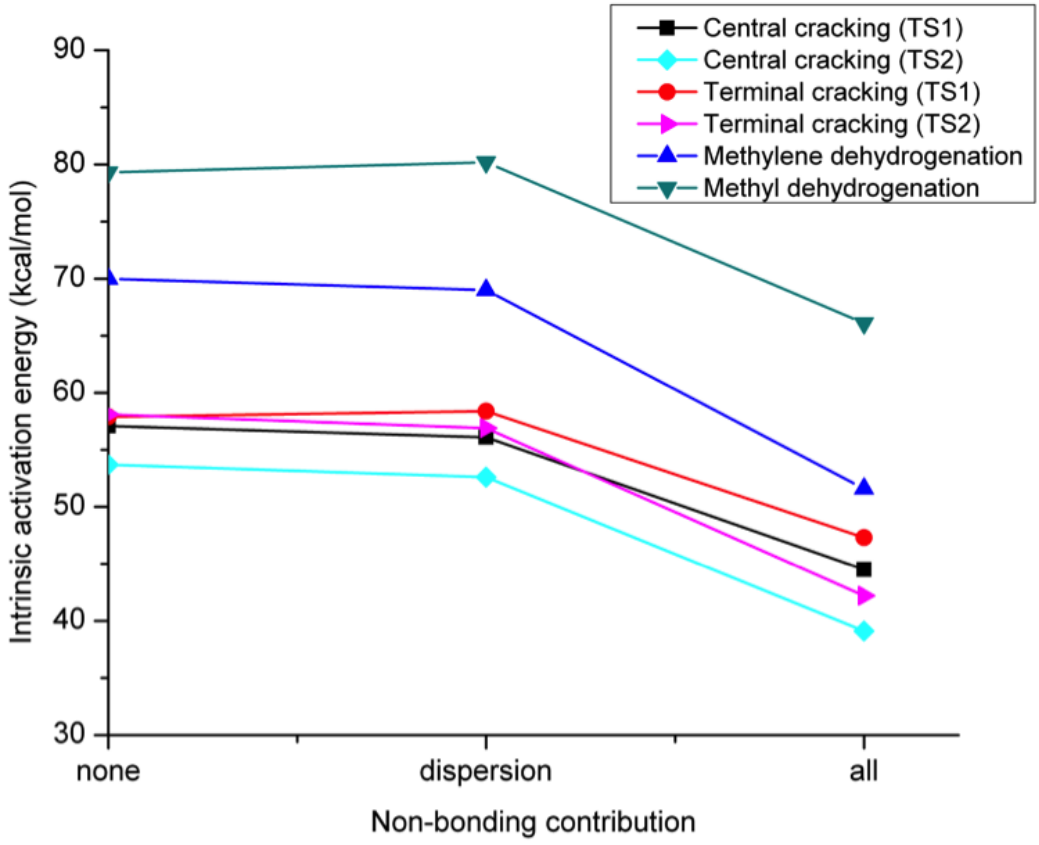

Figure A.1: Intrinsic activation energies (kcal/mol) for reactions of n-butane at the T12 site. "None" corresponds to the absence of dispersion and electrostatics. Dispersion is added in the next stage with little reduction in activation energy. "All" corresponds to QM/MM energy obtained on including all long-range interactions.

Cracking pathway	**T33**	**T5**	**Difference**
Central (TS1)	47.3	44.5	2.8
Central (TS2)	41.7	39.1	2.6
Terminal (TS1)	49.8	47.3	2.5
Terminal (TS2)	45.3	42.2	3.1

Table A.1: Intrinsic activation energies (kcal/mol) for n-butane cracking at the T12 site (excluding zero point corrections) calculated with QM region consisting of 33 and 5 T-atoms, respectively.

Charge on Brønsted acid proton	**T12**	**T10**
Adsorbed n-butane	0.56	0.56
Methyl dehydrogenation TS	0.40	0.40
Methylene dehydrogenation TS	0.36	0.35

Table A.2: Natural charges on the Brønsted acid proton when n-butane is adsorbed near the acid site, compared to charges on the leaving H atoms in the transition states for dehydrogenation.

A.3 Natural bond orbital (NBO) analysis for the dehydrogenation transition state

In order to verify that dehydrogenation proceeds via simultaneous H_2 formation and proton migration to the acid site, natural bond orbital analysis is carried out to determine the charge on the leaving H relative to that of a Brønsted acid proton. The results of the analysis are shown in Table A.2. The leaving H attains about 60% and 70% Brønsted acid character for methylene and methyl dehydrogenation, respectively, confirming that the mechanism for dehydrogenation is concerted. For the reactant and transition states, the natural charges on primary and secondary H atoms other than the leaving H range from 0.19 to 0.25, which are distinctly lower than the charge on an acid proton.

A.4 Heats of adsorption

Although dual-basis correction shifts the heat of adsorption value closer to the complete basis set limit, the corrected value represents more overbinding relative to the uncorrected value, which can be as high as 1 kcal/mol. The uncorrected values, therefore, were plotted in Figure 4.15. These values, along with the dual-basis corrections are reported in Table A.3.

Alkane	**T12 site**			**T10 site**		
	Uncor-rected	Dual basis corrected	Difference	Uncor-rected	Dual basis corrected	Difference
propane	-10.5	-11.1	-0.6	-14.7	-15.0	-0.3
n-butane	-15.5	-16.3	-0.8	-17.3	-17.8	-0.5
n-pentane	-20.5	-21.4	-0.9	-23.8	-24.5	-0.7
n-hexane	-24.5	-25.4	-1.0	-24.5	-25.6	-1.0

Table A.3: Heats of adsorption (kcal/mol) for alkanes in silicalite at 773 K, calculated both with 6-311G** (uncorrected), as well as by applying dual basis correction with 6-311++G(3df,3pd).